Dynamics of Structures

a workshop on dynamic loads and response of structures and soil dynamics

Hansen, Lars Pilegaard

Publication date:
1994

Document Version
Accepted author manuscript, peer reviewed version

DYNAMICS OF STRUCTURES

A workshop on dynamic loads and
response of structures and soil dynamics

AALBORG UNIVERSITY
DENMARK
September 14-15, 1994

DYNAMICS OF STRUCTURES

A workshop on dynamic loads and
response of structures and soil dynamics

AALBORG UNIVERSITY
DENMARK
September 14-15, 1994

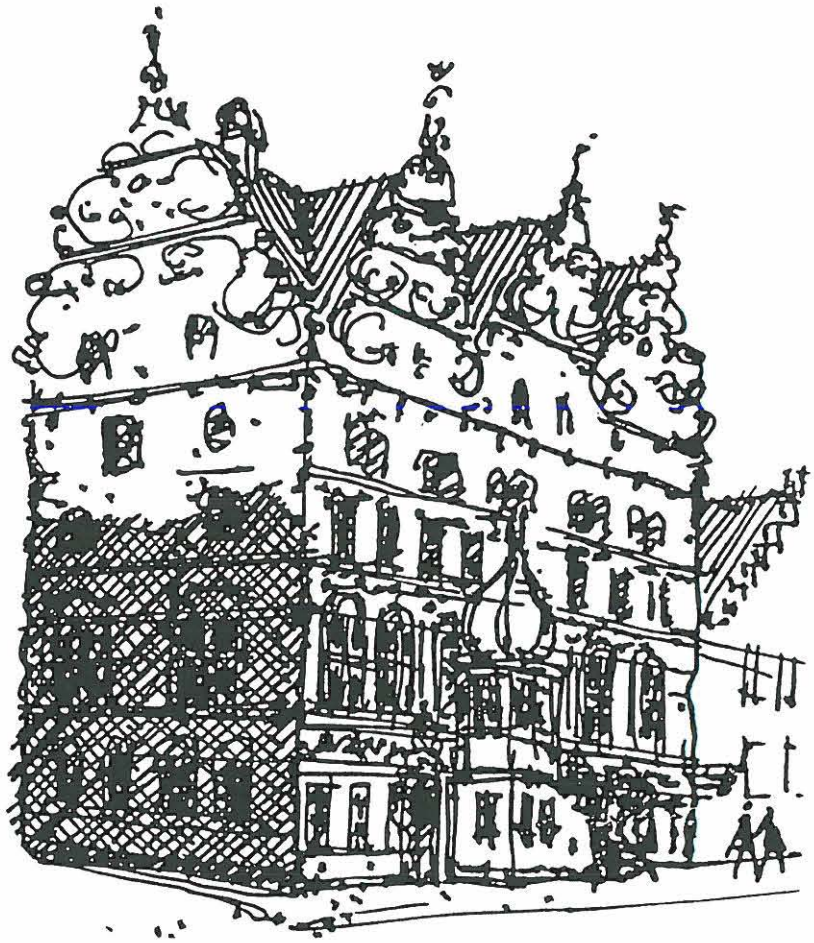

Dynamics of Structures,

Workshop Programme

Wednesday, September 14, Lecture Room A217

15.00-17.00	Presentation of laboratories and tests: *Structural Lab.:* Damage detection and fatigue. *Geotechnical Lab.:* Dynamic triaxial tests. *Hydraulics Lab.:* Dynamic wave loads.
19.30-?	**Dinner at restaurant Kniv & Gaffel, Maren Turisgade 10, 9000 Aalborg.**

Thursday, September 15, Lecture Room A217

09.00-09.05	**Welcome by Steen Krenk, Aalborg University**
09.00-09.30	*Lessons from Model Tests with Cyclic Loading of a Gravity Structure on Very Dense Sand,* Knut Andersen, Norwegian Geotechnical Institute
09.30-09.45	*Simplified Response Analysis of Guyed Masts according to EC3 Part 3.1,* Mogens G. Nielsen, Rambøll, Hannemann & Højlund A/S
09.45-10.00	*A Non-Linear Mathematical Model For Vortes Shedding Forces On Flexible Structures*, Allan Larsen, COWIconsult A/S
10.00-10.15	*Identification and Damage Detection on Structural Systems*, Rune Brincker, Aalborg University
10.15-10.30	*Damage Assessment of a Steel Lattice Mast under Natural Excitation*, Poul Henning Kirkegaard, Aalborg University
10.30-11.00	**Coffee**
11.00.11.30	*Dynamic Problems Related to Coastal Structures,* Hans Falk Burcharth, Aalborg University
11.30-11.45	*Development of Pore Pressure and Material Damping during Cyclic Loading,* Lars Bo Ibsen, Aalborg University
11.45-12.00	*Linear and Quadratic Lanczos Algorithms*, Steffen Vissing, Aalborg University
12.00-12.15	*Prediction of Global and Localized Damage and Future Reliability for RC Structures Subject to Earthquakes,* Søren R.K. Nielsen, Aalborg University
12.15-12.30	*Perturbation Solutions for Random Linear Structural Systems Subject to Random Excitation using Stochastic Differential Equations,* Søren R.K. Nielsen, Aalborg University
12.30-13.30	**Lunch**
13.30-14.00	*Measured and Predicted Response of an Offshore Gravity Platform,* Ivar Langen, Høgskolesenteret i Rogaland, Norway
14.00-14.30	*Dynamic Aspects of Bridge Piers with Plane Base Plate*, Helge Gravesen/Ole A. Madsen, Carl Bro Civil and Transportation A/S
14.30-14.45	*Man-Induced Vibrations*, Jeppe Jönsson, Aalborg University
14.45-15.00	*Fatigue and Crack Propagation*, Thomas Cornelius Hansen, Danish Technical University
15.00	**Closure**

Workshop, den 14.-15. september 1994
Aalborg Universitet

Deltagerliste

Andersen, Knut H.
Norges Geotekniske Institutt
Postboks 3930 Ullevål Hageby
0806 Oslo
Tlf. + 47 22 23 03 88
Fax. + 47 22 23 04 48

Andersen, Palle
Aalborg Universitet
Inst. for Bygningsteknik
Sohngaardsholmsvej 57
9000 Aalborg
Tlf. 98 15 85 22
Fax. 98 14 82 43

Asmussen, John
Aalborg Universitet
Inst. for Bygningsteknik
Sohngaardsholmsvej 57
9000 Aalborg
Tlf. 98 15 85 22
Fax. 98 14 82 43

Brincker, Rune
Aalborg Universitet
Inst. for Bygningsteknik
Sohngaardsholmsvej 57
9000 Aalborg
Tlf. 98 15 85 22
Fax. 98 14 82 43

Burcharth, Hans Falk
Aalborg Universitet
Inst. for Vand, Jord og Miljøteknik
Sohngaardsholmsvej 57
9000 Aalborg
Tlf. 98 15 85 22
Fax. 98 14 25 55

Bødker, Lars
Aalborg Universitet
Inst. for Vand, Jord og Miljøteknik
Sohngaardsholmsvej 57
9000 Aalborg
Tlf. 98 15 85 22
Fax. 98 14 25 55

Damkilde, Lars
Afd. for Bærende Konstruktioner
DTU, Bygning 118
2800 Lyngby
Tlf. 45 93 12 22
Fax. 42 88 32 82

Gravesen, Helge
Carl Bro Anlæg as
Rådgivende ingeniørfirma F.R.I.
Granskoven 8
2600 Glostrup
Tlf. 42 45 99 99
Fax. 43 63 65 67

Hansen, Henriette
Aalborg Universitet
Institut for Bygningsteknik
Sohngaardsholmsvej 57
9000 Aalborg
Tlf. 98 15 85 22
Fax. 98 14 82 43

Hansen, Svend Ole
Svend Ole Hansen ApS
Sct. Jørgens Allé 7
1615 København V
Tlf. 33 25 38 38
Fax. 33 25 38 39

Hansen, Lars Pilegaard
Aalborg Universitet
Inst. for Bygningsteknik
Sohngaardsholmsvej 57
9000 Aalborg
Tlf. 98 15 85 22
Fax. 98 14 82 43

Hansen, Thomas Cornelius
Afd. for Bærende Konstruktioner
Danmarks Tekniske Universitet
Bygning 118
2800 Lyngby
Tlf. 45 93 12 22
Fax. 42 88 32 82

Ibsen, Lars Bo
Aalborg Universitet
Inst. for Vand, Jord og Miljøteknik
Sohngaardsholmsvej 57
9000 Aalborg
Tlf. 98 15 85 22
Fax. 98 14 25 55

Jensen, Søren
University of Maryland
Department of Mathematics
Baltimore
MD 21044, USA
Tlf. + 1 410 455 3294
Fax. + 1 410 455 1066

Jönsson, Jeppe
Aalborg Universitet
Inst. for Bygningsteknik
Sohngaardsholmsvej 57
9000 Aalborg
Tlf. 98 15 85 22
Fax. 98 14 82 43

Kirkegaard, Poul Henning
Aalborg Universitet
Inst. for Bygningsteknik
Sohngaardsholmsvej 57
9000 Aalborg
Tlf. 98 15 85 22
Fax. 98 14 82 43

Krenk, Steen
Aalborg Universitet
Inst. for Bygningsteknik
Sohngaardsholmsvej 57
9000 Aalborg
Tlf. 98 15 85 22
Fax. 98 14 82 43

Langen, Ivar
Høgskolesenteret i Rogaland
P.O. Box 2557, Ullandhaug
N-4004 Stavanger, Norway
Tlf + 47 51 83 13 50
Fax. + 47 51 83 10 00

Larsen, Allan
COWI Consult
Parallelvej 15
2800 Lyngby
Tlf. 45 97 28 72
Fax. 45 97 21 12

Madsen, Ole Alenkær
Carl Bro Civil & Transportation
Granskoven 12
2600 Glostrup
Tlf. 42 45 99 99
Fax. 43 63 65 67

Nielsen, Mogens G.
Rambøll, Hannemann & Højlund a/s
Bredevej 2
2830 Virum
Tlf. 42 85 65 00
Fax. 45 83 02 07

Nielsen, Henrik Lundorf
KAMPSAX GEODAN
Karlskogavej 12
Postboks 13
9100 Aalborg
Tlf. 98 18 35 00
Fax. 98 18 38 39

Nielsen, Søren R. K.
Aalborg Universitet
Inst. for Bygningsteknik
Sohngaardsholmsvej 57
9000 Aalborg
Tlf. 98 15 85 22
Fax. 98 14 82 43

Sandberg, Göran
Division of Structural Mechanics
Lunds Tekniske Højskole, Box 118
S-221 00 Lund, Sweden
Tlf. + 46 46 10 81 46
Fax + 46 46 10 44 20

Vissing, Steffen
Aalborg Universitet
Inst. for Bygningsteknik
Sohngaardsholmsvej 57
9000 Aalborg
Tlf. 98 15 85 22
Fax. 98 14 82 43

Sekretær
Sørensen, Pernille
Aalborg Universitet
Inst. for Bygningsteknik
Sohngaardsholmsvej 57
9000 Aalborg
Tlf. 98 15 85 22
Fax. 98 14 82 43

LESSONS FROM MODEL TESTS WITH CYCLIC LOADING OF A GRAVITY STRUCTURE ON VERY DENSE SAND

by

Knut H. Andersen, Norwegian Geotechnical Institute

Model testing has in the past been successfully used to verify the foundation design procedures for cyclically loaded structures on clay. Model testing of cyclically loaded structures on sand has been limited, however, and the foundation design procedures for cyclically loaded structures on sand have not been verified to the same extent as for structures on clay.

The main reasons why model testing of cyclically loaded structures on sand has been limited, are the needs to simulate the gravity stresses and the drainage conditions in the prototype correctly in the model. The gravity stresses can be modelled in centrifuge tests, but the drainage will occur much more rapidly in a centrifuge model than in a prototype. Pore pressure generation due to cyclic loading and negative pore pressures due to dilatancy are then not reproduced correctly.

Recently Delft Geotechnics developed a viscous fluid that can be used as pore fluid in various types of soil instead of water. This pore fluid enables scaling according to the similitude equations that must be fulfilled to perform realistic centrifuge model experiments of cyclically loaded structures on sand. Special triaxial and oedometer tests were run to show that the viscous pore fluid does not influence the engineering properties of the sand.

In a cooperative project between Delft Geotechnics and the Norwegian Geotechnical Institute, two pilot model tests were performed on an offshore gravity platform on very dense sand to demonstrate the feasibility of the centrifuge modelling technique with the new pore fluid. In one test the platform was loaded monotonically, and in the other test it was loaded with a cyclic load history representative for a North Sea design storm. The tests were instrumented with piezometers and total stress devices at the base. Displacement transducers defined all displacement components, and a load cell attached to the hydraulic actuator recorded the applied loading history.

Even if these first tests were meant as pilot tests to demonstrate the feasibility of the centrifuge modelling technique, they provided valuable

data that have been used to check the geotechnical calculation procedures. The interpretation concludes that the bearing capacity and the displacements of offshore gravity platforms on very dense sand can be reasonably well predicted. Static and cyclic triaxial and direct simple shear laboratory tests are needed to provide the soil parameters in the calculations. The measured bearing capacity was higher than what is normally assumed in design. The main reason is that the high negative pore pressures induced by dilatancy in very dense sand normally has not been fully relied on in practical design. The results indicate that it may be the displacements rather than the bearing capacity that will govern the allowable cyclic loads on a cyclically loaded structure on very dense sand.

The results of the model tests are described in:

Allard A., K.H. Andersen and J. Hermstad (1994)
"Centrifuge Model Tests of a Gravity Platform on Very Dense Sand; Testing Techniques and Results". Conference on Behaviour of Offshore Structures, BOSS'94, Boston 1994, Proceedings Vol 1, pp 231-254.

Andersen K.H., A. Allard and J. Hermstad (1994)
"Centrifuge Model Tests of a Gravity Platform on Very Dense Sand; Interpretation". Conference on Behaviour of Offshore Structures, BOSS'94, Boston 1994, Proceedings Vol 1, pp 255-282.

CENTRIFUGE MODEL

- *EKOFISK TANK* -

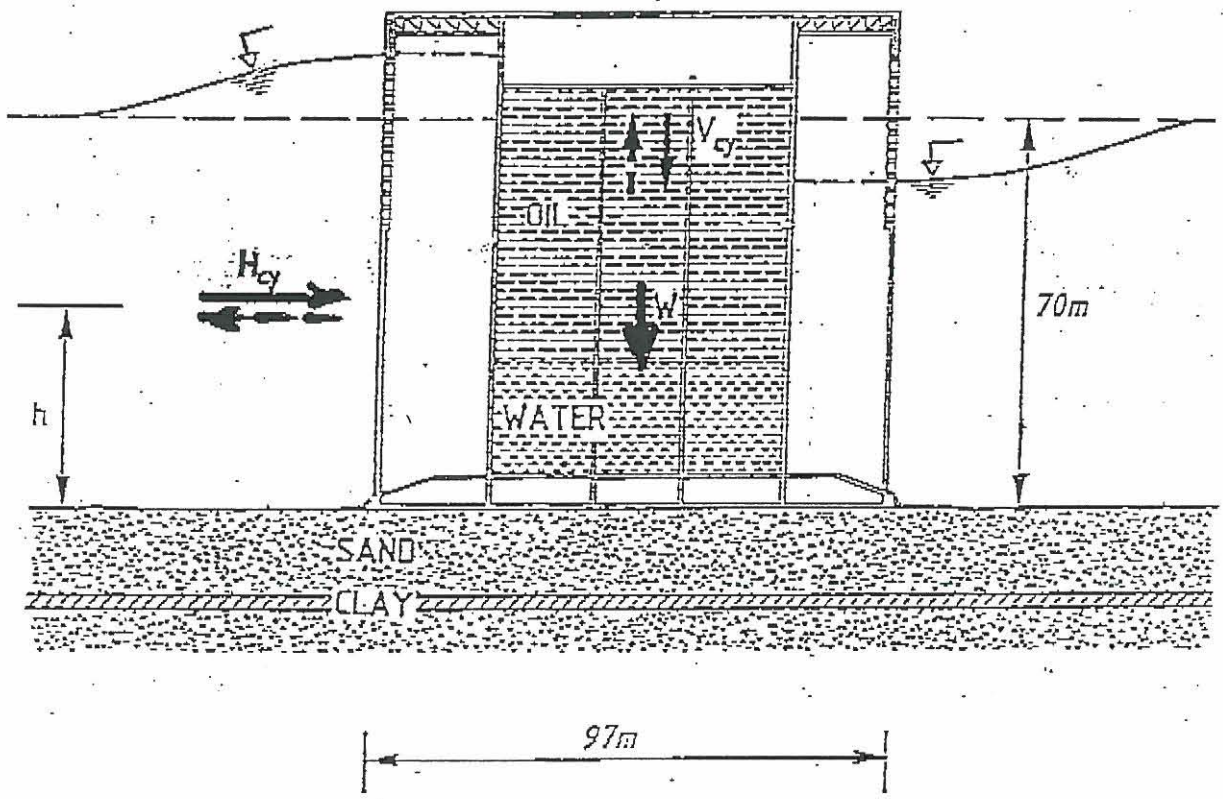

Very dense sand

2 tests; 1 monotonic and 1 cyclic

Centrifuge acceleration: 300g

Scaling: - length: 1/300
- time: $1/300^2$
- viscous fluid

DYNAMICS OF STRUCTURES

Aalborg University, Denmark, September 14-15, 1994.

SIMPLIFIED RESPONSE ANALYSIS OF GUYED MASTS ACCORDING TO EC3 PART 3.1

Mogens G. Nielsen
Rambøll, Hannemann & Højlund A/S
Bredevej 2, DK-2830 Virum, Denmark.

1. INTRODUCTION

The response of a guyed mast is rather difficult to analyze due to the non-linearities of the structure and the dynamics of the wind.

Guyed masts differs from towers by having non-linear deflections and several low eigenfrequencies, which makes the stochastic analysis very extensive.

Over the history a lot of different methods has been used for analysing guyed masts in order to make a simplified model of the dynamic response. Some of the methods is described below.

At the present time work is being done to make an European code for towers and masts: EUROCODE 3: Part 3.1 [2] and Rambøll, Hannemann & Højlund participates in this work.

2. ANALYSIS ACCORDING TO THE IASS-RECOMMENDATION

The method proposed in the IASS-recommendation for guyed masts [1] is based on patch wind loading in order to model the dynamics of the wind.

The principle of the method is to find the worst combination of the response from varying the wind pressure in some patches over the height of the guyed mast between the mean wind pressure and the maximum wind pressure. The maximum wind pressure is equal to the gust wind pressure except for the cantilever part where it is the gust wind pressure increased by 30%.

The patches are based on the spans between adjacent guy levels and over the cantilever if any. The procedure requires several static wind analyses for each wind direction considered in order to get the maximum response.

3. ANALYSIS ACCORDING TO THE RH&H PROCEDURE

Rambøll, Hannemann & Højlund has designed guyed masts for almost 50 years and has introduced a new patch wind method which in principle is as the procedure in

the IASS Recommendation. Though the method is changed in order to improve the model of the effect of the non-linearities.

The wind pressures in the combination of the patches are:

$$q_{full} = q_{mean} + k\,(q_{gust} - q_{mean})$$

$$q_{red} = q_{mean} - k\,(q_{gust} - q_{mean})$$

where q_{gust} is the gust wind pressure and q_{mean} is the mean wind pressure. k is a factor which takes the dynamics of the wind and the structure into account, and k is 1.0 for normal span and 2.0 for a cantilever.

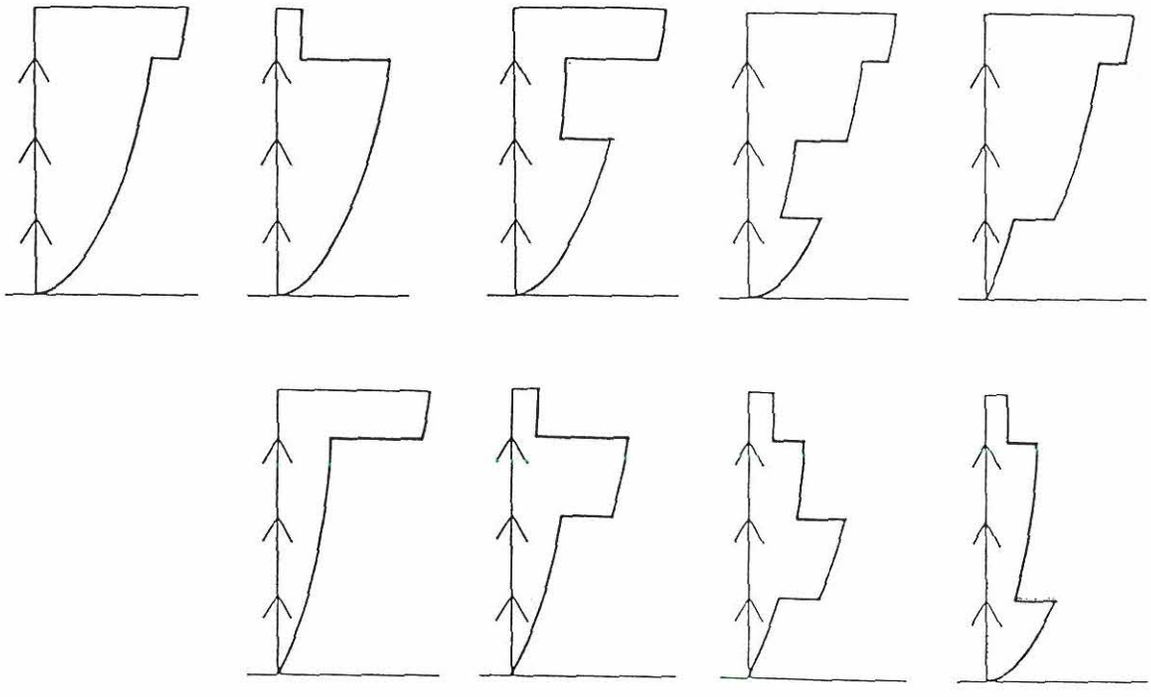

Fig 3.1 Application of patch loads according to RH&H procedure.

4. ANALYSIS ACCORDING TO EC3 PART 3.1

The method in the draft of EC3, Part 3.1 [2] is based upon a method proposed by Davenport and Sparling [3]. A similar method is also used in BS 8100 [5].

The principle of the method is to model the response from the wind as in the stochastic method with a mean and a fluctuating part.

Using this method the peak dynamic response is expressed as:

$$F_{peak} = F_{mean} \pm F_{fluctuating}$$

Where the F_{mean} is determined as the response, when structure is exposed to the mean wind load.

The fluctuating response, $F_{fluctuating}$ is determined as the root sum of the squares of the effects of the patch loads:

$$F_{fluctuating} = \sqrt{\sum_{i=1}^{N} F_{PLi}^{2}}$$

where F_{PLi} is the effect of the i'th patch load.

The fluctuating part of the wind pressure is determined by:

$$q_{fluctuating} = g\ \rho\ I_v\ V_m^2$$

where ρ is the density of the wind, I_v is the turbulence of the wind, V_m is the mean wind speed and g is the gust factor. G is set to 3.5.

The patches in this method differs from the patches in the IASS method (See fig. 4.1).

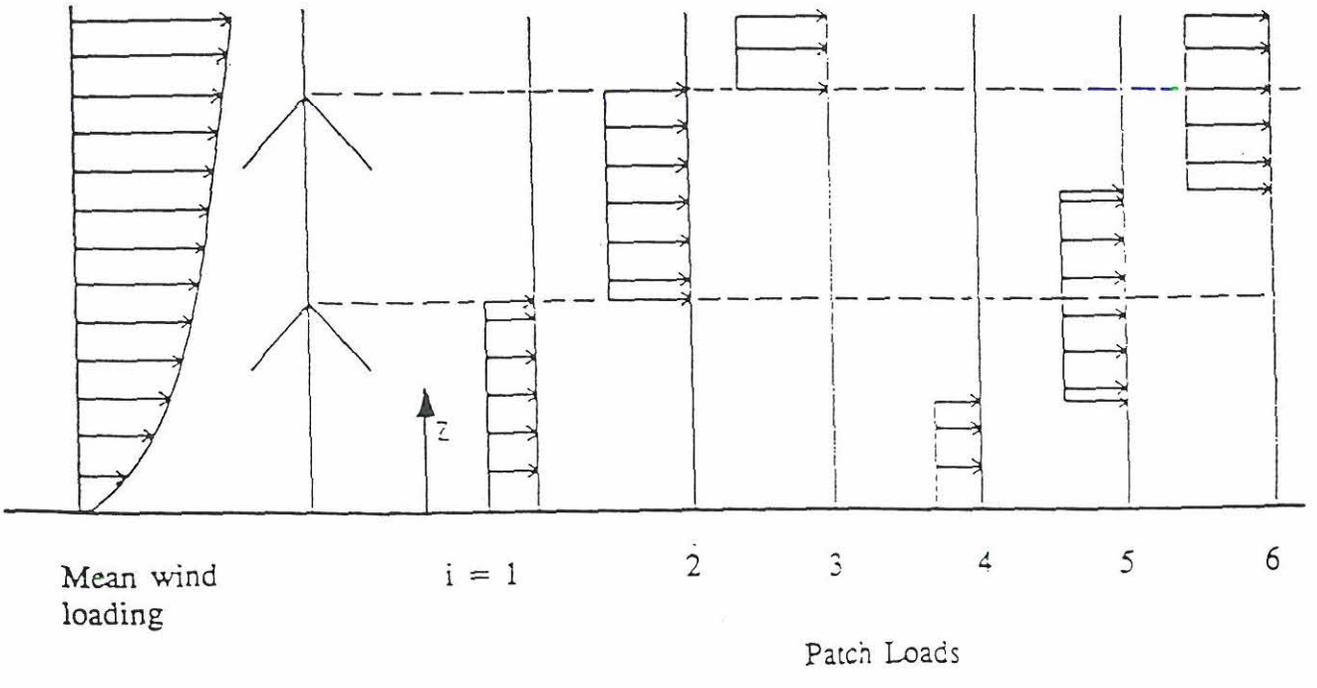

Fig 4.1 Application of patch loads according to EC3, Part 3.1.

5. STOCHASTIC ANALYSIS

Rambøll, Hannemann & Højlund has developed a program MAINMAST to make stochastic analyses of guyed masts [6].

The wind load is separated into the mean wind load, the turbulent load and the aerodynamic load, and it is assumed that the turbulent part of the wind velocity and the velocity of the mast are small compared to the mean wind velocity.

The expected extreme response is found by the traditional equation:

$$F_{extr} = F_{mean} \pm g\ \sigma_F$$

Where the F_{mean} is determined as the response, when structure is exposed to the mean wind load.

G is the peak factor and σ_F is the standard deviation of F. σ_F is determined from the equilibrium with the mast exposed to the mean wind and is found by an integration over frequency and a double integration over height of the structure. The wind load is based on the cross spectrum of the turbulent wind.

Using this method it is assumed that the deflections are linear from the equilibrium with the mean wind load.

6. COMPARISON BETWEEN THE DIFFERENT ANALYSIS

During the work of the EC3 part 3.1 several comparisons between the above mentioned methods have been undertaken and it seams as though the traditional IASS patch wind and the EC3 part 3.1 method is on the safe side compared to the stochastic method.

One of the mast that has been analyzed is the Danish 300 m mast and here the IASS patch wind method is very much on the save side if the gust wind speed is based on the EC1 values.

The mast was designed for the wind speeds defined in DS 410, and where the gust wind speed is relatively small compared to the mean wind speed. Comparing the results from the analyses based on these with the results from the stochastic analysis gives a relatively good agreement.

Fig. 6.1 shows a comparison for the Danish 300 m mast between the overall extreme member forces between the stochastic analysis ("Full Dynamic"), the BS 8100 patch wind analysis, the IASS patch wind analysis and the EC3 part 3.1 patch analysis. The mast has been analyzed for three directions of the wind. From fig. 6.1 it can be seen that the that the EC3 part 3.1 is very close to the stochastic analysis and mostly on the safe side. For the diagonals near the guy levels the forces are very much on the safe side.

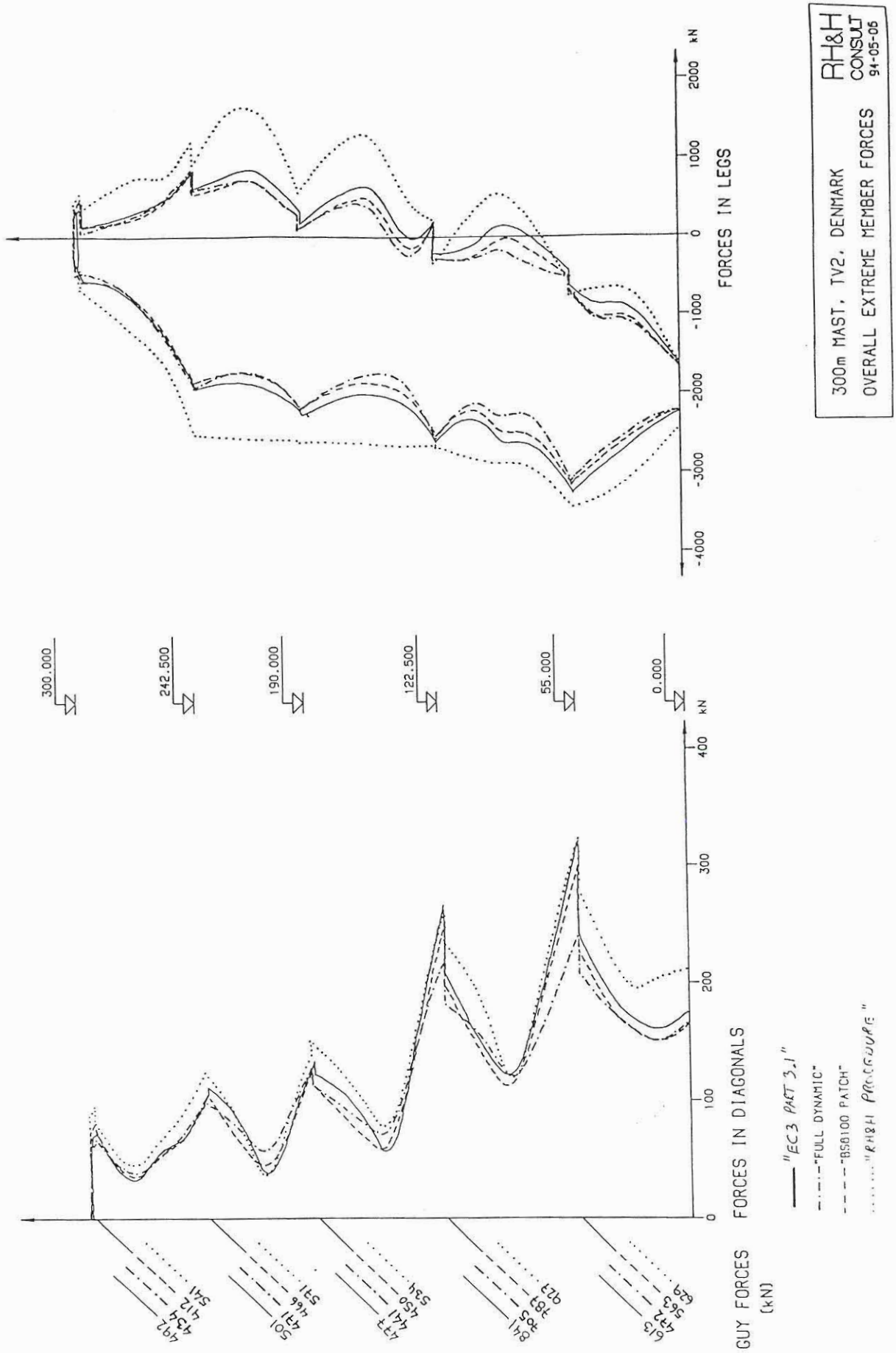

Fig. 6.1 Comparison between the overall extreme member forces from different analysis (The Danish 300 m mast).

7. REFERENCES

[1] Recommendations for guyed masts, IASS Working Group nr. 4, Madrid, 1981.

[2] EUROCODE 3: Part 3.1: Towers and Masts, Annex A: Response to Meteorological Actions, First Draft July 1994.

[3] A.G.Davenport and B.F.Sparling: Dynamic gust response factors for guyed towers, Presented at the 8th International Conference on Wind Engineering, University of Western Ontario, London, Canada, July 8-12, 1991.

[4] EUROCODE 1: Basis of Design and Actions on Structures, Part 2.3: Wind Actions, ENV 1991-2-3, 3. Dec. 1993, Preliminary Drafting Note.

[5] BS 8100: Lattice towers and masts, Part 4 code of practice for lattice masts, Draft, July 1992.

[6] MAINMAST, Technical Documentation: Model description for calculation of maximal dynamic response, Internal Documentation, Rambøll & Hannemann 1990.

A Non-Linear Mathematical Model For Vortex Shedding Forces On Flexible Structures

Allan Larsen
COWIconsult A/S, Parallelvej 15, 2800 Lyngby, Denmark

Abstract

The present paper (condensed form) proposes a one degree of freedom (1DOF) non-linear model of self limiting cyclic fluid loads for application in Finite Element Method analyses of light flexible structures subjected to vortex shedding excitation under lock-in conditions. Being empirical by nature, the model includes three independent parameters to be determined from response tests with representative fluid-elastic scale models or prototypes. The presentation will evaluate the proposed load / response model against other 1DOF empirical vortex shedding models which have found some acceptance in structural engineering and will discuss methods for parameter identification from measured response data.

1. INTRODUCTION

Flexible and lightly damped slender structures are often found to be prone to vortex-induced vibrations when submerged in a stream of fluid. Notable examples includes cable supported bridges, chimneys and towers exposed to wind and marine risers, pipelines, poles and taut cables exposed to ocean current. The bluff shape of most practical structural cross sections promotes formation of periodic and coherent von Karman type "vortex streets" in the wake of the structure. Large amplitude resonant vibrations may occur in speed ranges of the fluid flow where the vortex shedding action locks on to one of the cross flow vibration modes of the structure. At this condition, commonly referred to as lock-in, vortex-induced vibrations are found to be self-limiting, amplitude dependent and highly sensitive to the density of the fluid and the mass density and the inherent damping level of the structure.

The Finite Element Method has received broad acceptance as the foremost analysis tool in contemporary structural engineering. FEM analyses allow detailed computations of the overall response and stress distributions in critical structural members subjected to deterministic or random loads. Hence FEM computations appear as the logical choice for assessment of vortex shedding action on slender structures and for evaluation of alternative damping measures intended for suppression of excessive vortex induced responses.

The objective of the present paper is to establish a suitable forcing function model which recognizes the non-linear amplitude dependent character of the vortex shedding action. Also the model must be capable of reproducing the functional relationship between response and mass density / structural damping as estab-

lished through physical testing of a given structure submerged in a fluid flow. Finally, the proposed model must comply with the load generation facilities commonly available in commercial FEM codes.

2. 1DOF VORTEX SHEDDING MODELS IN THE LITERATURE

Structural loads are usually applied in dynamic FEM analyses as external time dependent forcing functions of a predefined magnitude and are thus independent of the structural response. Scruton [1] discussed use of this approach (the simple forced lift oscillator at resonance) for mathematical modelling of cross flow forces due to vortex shedding. He concluded that the resulting hyperbolic relationship between vortex induced response and structural damping was not consistent with wind tunnel observations of cylinders oscillating at finite amplitudes. The resonant forced lift oscillator model was later applied by Smith and Wyatt [2] as a convenient framework for correlation of wind tunnel test results obtained in connection with drafting of the proposed british design rules for bridge aerodynamics. The hyperbolic relationship between structural response and structural damping, $\eta \approx 1/\zeta$ is thus reflected in empirical formulae given in the above mentioned design rules.

Amplitude dependent loads may be introduced in FEM models as negative damping elements (dashpots) provided the dynamic loads can be expressed in terms of the local vibration velocity of the structure. In a review of vortex induced flow phenomena, Marris [3] proposed to express vortex induced cross flow forces at lock-in as a cubic function of the structural vibration velocity. For simple harmonic motion the cubic model may be rearranged to yield a linear forcing term combined with a non-linear amplitude dependent restoring term known from the classical Van der Pol Oscillator. The latter form was adopted by Scanlan [4] for projection of bridge section model test results to prototype responses. The Van der Pol Oscillator concept was later adopted by Vickery and Basu [5], but within the framework of stochastic vibration theory, for assessment of vortex induced crosswind vibrations of chimneys and towers mainly of circular cross section.

3. GENERALIZED Van der POL MODEL FOR VORTEX-INDUCED FORCES

The functional relationship between response and structural damping at lock-in is not satisfactorily accounted for by the 1DOF resonant forced lift oscillator and the classical Van der Pol oscillator models. Hence a generalization of the Van der Pol model for the cross flow force F_G due to vortex shedding action is proposed which allows improved adaption to experiments:

$$F_G = \mu f C_a(1 - \varepsilon |\eta|^{2v}) \dot{\eta} \qquad (1)$$

where η, $\dot{\eta}$ are the structural displacement and velocity made non-dimensional by the cross flow dimension of the structure. $\mu = \rho D^2/m$ is mass ratio, f the oscillation frequency and C_a, ε, ν are non-dimensional fluid dynamic parameters to be determined from measurements of structural response under representative flow conditions. In FEM applications an alternative expression for F_G is useful:

$$F_G = \mu f C_a \left(1 - \frac{\varepsilon |\dot{\eta}|^{2\nu}}{(2\nu+1)(2\pi f)^{2\nu}} \right) \dot{\eta} \qquad (2)$$

Expressions (1) and (2) are equivalent provided the vortex induced response is harmonic with a well defined frequency f, which often is the case in practical applications. The non-linear forcing function given by (2) is readily modelled by non-linear dashpot elements available in a number of commercial FEM codes.

4. STRUCTURAL RESPONSE VERSUS STRUCTURAL DAMPING

The numerical values of the fluid dynamic coefficients C_a, ε, ν in (1) or (2) may be determined from response measurements on an elastic model of the structure exposed to representative flow conditions. A common type of fluid-elastic model is the section model - a rigid portion of the structure supported by linear springs.

It is assumed that the structural dynamics of the physical model in absence of flow is well approximated by the usual 1DOF free oscillator accounting for structural stiffness, inertia and viscous damping. Introducing (1) to account for the vortex shedding action, the equation of motion for the model in presence of flow, becomes:

$$\ddot{\eta} + \mu f C_s \dot{\eta} + (2\pi f)^2 \eta = \mu f C_a(1 - \varepsilon |\eta|^{2\nu}) \dot{\eta} \qquad (3)$$

For harmonic resonant motion $\eta = \eta \cos(2\pi f t)$ the inertia and stiffness terms cancels out leaving the response to be governed by damping ($\dot{\eta}$) terms only. The steady state response amplitude is thus obtained as:

$$\eta = \left[\frac{\pi}{Ic(\nu)\varepsilon} \left(1 - \frac{Sc}{C_a} \right) \right]^{\frac{1}{2\nu}} \qquad (4)$$

where the trigonometric integral

$Ic(\nu) = \int_0^{2\pi} \sin^2(p) |\cos(p)|^{2\nu} dp$ in general must be evaluated numerically.

$Sc = \zeta_s m/\rho D^2$ is a modified Scruton Number, a non-dimensional quantity proportional to the structural mass, damping and the mass of displaced fluid.

Fig. 1 displays normalized steady state response amplitudes η/η_L as function of the ratio of structural damping to aerodynamic damping Sc/C_a, for representative values of the power multiplier $\nu = 0.25, 0.5, 1.0$ and 1.5. It is noted that ν governs the curvature of the response curves. $Sc/C_a = 1$ defines the value of the Scruton Number necessary to eliminate vortex induced responses. $Sc = 0$ defines the limiting amplitude $\eta_L = (\pi/Ic(\nu)\varepsilon)^{1/2\nu}$ used for normalization of the response. $\eta/\eta_L = 1$ would be sustained for the theoretical case of vanishing structural damping or structural mass.

Presence of the trigonometric integral $Ic(\nu)$ in (4) which requires a priori knowledge of the power multiplier ν appear slightly awkward. $\pi/Ic(\nu)$ may however be approximated by a linear expression $3\nu+1$. This approximation which is accurate within 8% in the interval $0 < \nu < 1$ spanning the range likely to be encountered in practical applications.

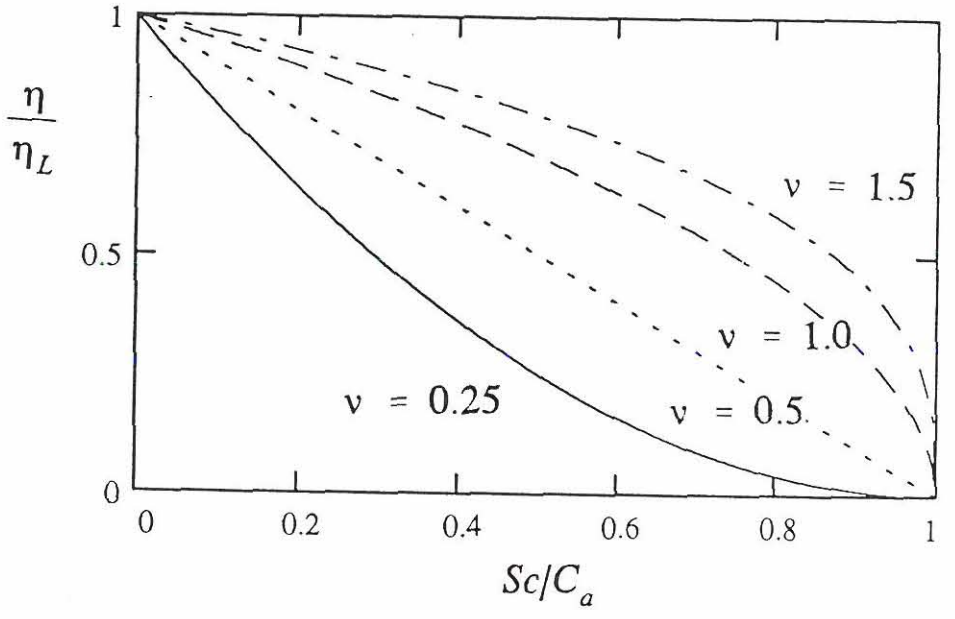

Fig. 1 Non-dimensional steady state response for the proposed generalized Van der Pol model for selected values of the power multiplier.

5. PARAMETER IDENTIFICATION AND APPLICATION

The steady state response equation (4) defines the functional relationship between expected structural response, the Scruton Number and the three fluid dynamic coefficients C_a, ε, ν sought after. Equation (4) suggests that determination of the numerical values of C_a, ε, ν may be obtained by measuring the steady state vortex induced at a minimum of three different Scruton Numbers. The fluid dynamic coefficients are then identified by matching the measured response to equation (4).

A least squares method may be adopted for matching of experimental data to the generalized Van der Pol response equation (4). The least squares fit is effectuated through an error expression comprising the sum of squares of differences between measured responses $\eta_i(Sc_i)$ and predicted responses $\eta(Sc_i,C_a,\varepsilon,\nu)$ according to (4):

$$SSQ = \sum \left[\eta_i(Sc_i) - \eta(Sc_i,C_a,\varepsilon,\nu)\right]^2 \qquad (5)$$

The solution proceeds by establishing the values of C_a, ε, ν for which the sum of squares (5) is a minimum. A task accomplished by standard data reduction routines.

Fig. 2 offers a graphical presentation of the proposed non-linear response model (full line) fitted to experimental data for a circular spring supported cylinder published by Goswami et al [6]. The figure also includes a fit of the non-linear model proposed by Marris [3] and Scanlan [4] which assumes $\nu = 1$.

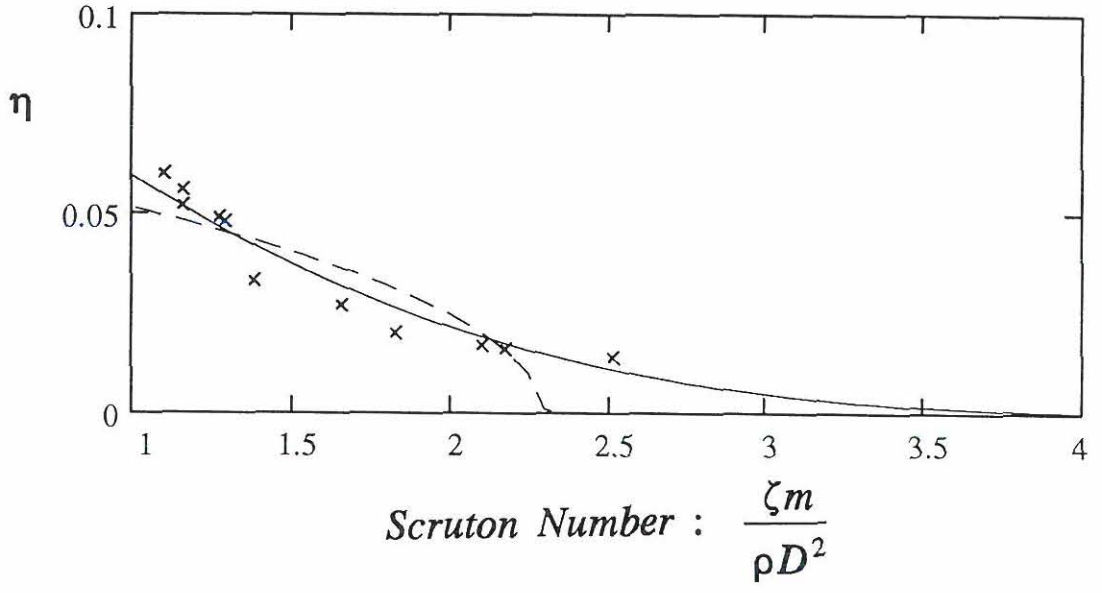

Fig. 2 Comparison of 1DOF resonant response models propsed by the present author and Scanlan [4] superimposed on experimental response data obtained for a circular spring supported cylinder [6].

From fig. 2 it is noted that the predicted generalized Van der Pol response curve (solid) maintains a slight downward curvature and appear well adopted to the trend suggested by the experimental data. Response predictions following the non-linear model proposed by Marris and Scanlan (dash) displays an upward curvature which is not quite consistent with experimental trends.

6. REFERENCES

1. SCRUTON C. On the wind-excited oscillations of stacks, towers and masts. *Wind effects on buildings and structures,* Vol. I, National Physical Laboratory, Teddington, UK, 1963.

2. SMITH B.W. and WYATT T.A. Development of draft rules for aerodynamic stability, in *Bridge Aerodynamics, Inst.Civ.Eng.*, Thomas Telford Ltd., London, 1981.

3. MARRIS A.W. A review on vortex streets , periodic wakes and induced vibration phenomena. *J.Bas.Eng.* Trans. ASME 1964.

4. SIMIU E. and SCANLAN R.H. *Wind effects on structures*, Wiley-Interscience, New York, 1978.

5. VICKERY B.J and BASU R.I. Across-wind vibrations of structures of circular cross-section, *J.Wind Eng. & Indust. Aerodyn. 12*, 1983.

6. GOSWAMI I., SCANLAN R.H. and JONES N.P. Vortex-induced vibrations of circular cylinders, I: Experimental data, *J.Eng. Mech.* ASCE 119 (11) 1993.

IDENTIFICATION AND DAMAGE DETECTION ON STRUCTURAL SYSTEMS

Rune Brincker, Associate Professor of Civil Engineering
Poul Henning Kirkegaard, Assistent Professor of Experimental Mechanics
Palle Andersen, Ph.D.-student
University of Aalborg

Abstract

A short introduction is given to system idenfication and damage assessment in civil engineering structures. The most commonly used FFT-based techniques for system identification are mentioned, and the Random decrement technique and parametric methods based on ARMA models are introduced. Speed and accuracy are discussed. Finally some commenly used damage indicators are mentioned, and the problem of identifying damage from a set of damage indicators is discussed.

Identification from dynamical response

Identification of physical properties from the dynamic response of structural systems - often called experimental modal analysis or system identification - is an area where a huge amount of research has been carried out, and where the interest for research results and practical applications is still increasing.

The growing interest for these techniques can be explained in different ways. One explanation is that computational possibilities in structural dynamics are getting better and new structural designs are introduced calling for a better and more detailed knowledge about the physical properties of the structures and how these properties are affected by damage and changes in load conditions. Another explanation is that by introduction of the computer in the measurement system, the possibility of handling large amounts of data became available, and the potential of the techniques were revealed.

The many possibilities of practical applications can be illustrated by studying one of the latest conference proceedings about experimental modal analysis, for instance one of the latest IMAC proceedings, see [15]. Only a few examples of applications will be mentioned here.

One of the first applications of structural dynamic measurement was in the 1940's where the problem of describing the loads on aircraft wings was studied and where especially the problems of flutter gave rise to experimental studies of the dynamical properties of aircraft

structures. Also, masts, chimneys and wind turbines are examples of structures where experimental studies of flutter and dynamic wind load might be wanted. Measurements on offshore structures loaded by sea waves have been performed in many locations for determination of sea loads and structural response, see e.g. Jensen [6].

Traditionally, identification of structural systems from their dynamical response has been based on the Fast Fourier Transform, Brigham [4]. The basic ideas were discovered in the forties by Danielson and Lanczos, [7], but the technique became known by the work of Cole and Tukey [8] and was implemented in larger scale from the the mid-sixties.

The standard technique is to estimate spectral density functions and fit these functions with a suitable rational spectrum model, Ewins [5]. Unfortunately, in typical cases in structural engineering, where the loading is unknown and unperiodic, the estimates based on this techique becomes biased due to leakage. However, the leakage problem might be removed by estimating correlation functons instead of spectral density functions, Brincker et al [13].

Another unparametric technique is the Random Decrement (RDD) Technique, Brincker et al [13]. The RDD technique is a fast technique for estimation of correlation functions for Gaussian processes by simple averaging.

The RDD technique was developed at NASA in the late sixties and early seventies by Henry Cole and co-workers [9-12], just a little later than the development of the FFT technique.

The basic idea of the technique is to estimate a co-called RDD signature. If the time series $x(t)$, $y(t)$ are given, then the RDD signature estimate $\hat{D}_{XY}(\tau)$ is formed by averaging N segments of the time series $x(t)$

$$\hat{D}_{XY}(\tau) = \frac{1}{N}\sum_{i=1}^{N} x(\tau + t_i)|\, C_{y(t_i)} \tag{1}$$

where the time series $y(t)$ at the times t_i satisfies the trig condition $C_{y(t_i)}$, and N is the number of trig points. The trig condition might be for instance that $y(t_i) = a$ (the level crossing condition) or some similar condition. The algorithm is illustrated in figure 1. In eq. (1) a cross signature is estimated since the accumulated average calculation and the trig condition are applied to two different time series. If instead the trig condition is applied to the same time series as the data segments are taken from, an auto signature is estimated.

In figure 2 estimation times are compared for direct estimation of the correlation function (using the definition), for estimation using the unbiased FFT and for using the RDD technique. As it appears, the RDD technique is faster that the FFT, for short estimates, up to 100 times faster.

The two techniques just mentioned are based on the same idea: to compress the data in a short interface function and then extract the physical parameters from this function by fitting an analytical model. However, information will be lost in the data compression

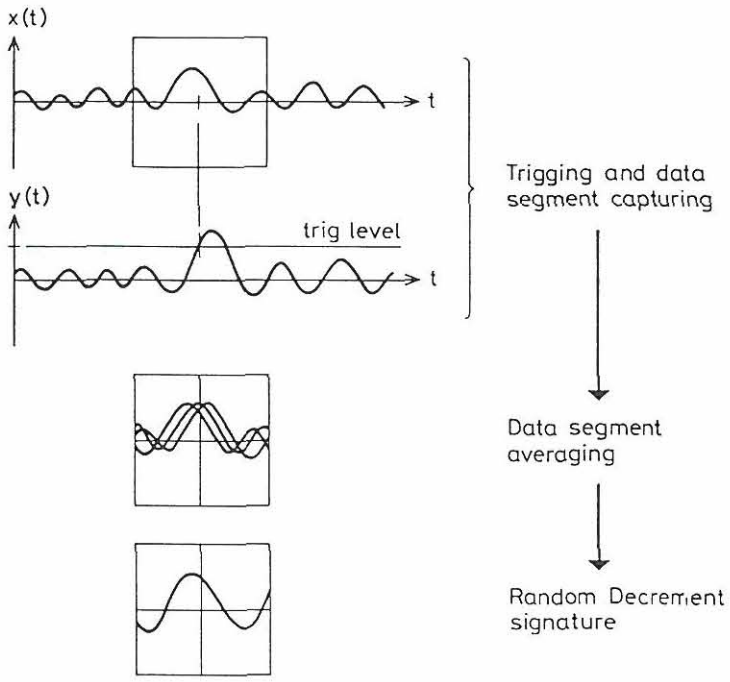

Figure 1. Determination of the Random Decrement signature.

process, because it is not possible to contain all the detailed information hidden in the time series in the estimates of correlation functions or spectral density functions.

Therefore, system parameters estimated from interface functions, will show larger variance than parameters estimated by effective fitting of models directly to the time series.

When fitting models directly to the time series, "blackbox" models in discrete time like Auto Regressive Moving Average (ARMA) models or oversized Auto Regressive (AR) models (also denoted method of maximum entropy) are frequently used, Ljung [1], Söderström and Stoica [2], Pandit and Wu [3]. These techniques has been developed mainly for applications in electrical engineering, but they are considered to be very accurate - in practice the closest one can get to unbiased effective estimators. For applications in structural engineering se e.g. Jensen [6]. In these techniques the parameter identification is based on nonlinear optimization and therefore the techniques require a relatively large computation power. However if the computation time and the time for transferring and storage of the large amounts of data can be accepted, these techniques will be an obvious choice.

An ARMA model is a parametric model given by

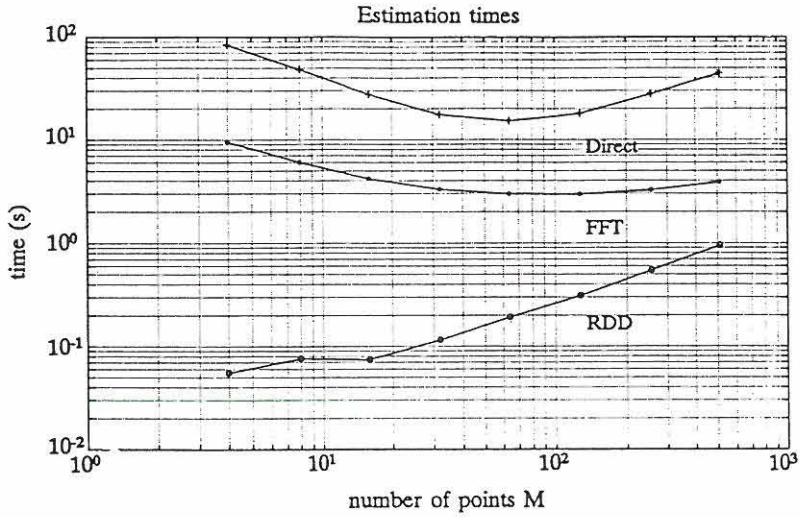

Figure 2. Times for calculation of autocorrelation function estimates by the Random Decrement technique (RDD), the Fast Fourier Transform (FFT) technique and the direct technique.

$$y(t) + a_1 y(t-1) + ... + a_{n_a} y(t-n_a) \;=\; e(t) + c_1 e(t-1) + ... + c_{n_c} e(t-n_c) \tag{2}$$

where the zero mean Gaussian white noise sequence $e(t)$ is filtered through a filter, described by the parameters a_i and c_i to give the response $y(t)$. the right-handside is the autoregressive part (AR), and the left-handside is the moving average part (MA). It can be shown, that any structural system with n degrees of freedom can be modelled as an ARMA($2n$, $2n-1$) model, Pandit et al [3], i.e., $2n$ AR parameters and $2n-1$ MA parameters. When the model order has been choosen, and the parameters has been estimated by non-linear optimization, any system parameter can be calculated by closed form solutions. Further, since the covariance matrix of the parameter set is estimated together with the parameter vector itself, confidence limits on any physical parameter might easily be calculated.

In practice however, the choice between the different techniques is governed by a trade-off between accuracy and speed, and sometimes it is beneficial to accept a small incease in variance for a large decrease in the time used in the estimation process.

The difference in estimation time might by quite large. To illustrate the difference the slowest, but most accurate technique (ARMA) is compared to the fastest possible at the moment (RDD), figure 3. Eigenfrequency and damping is estimated for a single degree

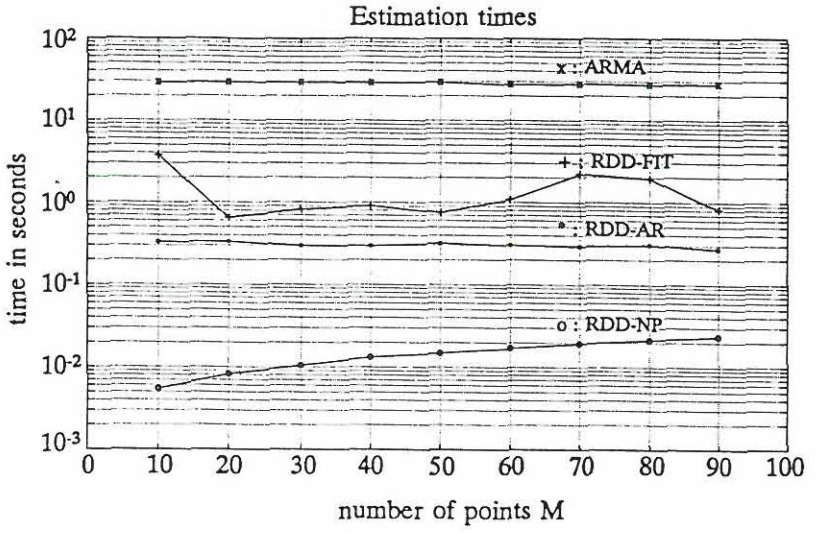

Figure 3. Estimation times for different techniques as a function of the length M of the one-sided auto correlation estimate.

of freedom system. In figure 3 three different curves are shown for the RDD technique, fitting of the theoretical correlaton function (RDD-FIT), fitting an AR model the the correlation function estimate (RDD-AR) and using a simple non-parametric technique to estimate the two quantities (RDD-NP). As it appears the estimation time differ by a factor of 1000-5000.

Damage Detection

One of the interesting applications of structural system identification is damage detection. When a specimen or even a large complex structure is damaged, the damage will cause a change of the dynamic properties. For instance if a structural member is cracked, the crack will decrease the stiffness and thereby decrease the eigenfrequencies of the structure and it may increase the damping due to local plasticity and thereby change the energy flow and the overall damping of the structure.

It is important to emphasize however, that there is no safe way at the moment for an accurate damage identification. The problem of finding out what kind of changes a certain damage might cause is usually not a great problem. The opposite problem however, the problem of identifying a certain damage for a given change of the structural response is a very difficult task - and at the present time - a problem that has not been solved.

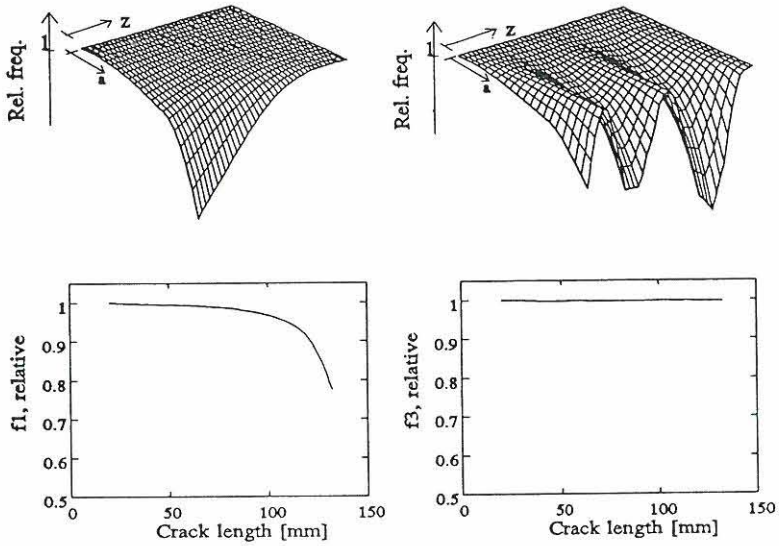

Figure 4. Result for a cantilever beam with box section (80 × 40 mm). Upper figures: Variantion of the first and the third natural frequency with crack position z along the beam and crack lenth a. Lower figures: Experimental results for a certain crack location.

In practise therefore, the application of these techniques is limited to cases where it is of importance to know whether or not significant structural changes has taken place, and if some changes has taken place - to be able to indicate the type and location of a possible damage.

A fine rewiev of the different damage indicators is given by Rytter [14]. Some examples will be given here.

The simplest and most important damage indicators are may be the changes of the eigenfrequencies. The eigenfreqencies can easily be measured with large accaracy, and if the eigenfrequencies are sensitive to the kind of damage in quistion, they might be well suited as damage indicators. The sensitivety is illustrated in figure 4.

Also the damping ratios might be used as damage indicators. In figure 5 is shown a phase-plan plot for a beam in the undamaged and the damaged state (a small crack develloped). The test results show clearly a large increase in damping.

If one has estimated a large number of damage indicators d_i together with their corresponding standard deviations σ_i, a simple unified damage measure might be defined by taking the sum

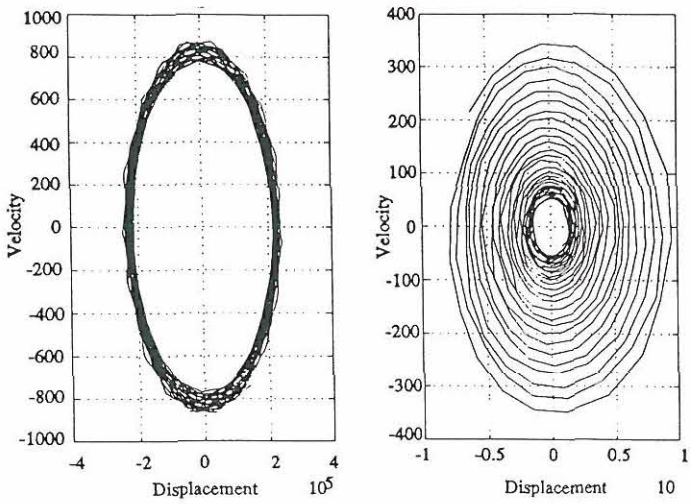

Figure 5. Phase-plan plots for a cantilever beam with box section (80 × 40 mm) in the undamaged state (left) and in the damaged state (right).

$$D = \frac{|d_1 - d_{10}|}{\sigma_1} + \frac{|d_2 - d_{20}|}{\sigma_1} + \ldots \tag{3}$$

where d_{i0} is the damage indicators corresponding to the undamaged (virginal) state.

Mode shapes might be included. One way to do this is to use the modal assurance criterion calculating a socalled MAC matrix for two eigenvectors. A socalled COMAC vector might also be calculated. Some experimental results are shown in figure 6.

A certain class of damage indicator are of great importance however. This is the class of parameters indicating an increase in the non-linear behaviour of the structure. Consider the phase-plan plot in figure 5. The damaged beam show a clear unsymmetry in the phase plan plot indicating a change in stiffness when the bending change sign. The phenomenon is due to the opening and the closing of the crack. Other non-linear indicators are new peaks appearing in the power spectrum and changes in the response statistics.

The most important findings in the latest year is probably the use of neural networks in the damage detection problem. Neural networks are computational models loosely inspired by the neuron architecture and operation of the human brain. Many different types of neural networks exist. Among these the multilayered neural network trained by means of the back-propagation algorithm are currently given greatest attention by application developers.

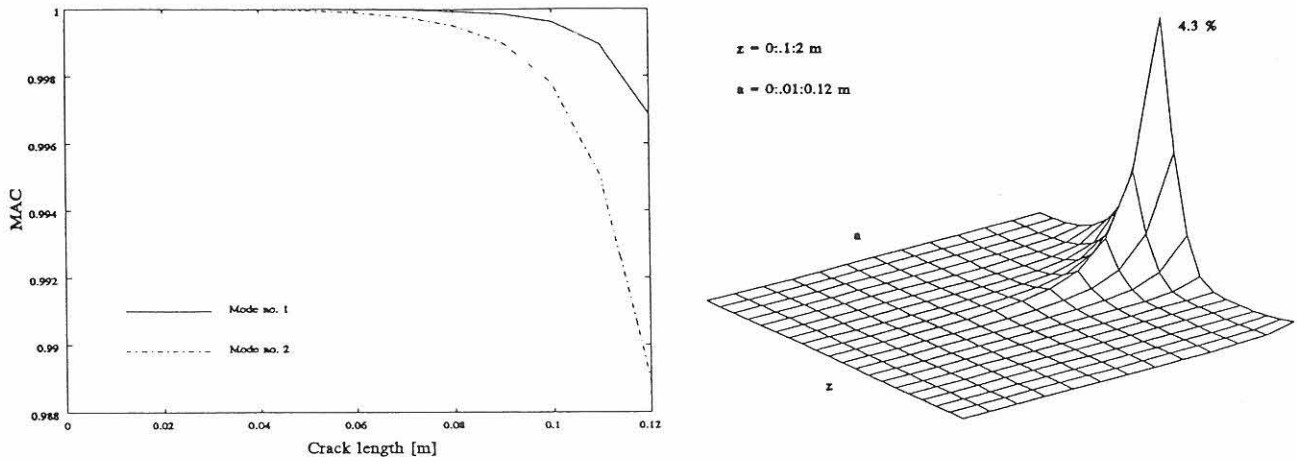

Figure 6. Result for a cantilever beam with box section (80 × 40 mm). Left figure: MAC values for mode 1 and 2. Right figure: COMAC values for mode 1 and 2.

When the neural networks are used in damage detection, the networks are trained by introducing different kinds of damage in the structure and calculating the corresponding changes in the actual damage indicators. Then, after training the network, it might be used for indifying the kind of damage for a given set of damage indicator obtained from measurements. The method has proven to be successfull on real structures, Kierkegard et at [15], Rytter et al [16].

References

[1] Ljung, Lennart: "System Identification - Theory for the User". Prentice-Hall, Inc., 1987.

[2] Söderström, T. and P. Stoica: "System Identification". Prentice Hall, 1987.

[3] Pandit, S.M. and S. WU: "Time Series and System Analysis with Applications". John Wiley and Sons, 1983.

[4] Brigham, E.O.: "The Fast Fourier Transform". Prentice-Hall, Inc., 1974.

[5] Ewing, D.J.: "Modal Testing: Theory and Practise". Research Studies Press, LTD. and Bruel and Kjaer, 1986.

[6] Jensen, J.L.: "System Identification of Offshore platforms", Ph.D.-thesis, Dept. of Building Technology and Structural Engineering, University of Aalborg, 1990.

[7] Danielson, G.C. and C. Lanczos: "Some Improvements in Practical Fourier Analysis and Their Application to X-ray Scattering From Liquids". J. Franklin Inst., Vol. 233, pp. 365-380, 435-452, 1942.

[8] Cooley, J.W. and J.W. Tukey: "An Algorithm for the Machine Calculation of Complex Fourier Series". Mathematics of Computation, Vol. 19, pp. 297-301, April 1965.

[9] Cole, A. Henry: "On-the-line Analysis of Random vibrations". AIAA/ASME 9th Structures, Structural and Materials Conference, Palm Springs, California, April 1-3, 1968.

[10] Cole, A. Henry: "Failure Detection of a Space Shuttle Wing Flutter by Random Decrement". NASA, TMX-62,041, May 1971.

[11] Cole, A. Henry: "On-line Failure Detection and damping Measurement of Space Structures by Random Decrement Signatures". NASA, CR-2205, March 1973.

[12] Chang, C.S.: "Study of Dynamic Characteristics of Aerodynamic Systems Utilizing Randomdec Signatures". NASA, CR-132563, Febr. 1975.

[13] Brincker, R., S. Krenk, P.H. Kirkegaard and A. Rytter: "Identification of Dynamical Properties from Correlation Function Estimates". Bygninsstatiske Meddelelser, Vol. 63, No. 1, 1992.

[14] Rytter, A.: "Vibrational Based Inspection of Civil Engineering Structures", Fracture & Dynamics Paper No. 44, May 1993, Ph.D. thesis, Dept. of Building Technology and Structural Engineering, Alborg University.

[15] Kirkegaard, P.H. and A. Rytter: "Use of Neural Networks for Damage Assessment in a Steel Mast", Proc. of the International Modal Analysis Conference, Honolulu, Hawaii, 1994.

[16] Rytter, A. and Kirkegaard: "Vibrational Based Inspection of a Steel Mast", Proc. of the International Modal Analysis Conference, Honolulu, Hawaii, 1994.

Damage Assessment of a Steel Lattice Mast under Natural Excitation

P. H. Kirkegaard

Department of Building Technology
Aalborg University
Sohngaardsholmsvej 57, 9000 Aalborg, Denmark
e-mail: I6PHK@SV1.BUILD.AUC.DK

A. Rytter

Applied Mechanics Unit, Ispra, Italy

Abstract: In this paper the possibility of detecting and locating damages in a 20 m high steel lattice mast subjected to natural excitation has been investigated. For the damaged mast seven different damage states were considered. In these damage states a damage was assumed in one of the lower diagonals. These diagonals were cut and provided with a bolted joint implying that a damage could be simulated. Based on 20 periodical measurements during 6 months the sensitivity of the modal parameters, identified by an ARMA-model, to environmental conditions such as wind-direction, wind-speed and air-temperature have been investigated. These sensitivities have been compared with the changes of modal parameters due to a damage. It is found that the measured natural frequencies vary less than one per cent while the measured modal damping ratios vary more than twenty per cent due to different environmental conditions. The measured bending natural frequencies and the measured rotational frequency approximately decrease few per cent and more than ten per cents, respectively, due to a damage corresponding to a removal of one of the lower diagonals. The results also show that a neural network trained with simulated data is capable for detecting location of a damage in the steel lattice mast when the network is subjected to the experimental data.

Keywords. System identification, ARMA-model, damage detection, civil engineering application, neural networks.

1. Introduction

Structural diagnosis by measuring vibrational signals of civil engineering structures is a subject of research which has received increasing interest during the last decades. The main impetus for doing vibrational based inspection (VBI) is caused by a wish to establish an alternative damage assessment method to the more traditionally methods such as e.g. visual inspection. Many research projects have concluded that it is possible to detect damages in civil engineering structures by VBI, and some techniques to locate damages in civil engineering structures have also been proposed. However, much of the performed research has been based on numerical simulations and on laboratory models. A throughout review of VBI techniques can be found in Rytter [1].

In order to use VBI techniques it is necessary to be able to obtain reliable estimates of the dynamic characteristics, e.g. natural frequencies. Such quantities can be estimated from the resulting output caused by a known well-defined input. However, the estimates can also be estimated by using the so-called ambient testing, i.e. the only excitation on the structure is the natural excitation.

The aim of the research presented in this paper was to answer the following questions by using full-scale measurements based on natural excitation:

1) Is it possible to distinguish between changes in modal parameters due to effects produced by damages and those brought about as a result of changes in the ambient environmental conditions ?

2) How sensitive are measured modal parameters to a damage ?

3) Can the location of the damages be estimated ?

In order to answer these questions a 20 m high steel lattice mast subjected to wind excitation was experimentally investigated. The experimental arrangement are described in section 2. In section 3 the experimental results are presented and discussed and at last in section 4 conclusions are given.

2. Experimental Arrangement

An elevation of the 20 m high steel lattice test mast is shown in fig. 2.1. The four chords K-frame test mast with a 0.9x0.9 m cross-section was bolted with twelve bolts, three for each chord, to a concrete foundation block founded on chalk and covered by sand. The mast was constructed with welded connections. At the top of the mast two plywood plates were placed in order to increase the wind-area.

The eight lower diagonals were cut and provided with a bolted joint. Each bolted joint consists of 4 slice plates giving the possibility of simulating a 1/4, 1/2, 3/4 and full reduction of the area of a diagonal. A damage was simulated by removing one or more splice plates in these bolted joints. Seven different damage states (1,2,5,6,9,10,11) were considered. The damage state 1,2,5 and 6 correspond to a removal of diagonal AB101, BC101, AB102 and BC102, respectively, see fig. 2.2. Damage states 9 and 11 correspond to fifty per cent reduction of the sectional area of diagonal AB101 and AB102, respectively. Damage state 10 corresponds to fifty per cent reduction of the sectional area of diagonal AB101, BC101, CD101 and DA101.

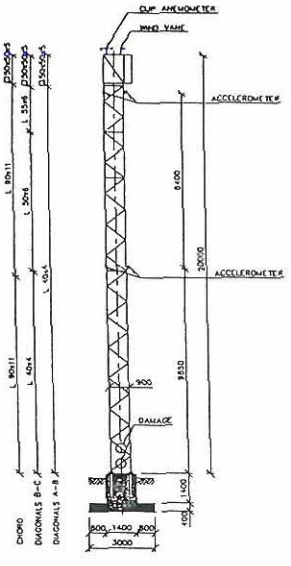

Fig. 2.1 Elevation of Mast.

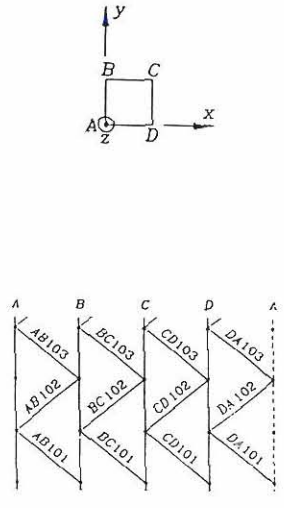

Fig. 2.2 Diagonals of the lower two sections

The mast was instrumented with instruments to measure the accelerations, wind-direction (wind-vane) and wind-speed (cup-anemometer). Further, the ambient air temperature was measured. The data acquisition and the analyse of the sampled data by an ARMA-model were performed with the MATLAB, see PC-MATLAB [2], based on program to Structural Time Domain Identification, STDI, see Kirkegaard et al. [3]. A throughout description of the test arrangement can be found in Kirkegaard et al. [4].

3. Experimental Results and Discussion

In the period from December 92 to June 93 twenty measurements sessions were performed with the undamaged mast . The dates of the sessions were selected in such a way that a data base containing measured responses due to different wind-directions and wind-speeds were created. At a measurement session 10 time series were recorded for each transducer, i.e. accelerometers as well as cup-anemometer and wind-vane. In the same period 2 measurement sessions were performed where damages were simulated at the mast. In the period the lowest and the highest air temperature were -5^oC and 20^oC, respectively.

3.1 Modal Parameters of the Undamaged Mast

It was the natural bending frequencies no. 1 and no. 4, the natural bending frequencies no. 2 and no. 5 and the natural frequency no. 3 corresponding to deflection parallel to the x-axis and deflection parallel to the y-axis and rotation, respectively, which were estimated.

The estimates of the natural frequencies and the modal damping ratios are shown as function of the measurement number in fig. 3.1. The 20 estimates in each figure have been obtained by combining the measured estimates of natural frequencies and modal damping ratios, respectively, from each measurement session by weighting with the standard deviations. At each measurement session 10 times series were recorded, implying 10 estimates of the natural frequencies and modal damping ratios. respectively.

The solid lines in fig. 3.1 indicate a mean value of the 20 estimates while the dashed lines give an interval between the mean value plus one per cent and the mean value minus one per cent for the natural frequencies. In the same way an interval corresponding to the mean value plus ten per cent and the mean value minus ten per cent is shown with dashed lines for the modal damping ratios. Fig. 3.1 shows that the measured natural frequencies vary approximately only few per cent while the modal damping ratios vary more than twenty per cent. It is seen that the bending natural frequencies are more sensitive than the rotational frequency. The standard deviation of the natural frequencies and modal damping ratios are approximately 0.003 Hz and 0.001, respectively. This indicates that the variation of the measured modal parameters is due to changes in the environmental conditions and only not due to randomness. In order to investigate the sensitivity of natural frequencies with respect to wind-direction and wind-speed the 200 estimates of the natural frequencies are shown in fig. 3.2a as function of the wind-speed. The estimates have been divided into 4 groups. Each group corresponds to a wind-direction interval of 90 degrees. Fig. 3.2a shows that the natural frequencies are sensitive to the wind-speed. However, it is most clear for the first and second natural frequency. Further, it is seen that the natural frequencies have an increase for a wind-speed corresponding to 7-8 m/s when the wind-direction is changed. However, this change can also be a consequence of a change in temperature. In fig. 3.2b the 200 estimates of the natural frequencies are shown as a function of the wind-speed. The estimates have been divided into 2 groups. corresponding to estimates obtained from measurements where the air temperature was lower than 0^oC and higher than 0^oC, respectively. It is seen that the increase in natural frequencies for a wind-speed corresponding to 7-8 m/s can be due to an air temperature below 0^oC and not necessarily a change in the wind-direction. However, more data most be obtained in order to investigate this problem.

3.2 Modal Parameters of the Damaged Mast

In fig. 3.3a and 3.3b the measured natural frequencies from measurement sessions 4 and 6 are shown as a function of damage state, respectively. The solid lines in fig. 3.3a show the lower bound of the 95% confidence level of the natural frequencies from measurement session 3. The estimates are assumed Gaussian distributed. In the same way in fig. 3.3b the lower bound of the 95% confidence

level of the natural frequencies from measurement session 5 is shown. The measurement sessions 3 and 5 (undamaged) correspond to measurement sessions 4 and 6 (damaged), respectively, with respect to environmental conditions, i.e. approximately the same wind-speed, wind-direction and air-temperature. This means that a change in the measured natural frequencies can be interpreted as a change due to a damage and not to a change in the environmental conditions. Fig. 3.3 shows that it is possible to detect a damage in the mast corresponding to a removal of one of the lower diagonals, damage states 1,2,5 and 6. Further, a damage, damage states 9 and 11, corresponding to a fifty per cent reduction of the sectional area can also be detected. However, if such a damage should be detected it is important to compare modal parameters from the damaged and undamaged mast, respectively, obtained under the same environmental conditions.

3.3 Estimation of Damage Location by use of Neural Network

The applicability of a neural based damage assessment method, see e.g Hertz et al. [5] and Kirkegaard et al. [6], is investigated by training a neural network with the relative changes of the natural frequencies of the 5 lowest modes. These changes were estimated for a 20, 40, 60, 80 and 100 per cent reduction of the sectional area of diagonal AB101, BC101, AB102 and BC102, respectively. Further, the relative changes of the frequencies also were estimated for the undamaged mast. By a trial-and-error approach it is found that a 4 layers neural network with 5 input nodes, 5 nodes in each of the two hidden layers and 4 output nodes gave the network with smallest output error. Each output node corresponds to a damage in one of the diagonals AB101, BC101, AB102 and BC102, respectively. The value for a single diagonal adopts the value 1 when not damaged, the value 0 when totally damaged and 0.2 corresponds to a 80 per cent reduction of a sectional area etc.

The network was tested by subjecting the simulated input data corresponding to a 100 per cent reduction of the sectional area of the four diagonals AB101, BC101, AB102 and BC102, respectively, to the network. It was found that the neural network was capable of reproducing the location and size of a damage used in training (Damage state 1,2,5,6). Table 1 shows the outputs from the network subjected to experimental data.

Output Node No.	Damage State					
	1	2	5	6	9	10
1(AB101)	0.1	0.8	0.9	0.9	0.5	0.8
2(BC101)	0.8	0.1	0.8	1.0	0.7	0.4
3(AB102)	0.6	1.0	0.1	1.1	0.2	0.2
4(BC102)	0.9	0.9	0.9	0.0	0.9	1.1

Table 1: Results from network subjected to experimental data.

The results in table 1 show that it is possible to detect a damage corresponding to a removal of a diagonal (Damage state 1,2,5,6) by the neural network approach. It is also seen that a damage corresponding to 50 per cent reduction of the sectional area of a diagonal AB102 can be detected, but not quantified.

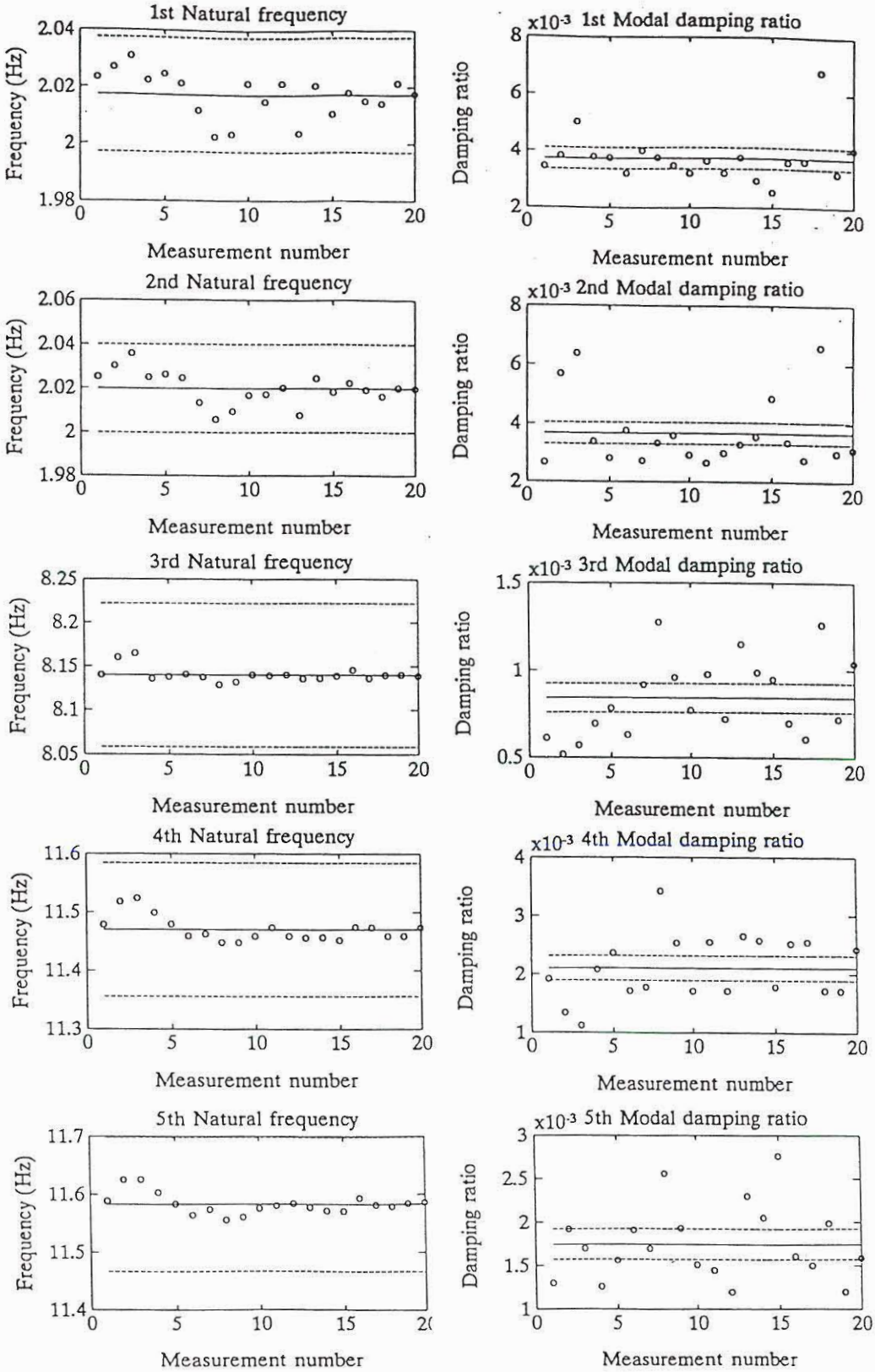

Fig. 3.1. Estimated natural frequencies and modal damping ratios as a function of measurement number. (Solid lines show the mean value and dashed lines show the mean value plus/minus one per cent and plus/minus ten per cent for the natural frequencies and the modal damping ratios, respectively).

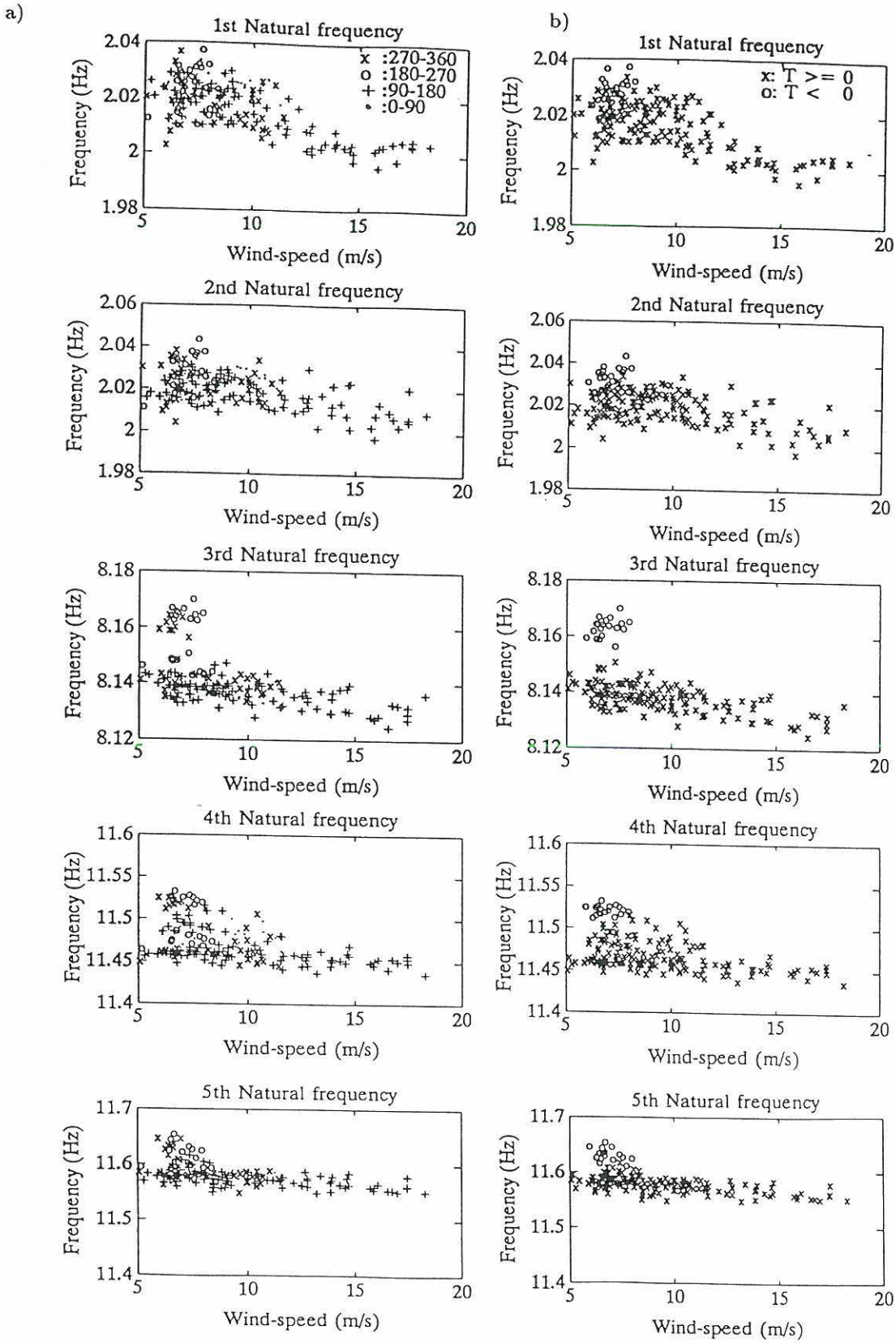

Fig. 3.2. Natural frequencies as a function of wind-speed and wind-direction (a) and as a function of wind-speed and air temperature (b).

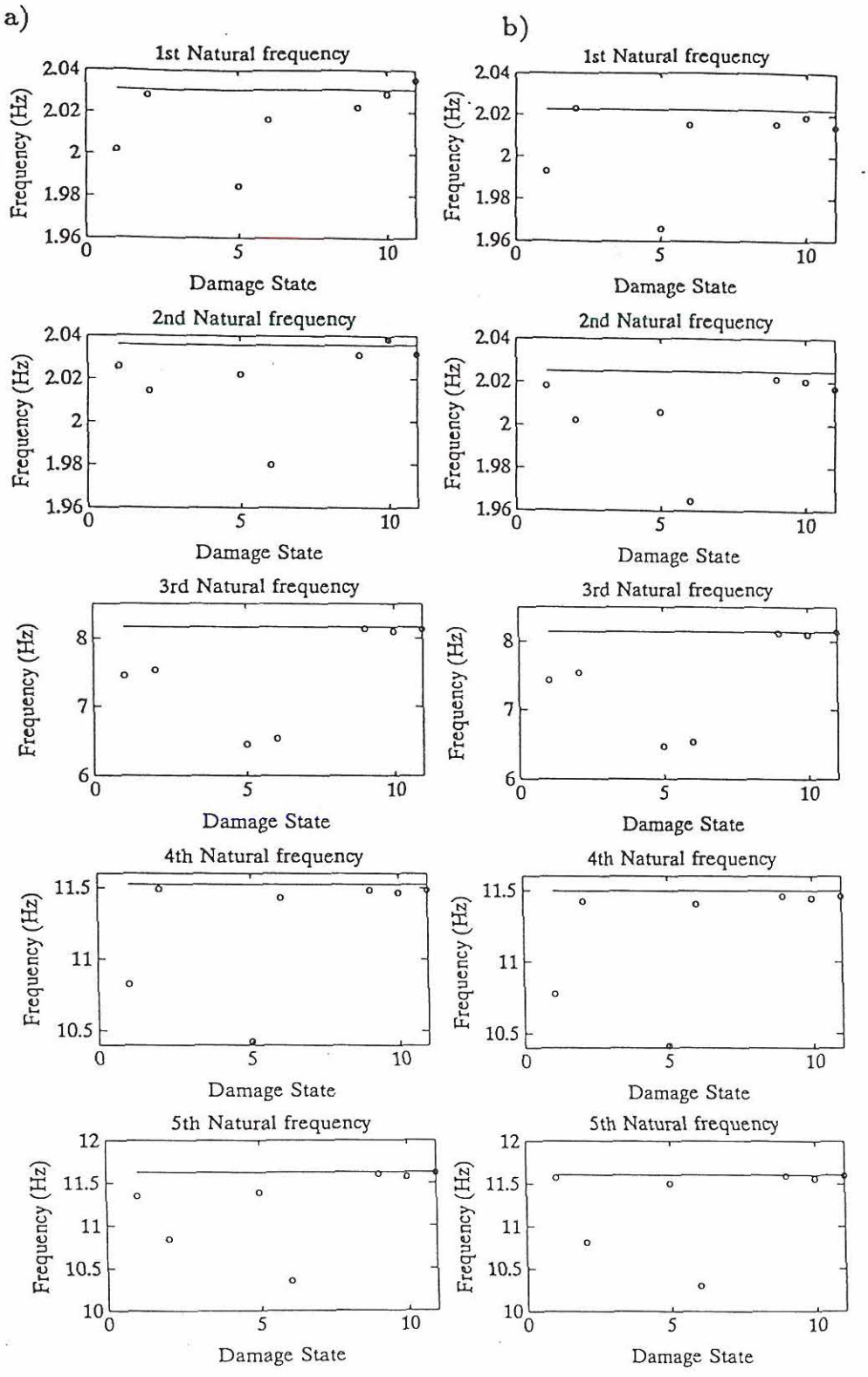

Fig. 3.3 Estimated natural frequencies from measurement session 4 (a) and 6 (b) as a function of damage state. (Solid lines are the lower bound of the 95% confidence level for estimated natural frequencies from measurement sessions 3 (a) and 5 (b), respectively)

4. CONCLUSIONS

In this paper the natural frequencies and modal damping ratios of a 20 m high steel lattice mast subjected to natural excitation have been experimentally investigated. The conclusions of the paper can be stated as follows:

- Measured natural frequencies vary less than one per cent while the measured modal damping ratios vary more than twenty per cent due to different environmental conditions, such as wind-speed and air-temperature
- The measured bending natural frequencies and the rotational frequency approximately decrease few per cent and more than ten per cent, respectively, due to a damage corresponding to a removal of one of the lower diagonals.
- It is possible to detect a damage corresponding to a removal of a diagonal using a system identification technique (ARMA) based on natural excitation. A fifty per cent reduction of the sectional area of a diagonal can be detected, if the measured modal parameters from the damaged mast and the undamaged mast, respectively, are obtained under the same environmental conditions.
- A neural network trained with simulated data is capable for detecting location of a damage, corresponding to a removal of a diagonal when the network is subjected to experimental data.

4. REFERENCES

[1] Rytter, A.: Vibration Based Inspection of Civil Engineering Structures. Ph.D-thesis, Aalborg University, Denmark, 1993.

[2] PC-MATLAB for MS-DOS Personal Computers, The Math Works, Inc., 1989.

[3] Kirkegaard, P.H. & R. Brincker: STDI: Program for Structural Time Domain Identification. University of Aalborg, 1993.

[4] Kirkegaard, P.H. & A. Rytter: An Experimental Study of the Modal Parameters of a Damaged Steel Mast. Fracture and Dynamic Paper No. 45, University of Aalborg, 1993.

[5] Hertz, J., A. Krogh & R.G. Palmer: Introduction to the Theory of Neural Computation. Addison-Wesley, Redwood City, CA, 1991.

[6] Kirkegaard, P.H. & A. Rytter: Use of Neural Networks for Damage Detection and Location in a Steel Member. Proceedings of the third International Conference on Use of Artificial Intelligence in Civil Engineering, CIVIL-COMP93, 1993.

Dynamic Response of Breakwaters

by

Hans Falk Burcharth

Wind generated storm waves cause dynamic loads on breakwaters. The problems related to the structural response depend on the type of structure. In case of monolithic structures, like sandfilled concrete caissons, the problems are associated with the overall stability of the monolith and not with the structural members, i.e. the front plate of the caisson. In case of rubble mound structures the problems are related to the integrity of the slender types of concrete armour units, and to the stability of super structures (parapet walls), if present.

The presentation will discuss the present stage of knowledge associated with the problems of designing breakwater structures. For the case of rubble mound structures a method of designing armour layers made of slender unreinforced concrete units has been developed. For the other cases no saticfactory methods exist so far but research is ongoing.

Development of pore pressure and material damping during cyclic loading

L.B. Ibsen, Aalborg University, Denmark

ABSTRACT: The behaviour of sand during cyclic loading can be characterized as "stabilization", "instant stabilization", "pore pressure buildup" and "liquefaction". The terminologies can be defined exactly by a simple mathematical formulation based on the existence of a cyclic stable state. By introducing a mobilization index M it is possible to describe the strongly hysteretic behaviour during loading and unloading, even if the stress path is complicated.

INTRODUCTION

In the last thirty years a great number of test series with cyclic loading of sand have been performed, many phenomena have been described and important theories have been presented. Today the main problem is to gather all relevant information in a consistent mathematical formulation.

Laboratory testing gives a possibility to study soil behaviour in details. However, it is widely recognized that it is not possible to use laboratory test results for practical purposes without calibrating them against field tests and field observations.

For instance, the preparation of a sand specimen and the reconstruction of stress history and seismic history have a major effect on the cyclic behaviour. In most natural deposits, soil elements are subjected to shear stresses corresponding to the "earth pressure of rest" situation. In earth structures close to natural slopes or beneath foundations, soil elements are subjected to even larger shear stresses. The stress history is reconstructed by anisotropic consolidation before cyclic testing.

An old sand deposit in an earthquake region has been vibrated many times in its lifetime and the specimen should therefore be prepared by a vibration technique at a level corresponding to the seismic history.

The success of laboratory testing depends on the extent to which the in-situ characteristics are reestablished.

The purpose of this paper is therefore limited to describe in mathematical formulations the phenomena involved in soil response on cyclic loading, and to give a definition of the terminologies, which are already accepted, but not clearly defined. It combines the two different assumptions

i) Alternating loads build up pore pressure, and liquefaction will develop if the amplitude or the number of cycles are big enough (initiated by Seed and Lee in 1966).

ii) The initial effective stress state and the relative density of the soil play a definitive role for the behaviour of a soil. If the initial shear stress exceeds a certain value the pore pressure will be reduced by cyclic loading and the soil will stabilize (Casagrande 1976, Castro and Poulus 1977, Loung 1980).

The paper is based on triaxial tests on a uniform sand called Lund no 0. The mean diameter $d_{50} = 0.4\ mm$, the coefficient of uniformity $U = 1.7$, the initial void ratio 0.62 corresponding to a density index $I_D = 0.7$. The test specimens were prepared by a pluvial technique and carefully saturated in vacuum. A test consists of an anisotropic consolidation phase followed by cyclic loading at constant volume.

STATIC BEHAVIOUR OF DENSE SAND

The parameters, which describe the state of a soil under axisymmetrical stress conditions, are

$$\begin{aligned} &\text{the mean normal stress} && p' &&= \frac{1}{3}(\sigma_1' + 2\sigma_3') \\ &\text{the deviator stress} && q' &&= (\sigma_1' - \sigma_3') \\ &\text{the volumetric strain} && \varepsilon_v &&= \varepsilon_1 + 2\varepsilon_3 \\ &\text{the distorsion} && \varepsilon_q &&= \frac{2}{3}(\varepsilon_1 - \varepsilon_3) \end{aligned} \qquad (1)$$

where σ_1 is the vertical and σ_3 the horizontal pressure.

The strength of a soil is normally described by the Mohr-Coulomb's failure criterion. "Failure" is defined as a state where q is maximum, and corresponds normally to a distorsion $\varepsilon_q = 5 - 10\%$. The strength parameters c' and φ' are assumed to depend on the void ratio only. In Figure 1 is shown the failure line corresponding to $e = 0.62$.

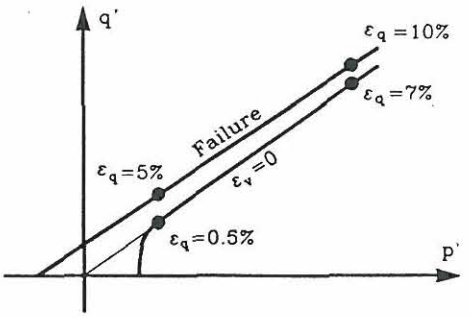

Figure 1. Stress path in an undrained test compared with the Mohr-Coulomb failure criterion.

In a stress state with very small deviatoric stresses the behaviour of a sand is contractive, but when q' increases a dense sand dilates. However, it is not possible to cut up the $q'-p'$ stress-space in a contractive and a dilative zone, because changes in ε_v depend on stress increments.

The stress path for an undrained test is shown in Figure 1. It is of particular interest because the first cycle on cyclic loading has to follow a similar stress path. It must be emphasized that for normal stress levels this stress path does not describe an undrained failure state, because the destorsion is too small, only $\varepsilon_q \approx 0.5 - 1.0\%$. At very high stress levels $\varepsilon_q = 5 - 10\%$ and failure can occur. We can conclude that the first cycle in an undrained cyclic test has limited strains.

MOBILIZATION INDEX M

The deviator stress q' can be normalized by introducing a mobilization index M

$$M = q' / \left| q'_f \right| \quad ; \quad -1 < M < 1 \tag{2}$$

where q'_f corresponds to the actual mean normal stress p'.

The advantage of using a mobilization index instead of the often used stress ratio $(\sigma'_1 - \sigma'_3)/\sigma'_3$ is obvious: It is possible to compare tests with different soil and densities, because q' is normalized with respect to the strength of the soil. M can be used with success even for curved failure envelopes and as mentioned later a mathematical description of hysteresis is possible even for large strains and complicated stress variations.

The mobilization index is introduced in Figure 2. The drained, anisotropic stress state (p'_o, q'_o) just before cyclic loading is then (p'_o, M°_m). During cyclic loading the amplitude A is constant and the maximum value of M at each cycle is:

$$M_{max} = \frac{q'_o + A}{A} M_m = k\, M_m \tag{3}$$

where k is the amplitude ratio and M_m is the mean value of M.

CYCLIC TRIAXIAL TESTS

In triaxial tests the loads, movements, volume, and pore pressure are measured on the outside of the test specimen, and it is essential to have homogeneous conditions inside the specimen in order to achieve correct values of stresses, strains, and void ratio. The height of the specimen is therefore equal to the diameter, and smooth pressure heads are used. But in extension it is impossible to avoid inhomogeneous strains at failure where "necking" occurs, preventing the strain and stresses from being calculated correctly.

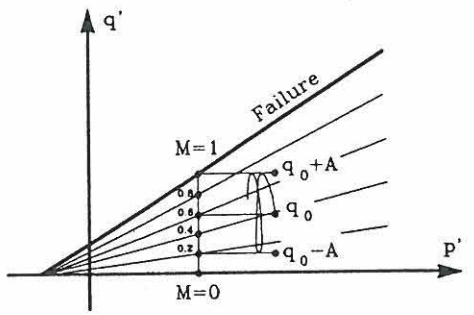

Figure 2. Normalization of the deviator stress q. Variation of M during cyclic loading.

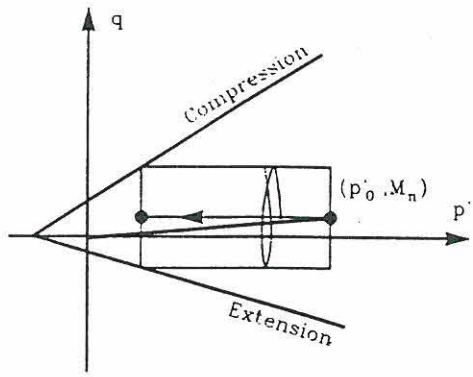

Figure 3. Simultaneous liquefaction in compression and extension. Risk for necking.

The Mohr-Coulomb failure criterion is unsymmetric in triaxial compression and extension, because the intermediate normal stress changes from σ'_{min} to σ'_{max}.

$$\begin{aligned} \text{In compression:} \quad q'_f &= \frac{6 sin\varphi'}{3 - sin\varphi'} (p' + c' cot\varphi') \\ \text{In extension:} \quad q'_f &= \frac{-6 sin\varphi'}{3 + sin\varphi'} (p' + c' cot\varphi') \end{aligned} \tag{4}$$

If q' varies symmetrically $M_m = sin\varphi'/(3 + sin\varphi')$ at failure. Failure then takes place simultaneously in compression and extension (Figure 3). If $M_m < sin\varphi'/(3+sin\varphi')$ at failure necking takes place. The corresponding initial value of M_m is given by

$$M^\circ_m < M_n = \frac{1}{18} (3 - sin\varphi) \frac{A}{p'_o} \tag{5}$$

In tests with $M^\circ_m = M_n$ the strains in loading and reloading are almost identical, and the cyclic stress-strain curves are reversible.

CYCLIC PHENOMENA

The stable state M_s

It is now postulated that a stable state exists at a certain mobilization index M_s, where the positive and negative pore pressure generated during a loading cycle neutralize each other, provided that $|M_{max}| < 1$. In the stable state the stress variation during a loading cycle does not change anymore. The stable state M_s has been verified in an extensive test series, shown in Figure 4. The initial value of M_m, the confining pressure, the amplitude and the number of cycles vary from test to test, but the number of cycles, N, is large enough to ensure that the last hundreds of cycles takes place in the stable state, where the stress paths do not change.

Stabilization

It is seen that when $M^\circ_m > M_s$ then negative pore pressure will develop and the effective stress level will increase until the stable state is reached. This phenomenon is called "stabilization". If $M^\circ_m >> M_s$ then "instant stabilization" takes place.

Pore presssure buildup and liquefaction

If $M_m < M_s$ and $|M_{max}| < 1$ a positive pore pressure will be generated and the effective stress level will decrease until the stable state is reached. This phenomenon is called "pore pressure buildup".

If M_{max} equals 1 during pore pressure buildup, the hysteretic strains get very large ($\varepsilon_q = \pm 10\%$), the testing equipment looses all control, and the peak pore pressure in each cycle rises to the confining pressure. This ultimate state is called "liquefaction". It is well documented in many test series.

Mathematical formulation

A simple description of this phenomenon is given by:

$$\begin{aligned} M_m &= M_m^\circ + (M_s - M_m^\circ)\, f(N) \\ M_{max} &= k \cdot M_m \leq 1 \end{aligned} \tag{6}$$

where $f(N)$ is a function of the number of cycles. $f(N) = 0$ for $N = 0$ and $f(N) \to 1$ for $N \to \infty$. Thus

$$f(N) = \left(\frac{N}{N + N_o}\right)^{\ell} \tag{7}$$

ℓ is rather close to 1. In analysis of liquefaction risks during earthquakes an advantageous value of ℓ is 1.25.

N_o depends on M_m° as indicated in Figure 5, which is based on results from a larger number of tests than shown in Figure 4. It is seen that

$$N_o = 4 \cdot \left(\frac{1 - M_m^\circ}{M_m^\circ}\right) \tag{8}$$

M_m° is at the actual stress level limited upwards: $M_m^\circ < 0.8$.

Figure 6 shows the three possible developments of M_m and M_{max} during cyclic loading as given by formulas (6), (7), (8).

STRESS VARIATION DURING CYCLIC LOADING

Figure 7 shows some examples of stress variations during cyclic loading, which corresponds to the phenomena defined earlier.

The first loading ($N = 1$) always follows the stress path in a static undrained test. and the corresponding value of M is always lesser than one. This causes in Figure 7 b) a negative pore pressure big enough to stabilize the sand almost immediately.

As the cyclic loading goes on the distorsion grows bigger and bigger and when $\varepsilon_q \approx 5 - 10\%$ the maximum value of M is able to reach 1. In Figure 7 d) liquefaction can occur.

In tests where $M_m^\circ < M_n$, necking can give big distorsions and liquefaction after a few cycles.

HYSTERETIC BEHAVIOUR OF SAND

The behaviour of sand during cyclic loading is strongly hysteretic and irreversibility occurs and causes permanent deformations.

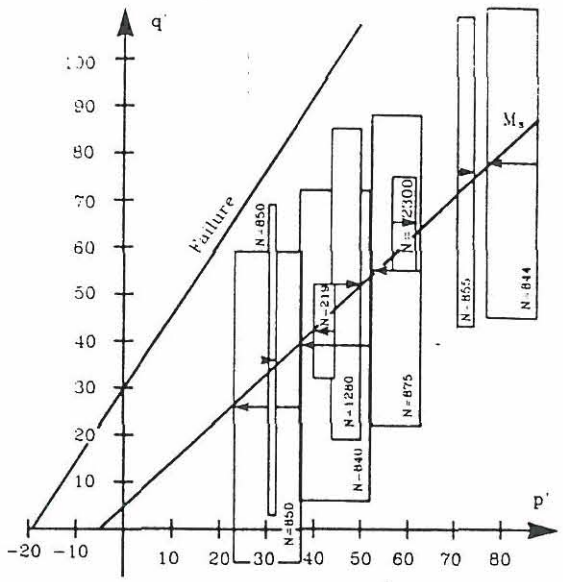

Figure 4. Verification of the stable static M_s.

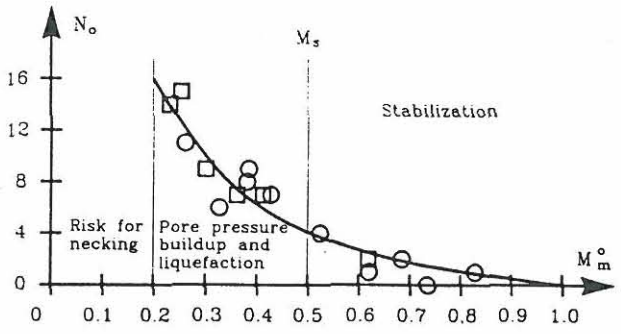

Figure 5. Estimation of N_o as a function of M_m° formula 8.

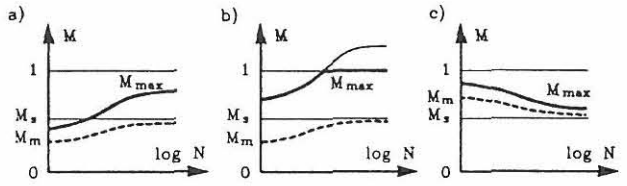

Figure 6. Development of the degree of mobilization under cyclic loading.

a) Increasing M_{max} resulting in pore pressure build-up.
b) Increasing M_{max} resulting in liquefaction.
c) Increasing M_{max} resulting in stabilization.

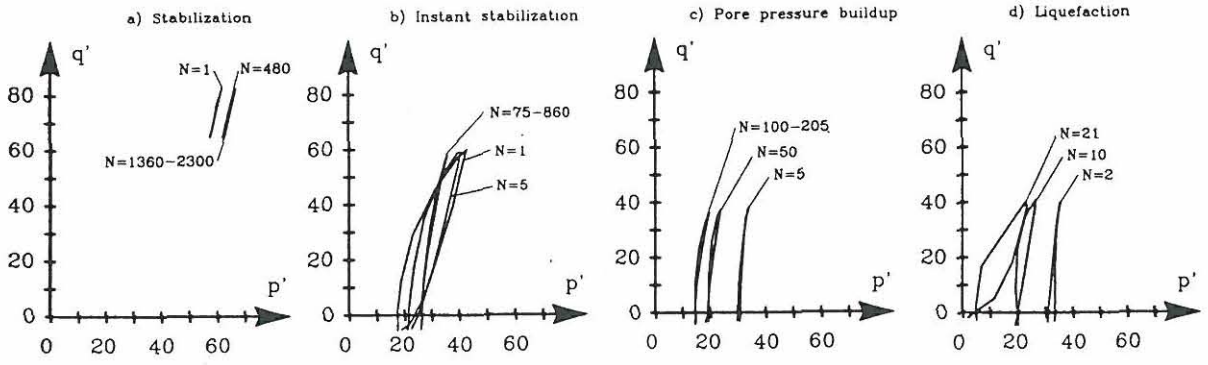

Figure 7. Stress path in cyclic loading.

The irreversibility depends on M_m° and does not occur for $M_m^\circ = M_n$. It depends on $(M_m^\circ - M_n), (M_s - M_m^\circ)$ and the number of cycles. In Figure 7 a) the irreversibility dominates the hysteresis, in Figure 7 d) only small irreversibility occurs.

Two stress cycles from the sequence in Figure 7 d) are shown in Figure 10. It shows that the behaviour of sand in this case is strongly hysteretic. The shape of the two curves are considerably different, corresponding to the different variations in p' and q', and it seems very complicated for a mathematical description.

However, by introducing the mobilization index M the curves become very regular and the mathematical formulation rather easy.

A performance curve for a first loading is shown in Figure 8 with $M_m^\circ \approx 0$. It can be described by

$$\frac{\partial M}{\partial \varepsilon_q} = G_M (1 - M^n)$$

where G_M is a normalized shear modulus, and n is a parameter which describes the curvature. In unloading the formula is modified to

$$\frac{\partial M}{\partial \varepsilon} = G_M (1 - |M|^n)$$

and a hysteric cyclic curve can then be described by:

$$\frac{\partial M}{\partial \varepsilon} = G_M \left(1 - sign\left(\frac{M}{d\varepsilon}\right) |M^n|\right) \qquad (9)$$

This shows continuity and differentiability for $M = 0$, (Figure 9). The formula is a simplified Bouc-Wen formula.

A further study shows that when $M_m \neq 0$ unrealistic irreversibilities occur except for small stress amplitudes. In order to separate the hysteretic behaviour from irreversibility, the formula is modified

$$\frac{\partial (M - M_m)}{\partial \varepsilon} = G_M \left(1 - sign\left(\frac{M - M_m}{d\varepsilon}\right) \left|\frac{M - M_m}{1 - M_m}\right|^n\right) \qquad (10)$$

In Figure 10 formula (10) is fitted to test results with small values of M_m by the method of least squares. Characteristic values of G_n and n are $G_M = 900$ and $n = 0.5$.

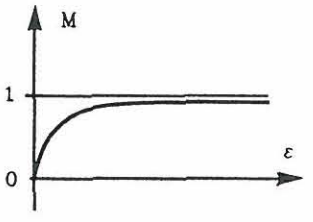

Figure 8. Normalized performance curve.

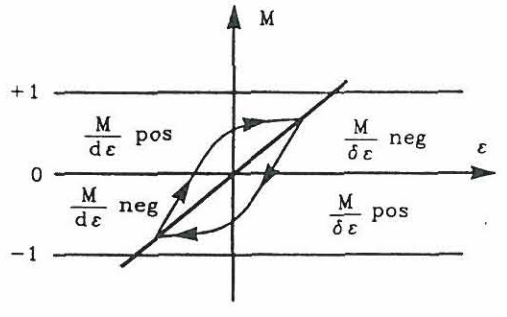

Figure 9. Hysteretic curve (eq 9).

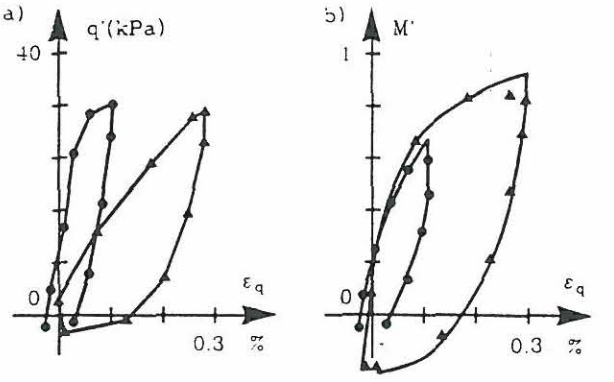

Figure 10. Hysteretic curves estimated from eq (10) and measured in triaxial tests.

Using formula (6), (7), (8) and (10) the development of hysteresis during cyclic loading can be followed and the damping ratio D calculated. For small values of M_m the damping ratio depends on M_{max} only:

$$D \approx 0.5\, M \qquad (11)$$

Hardin and Drnevich propose for a clean dense sand $D = 0.28 - 0.015\ log(N)$, which is seen to correspond to a natural state with stabilisation.

CONCLUSION

The behaviour of sand subjected to cyclic loading is described in simple mathematical formulations by introducing a normalized deviator stress, called the mobilization index. This paper shows how stabilization, instant stabilization, pore pressure buildup, and liquefaction develop and how hysteretic curves and damping ratios can be calculated. The damping ratio agrees well with expected values for a saturated sand.

REFERENCES

Casagrande, A. : *Liquefaction and cyclic deformations of sand. A critical review.* Harvard Soil Mechanics series 88. Harvard University, Cambridge. Mass. 1976.

Castro, G. : *Liquefaction and cyclic mobility of saturated sand.* J. Geo. Eng. Div., ASCE, Vol. 101, pp 551-569, 1975.

Castro, G. and Poulos, S.J. : *Factors affecting liquefaction and cyclic mobility.* Proc. ASCE, Vol. 103, GT6, 1977.

Hardin, B.O. and Drnevich, V.P. (1972) : *Shear modolus and damping in soils: Design equations and curves.* J. of SMFD, ASCE 98 (SM7) pp 667-692, 1972.

Jacobsen, H.M. and Ibsen, L.B. : *Development of pore pressure in cohesionless soil with initial shear stresses during cyclic loading.* YGEC III, Minsk, 1989.

Loung, M. : *Stress-strain aspects of cohesionless soil under cyclic and transient loading.* Int. Symp. on Soils under Cyclic and Transient Loading. Swansea, Jan. 1980.

Nielsen, S.R.K., Thoft-Christensen, P., Jacobsen, H.M. : *Reliability of soil sublayers under earthquake excitation: Markov Approach.* IV Int. Conf. on Soil Dynamics and Earthquake Engineering. Mexico, 1989.

Seed, H.B., Lee, K.L. : *Liquefaction of saturated sands during cyclic loading.* J. SMFD, ASCE, Vol. 92, No. SM6, Nov. 1966, pp 105-134.

Seed, H.B. : *Soil liquefaction and cyclic mobility evaluation for level ground during earthquake.* Proc. ASCE, No. GT2, Feb. 1979, pp 200-255.

Linear and Quadratic Lanczos Algorithms

Steffen Vissing & Steen Krenk
Department of Building Technology and Structural Engineering
Aalborg University, DK–9000 Aalborg, Denmark

Eigenvalue problems arise in various engineering problems as for instance structural dynamics and stability analysis as well as in heat tranfer analysis. The solution of linear or quadratic eigenvalue problems is therefore an essentiel part of the analysis. Quadratic eigenvalue problems are often solved after reduction to an indefinite linear eigenvalue problem of double size and thus the fundamental problem is the generalized indefinite linear eigenvalue problem. In this paper Lanczos algorithms for the symmetric problem is developed, but the algorithms may be generalized to nonsymmetric problems by introducing biorthogonal sets of left and right vectors. The generalized linear eigenvalue problem is of the form

$$(\mathbf{A} + \lambda \mathbf{B})\mathbf{w} = \mathbf{0} \tag{1}$$

where $\mathbf{A}$ and $\mathbf{B}$ are $n \times n$ real symmetric matrices which may be indefinite, λ is an eigenvalue and $\mathbf{w}$ is the corresponding n-dimensional eigenvector.

A general strategy for the generalized linear indefinite eigenvalue problem (1) consists of setting up a Krylov sequence representing the required eigenvectors and defining a proper orthogonality condition and vector orientation. A Krylov subspace suitable for approximate representation of the eigenvectors corresponding to the numerically smallest or largest eigenvalues can be generated by iterating with the matrix $\mathbf{A}^{-1}\mathbf{B}$ or the matrix $\mathbf{B}^{-1}\mathbf{A}$. The eigenvalue problem may typically arise from a finite element formulation in which the discretization causes the largest errors for the numerically largest eigenvalues. Further more only a small fraction of the eigenvectors corresponding to the numerically smallest eigenvalues may approximate a response to sufficient accuracy. Therefore the following Krylov sequence is used

$$[\mathbf{w}_0,\ \mathbf{A}^{-1}\mathbf{B}\mathbf{w}_0,\ (\mathbf{A}^{-1}\mathbf{B})^2\mathbf{w}_0, \ldots,\ (\mathbf{A}^{-1}\mathbf{B})^{m-1}\mathbf{w}_0] \tag{2}$$

However, an efficient use of the Krylov sequence requires some kind of condition on the base vectors, e.g. a suitable orthogonality condition. Natural choices for orthogonalizing the Krylov vectors are either of the two system matrices $\mathbf{A}$ and $\mathbf{B}$ or a simple matrix like the identity matrix. This paper presents algorithms in which the vectors are orthogonalized with respect to either of the system matrices. Hereby the vectors need in principle only be orthogonalized to the previous two vectors in order to achieve orthogonality and only two parameters in the recurrence formulae are needed. However, in finite precision the numerical error increase in each iteration whereby non-orthogonal vectors may be generated. In order to prevent the loss of orthogonality a simple reorthogonalisation procedure is applied. Using either $\mathbf{A}$ or $\mathbf{B}$ orthogonality conditions the n-dimensional eigenvalue

problem is reduced to an m-dimensional eigenvalue problem with a symmetric tridiagonal matrix $\mathbf{T}$ and, on account of indefinite system matrices, a diagonal matrix $\mathbf{E}$ containing ± 1 in the diagonal. Alternative, orthogonality conditions with respect to a matrix without direct relation to the problem e.g. the identity matrix may lead to fewer matrix operations but the tridiagonal matrix $\mathbf{T}$ is then replaced by an upper Hessenberg matrix.

Linear Lanczos algorithms for the generalized symmetric but indefinite eigenvalue problem with $\mathbf{A}$ and $\mathbf{B}$ orthogonality conditions are given in pseudo code as Algorithm 1 and Algorithm 2. In the algorithms α_j, $j = 1, 2, \cdots, n$ are the diagonal elements of $\mathbf{T}$, β_j, $j = 2, 3, \cdots, n$ are the sub- and superdiagonal elements of $\mathbf{T}$ and e_j, $j = 1, 2, \cdots, n$ are the diagonal elements of $\mathbf{E}$. The efficiency of the algorithms depends on the two matrix operations $\mathbf{B}\mathbf{q}_j$ and $\mathbf{A}^{-1}\mathbf{p}_j$ which is directly related to the bandwidth of the system matrices $\mathbf{A}$ and $\mathbf{B}$.

ALGORITHM 1: LINEAR LANCZOS WITH $\mathbf{A}$ ORTHOGONALITY

Start vector $\mathbf{p}_1$
Initialize $\mathbf{p}_0 := \mathbf{0}$
for $(j := 1$ to $m)$
  $\mathbf{q}_j := \mathbf{A}^{-1}\mathbf{p}_j$
  $d := \mathbf{q}_j^T \mathbf{p}_j$
  $e_j := \text{sign}(d)$
  $\beta_j := |d|^{1/2}$
  $\mathbf{q}_j := \mathbf{q}_j / \beta_j$
  $\mathbf{p}_j := \mathbf{p}_j / \beta_j$
  $\mathbf{p}_{j+1} := \mathbf{B}\mathbf{q}_j$
  $\alpha_j := \mathbf{q}_j^T \mathbf{p}_{j+1}$
  $\mathbf{p}_{j+1} := e_j \mathbf{p}_{j+1} - \alpha_j \mathbf{p}_j - \beta_j \mathbf{p}_{j-1}$
  $\mathbf{p}_{j+1} := \text{ortho}(\mathbf{p}_k, \mathbf{q}_k),\ k = 1, 2, \cdots$

ALGORITHM 2: LINEAR LANCZOS WITH $\mathbf{B}$ ORTHOGONALITY

Start vector $\mathbf{q}_1$
Initialize $\mathbf{q}_0 := \mathbf{0}$
for $(j := 1$ to $m)$
  $\mathbf{p}_j := \mathbf{B}\mathbf{q}_j$
  $d := \mathbf{q}_j^T \mathbf{p}_j$
  $e_j := \text{sign}(d)$
  $\beta_j := |d|^{1/2}$
  $\mathbf{q}_j := \mathbf{q}_j / \beta_j$
  $\mathbf{p}_j := \mathbf{p}_j / \beta_j$
  $\mathbf{q}_{j+1} := \mathbf{A}^{-1}\mathbf{p}_j$
  $\alpha_j := \mathbf{q}_{j+1}^T \mathbf{p}_j$
  $\mathbf{q}_{j+1} := e_j \mathbf{q}_{j+1} - \alpha_j \mathbf{q}_j - \beta_j \mathbf{q}_{j-1}$
  $\mathbf{q}_{j+1} := \text{ortho}(\mathbf{q}_k, \mathbf{p}_k),\ k = 1, 2, \cdots$

A full reorthogonalization procedure is shown in Algorithm 1 and 2 in which all the $\mathbf{p}_j$ vectors are stored. A more efficient reorthogonalization algorithm may be applied.

After the generalized Lanczos reduction a reduced m-dimensional eigenvalue problem is obtained in the form

$$(\mathbf{E} + \lambda \mathbf{T})\mathbf{y} = \mathbf{0} \tag{3}$$

where $\mathbf{y}$ is an m-dimensional eigenvector corresponding to the eigenvalue λ. The eigenvalues of (3) approximate the numerically smallest eigenvalues of (1) while the corresponding eigenvectors are obtained by $\mathbf{w} = \mathbf{Q}\mathbf{E}\mathbf{y}$ where $\mathbf{Q} = [\mathbf{q}_1, \mathbf{q}_2, \cdots, \mathbf{q}_m]$ is a matrix storing the orthogonalized Krylov vectors known as Lanczos vectors. The eigenvalues of (3) may be

obtained by a generalization of a symmetric solver for the standard eigenvalue problem with a symmetric tridiagonal matrix e.g. the QR method or by an unsymmetric solver for the standard eigenvalue problem with the unsymmetric tridiagonal matrix **ET**. The unsymmetric solver will fill out the upper part of the matrix **T**. Additional work is needed on the stability of the symmetric solver.

Example

The test example shown in Figure 1 is a 10 stores building with a vertical viscous damper at the top. The physical properties are given in the figure. The building is modelled with 174 elements and has 150 free degrees of freedom. The damping matrix only contains one nonzero element corresponding to the damping coefficient c of the damper.

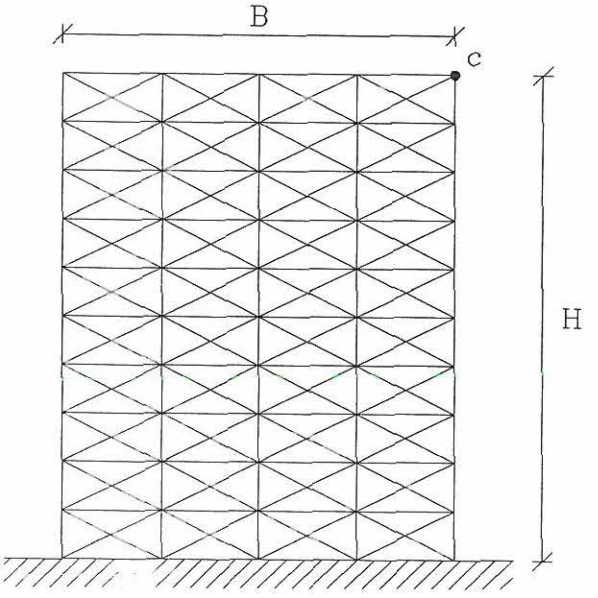

A	I	B	H	ρ	E
1	1/12	20	25	0.1	1

Figure 1: 10 stores building with a damper

In table 1 and 2 the eigenvalues for 10, 20 and 40 iterations with the algorithms for **A** and **B** orthogonality conditions are compared with the 20 smallest eigenvalues of the exact solution with $c = 0.5$. The eigenvalues for $c = 0$, $c = 0.5$, $c = 0.1$ are shown in Figure 2.

This example show no notable difference in the convergence rate for **A** and **B** orthogonality. Approximately half of the eigenvalues have converged.

Exact	10 iterations	20 iterations	40 iterations
$0.0014 \pm 0.0383i$	0.0014 ± 0.0383	$0.0014 \pm 0.0383i$	$0.0014 \pm 0.0383i$
$0.0049 \pm 0.0844i$	0.0049 ± 0.0844	$0.0049 \pm 0.0844i$	$0.0049 \pm 0.0844i$
$0.0108 \pm 0.1159i$	0.0108 ± 0.1160	$0.0108 \pm 0.1159i$	$0.0108 \pm 0.1159i$
$0.0040 \pm 0.2159i$	-0.1525	$0.0040 \pm 0.2159i$	$0.0040 \pm 0.2159i$
$0.0003 \pm 0.2311i$	0.0087 ± 0.2542	$0.0003 \pm 0.2312i$	$0.0003 \pm 0.2311i$
$0.0010 \pm 0.2610i$	0.9020	$-0.0059 \pm 0.2656i$	$0.0010 \pm 0.2610i$
$0.0277 \pm 0.2909i$	–	$0.0005 \pm 0.3364i$	$0.0277 \pm 0.2909i$
$0.0008 \pm 0.3249i$	–	$0.0084 \pm 0.4547i$	$0.0008 \pm 0.3249i$
$0.0022 \pm 0.3457i$	–	$0.0370 \pm 0.7749i$	$0.0022 \pm 0.3457i$
$0.0047 \pm 0.3644i$	–	$0.2590 \pm 1.9052i$	$0.0047 \pm 0.3646i$

Table 1: Eigenvalues of a 10 stores building, **A** orthogonality, $c = 0.5$.

Exact	10 iterations	20 iterations	40 iterations
$0.0014 \pm 0.0383i$	0.0014 ± 0.0383	$0.0014 \pm 0.0383i$	$0.0014 \pm 0.0383i$
$0.0049 \pm 0.0844i$	0.0049 ± 0.0844	$0.0049 \pm 0.0844i$	$0.0049 \pm 0.0844i$
$0.0108 \pm 0.1159i$	0.0108 ± 0.1159	$0.0108 \pm 0.1159i$	$0.0108 \pm 0.1159i$
$0.0040 \pm 0.2159i$	0.0102 ± 0.2398	$0.0040 \pm 0.2159i$	$0.0040 \pm 0.2159i$
$0.0003 \pm 0.2311i$	0.3499 ± 0.3230	$0.0003 \pm 0.2311i$	$0.0003 \pm 0.2311i$
$0.0010 \pm 0.2610i$	–	$0.0001 \pm 0.2631i$	$0.0010 \pm 0.2610i$
$0.0277 \pm 0.2909i$	–	$0.0034 \pm 0.3300i$	$0.0277 \pm 0.2909i$
$0.0008 \pm 0.3249i$	–	$0.0134 \pm 0.4285i$	$0.0008 \pm 0.3249i$
$0.0022 \pm 0.3457i$	–	$0.0624 \pm 0.7202i$	$0.0022 \pm 0.3457i$
$0.0047 \pm 0.3644i$	–	$0.7684 \pm 2.0851i$	$0.0048 \pm 0.3645i$

Table 2: Eigenvalues of a 10 stores building, **B** orthogonality, $c = 0.5$.

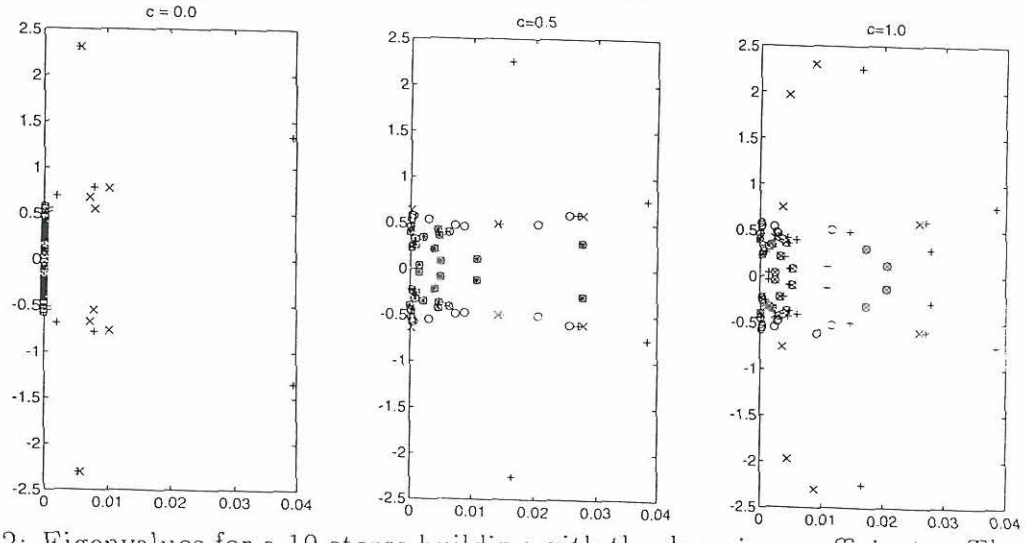

Figure 2: Eigenvalues for a 10 stores building with the damping coefficient c. The symbols o, + and × stands for, respectively, the exact solution, **A** orthogonality and **B** orthogonality.

PREDICTION OF GLOBAL AND LOCALIZED DAMAGE AND FUTURE RELIABILITY FOR RC STRUCTURES SUBJECT TO EARTHQUAKES

H.U. Köylüoğlu
Department of Civil Engineering and Operations Research, Princeton University, Princeton, NJ 08544, USA

S.R.K. Nielsen
Department of Building Technology and Structural Engineering, Aalborg University, Sohngaardsholmsvej 57, DK-9000 Aalborg, Denmark

A.Ş. Çakmak
Department of Civil Engineering and Operations Research, Princeton University, Princeton, NJ 08544, USA

P.H. Kirkegaard
Department of Building Technology and Structural Engineering, Aalborg University, Sohngaardsholmsvej 57, DK-9000 Aalborg, Denmark

SUMMARY

The paper deals with the prediction of global and localized damage and the future reliability estimation of partly damaged reinforced concrete (RC) structures under seismic excitation. Initially, a global maximum softening damage indicator is considered based on the variation of the eigenfrequency of the first mode due to the stiffness and strength deterioration of the structure. The hysteresis of the first mode is modelled by a Clough and Johnston hysteretic oscillator [1] with a degrading elastic fraction of the restoring force. The linear parameters of the model are assumed to be known, measured before the arrival of the first earthquake from non-destructive vibration tests or via structural analysis. The previous excitation and displacement response time series is employed for the identification of the instantaneous softening using an ARMA model. The hysteresis parameters are updated after each earthquake. The proposed model is next generalized for the MDOF system. Using the adapted models for the structure and the global damage state, the global damage in a future earthquake can then be estimated when a suitable earthquake model is applied. The performance of the model is illustrated on RC frames which were tested by Sözen and his associates [2,4].

1. INTRODUCTION

The physical local damage in reinforced concrete (RC) structures subject to severe seismic excitation is attributed to micro-cracking and crushing of concrete, yielding of the reinforcement bars and bond deterioration at the steel-concrete interfaces. To the extent

that RC structures can be modelled by non-linear mechanical theories, local damage at a cross-section of the structure can adequately be measured by the degradation of bending stiffness and moment capacity of the cross-section. The overall effect of local damages is the stiffness and strength deterioration of the structure. A global damage indicator can then be defined as a functional of such continuously distributed local damages which characterize the overall damage state and serviceability of the structure.

Global damage indicators are response quantities characterizing the damage state of the structure after an earthquake excitation, and such can be used in decision-making during the design phase, or in case of post-earthquake reliability and repair problems. In serving these purposes, the global damage indicator should, at least, be observable for practical purposes, be a non-decreasing function of time unless the structures are repaired or strengthened, possess a failure surface (serviceability or ultimate limit state) to separate safe states from the unsafe ones and carry Markov property so that post-earthquake reliability estimates for a partly damaged structure can be made solely from the latest recorded value of the damage indicator.

The maximum softening damage indicators measure the maximum relative reduction of the vibrational frequencies for an equivalent linear system with slowly varying stiffness properties during a seismic event, hence, display the combined damaging effects of the maximum displacement ductility of the structure during extreme plastic deformations and the stiffness deterioration in the elastic regime, the latter effect being referred to as final softening. The introduction of the one-dimensional maximum softening indicator based on an equivalent linear single-degree-of-freedom (SDOF) system fits to the first mode of the RC building as a global damage indicator is due to DiPasquale and Çakmak [3]. The excitation and displacement response time series of a single position on the building are the only required observations for the one-dimensional maximum softening damage indicator. The applicability of the index was analysed based on data from shake table experiments with RC frames performed by Sözen and his associates [2,4]. Limit states for slight damage to total collapse were calibrated using this data and the performance of the index was tested for partly damaged structures which had been instrumented in the past. The maximum softening concept has also been generalized to multi-degree-of-freedom (MDOF) models along with the associated damage localization problem [9]. The Markov property of the maximum damage indicator chains for SDOF and 2 DOF models was tested numerically by means of Monte Carlo simulations [8,9] and it was concluded that the global damage indicator fulfils Markov property with sufficient accuracy.

The present paper deals with the prediction of global and localized damage and the future reliability estimation of partly damaged reinforced concrete (RC) structures under seismic excitation. Initially, a global maximum softening damage indicator is considered based on the variation of the eigenfrequency of the first mode due to the stiffness and strength deterioration of the structure. The hysteresis of the first mode is modelled by a Clough and Johnston hysteretic oscillator [1], with degrading elastic fraction of the restoring force, subject to seismic excitation. The circular eigenfrequency, damping ratio and the modal participation factor of the first mode of the undamaged structure are assumed to be known, measured before the arrival of the first earthquake from

non-destructive vibration tests or via structural analysis. The previous excitation and displacement response time series is employed for the identification of the instantaneous softening using an ARMA model. The two free hysteresis parameters are updated after each earthquake from another system identification procedure where a weighted error criterion defined using instantaneous softening and the displacement response time series are employed. Using the adapted models for the structure and the global damage state, the global damage in a future earthquake can then be estimated if a suitable earthquake model is applied. In the paper, the Markov property of the global maximum softening damage indicator is verified. Hence, the maximum softening index as calculated from the present method may be used for future reliability estimates as well.

The proposed model is next generalized for an MDOF system. The horizontal displacement of the structure is assumed to be measured in a finite n number of points on the structure. An equivalent hysteretic shear model of n degrees of freedom is introduced in which the linear system parameters are identified to provide the same undamped circular eigenfrequencies, modal damping ratios and modal participation factors as measured on the undamaged structure. The shear force between the measure points (typically storeys) is next modelled by Clough-Johnston hysteretic models similar to the one applied in the SDOF case. The set of maximum softening damage indices between all measure points forms a Markov vector and can be used for reliability estimation. Since the local damages are directly observed, the localization of the damage problem (the inverse problem) is circumvented.

The performance of the model is illustrated on RC frames which were tested by Sözen and his associates [2,4].

2. HYSTERETIC MODEL FOR SDOF OSCILLATOR

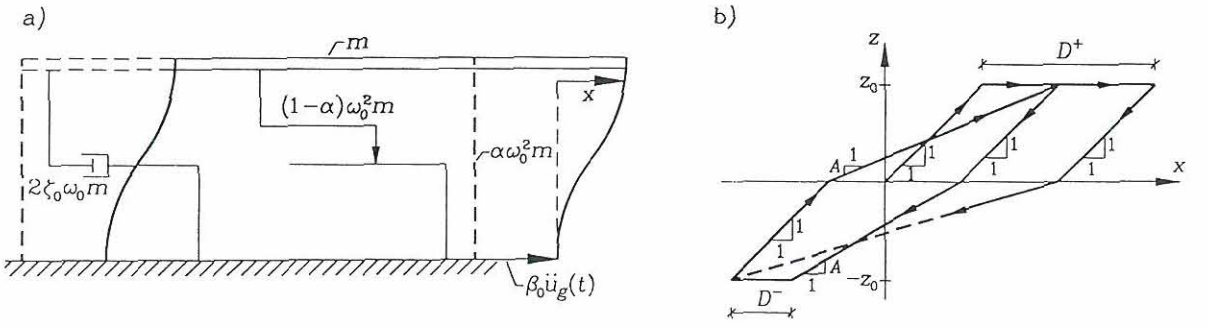

Figure 1. a) SDOF hysteretic oscillator model b) Clough-Johnston hysteretic model.

The equations of motion of the first mode are modelled by the following coupled differential equations

$$\ddot{x}(t) + 2\zeta_0\omega_0\dot{x}(t) + \omega_0^2\Big[\alpha(D(t))x(t) + \big(1-\alpha(D(t))\big)z(t)\Big] =$$

$$-\beta_0\ddot{u}_g(t) \quad , \quad t > t_0 \quad , \quad x(t_0) = \dot{x}(t_0) = 0 \tag{1}$$

$$\dot{z}(t) = k\big(\dot{x}(t), z(t), D(t); z_0\big)\dot{x}(t) \quad , \qquad z(t_0) = 0 \tag{2}$$

$$\dot{D}(t) = g\big(\dot{x}(t), z(t); z_0\big)\dot{x}(t) \quad , \qquad D(t_0) = D_0 \tag{3}$$

$$\alpha(D(t)) = \Big(\frac{2z_0}{2z_0 + D(t)}\Big)^{n_0} \tag{4}$$

$$k\big(\dot{x}(t), z(t), D(t); z_0\big) = H(z)\big\{A(t)H(\dot{x})(1 - H(z - z_0))+$$

$$H(-\dot{x})\big\} + H(-z)\big\{A(t)H(-\dot{x})(1 - H(-z - z_0)) + H(\dot{x})\big\} \tag{5}$$

$$g\big(\dot{x}(t), z(t); z_0\big) = H(\dot{x})H(z - z_0) - H(-\dot{x})H(-z - z_0) \tag{6}$$

$$A(t) = \frac{z_0}{z_0 + D(t)} \tag{7}$$

$$H(x) = \begin{cases} 1 \quad , & x \geq 0 \\ 0 \quad , & x < 0 \end{cases} \tag{8}$$

The first modal coordinate $x(t)$ can be defined as the top storey displacement of the structure relative to the ground surface if the mode shape is suitably normalized. The linear circular eigenfrequency, ω_0, the damping ratio, ζ_0, and the mode participation factor, β_0, of the first mode are assumed to be known before the arrival of the first earthquake, obtained previously via linear structural analysis or non-destructive experimentation of the structure. $\ddot{u}_g(t)$ indicates the horizontal earth surface acceleration signal and the first earthquake starts at the time $t = t_0$. $\alpha\big(D(t)\big)$ is the elastic fraction of the restoring force.

$z(t)$ is the hysteretic component which is modelled using the Clough-Johnston hysteretic model. $z = +z_0$, $z = -z_0$ signify the yield levels. $k\big(\dot{x}(t), z(t), D(t); z_0\big)$ is a non-analytic function describing the state dependent stiffness of the hysteretic model on the component $z(t)$. The stiffness degrading hysteretic constitutive law of the model can be represented as shown in figure 1.b. The Clough-Johnston model deals with the stiffness degradation by changing the slope $A(t)$ of the elastic branches as the accumulated plastic deformations, $D^+(t)$ and $D^-(t)$ at positive and negative yielding, increase as shown in figure 1.b. $D(t) = D^+(t) + D^-(t)$ is the total accumulated plastic deformations. For loading branches, the slope $A(t)$ is selected such that the elastic branch always

aims at the previous unloading point with the other sign. At unloadings, the slope is 1. D_0 is the initial value of the total accumulated damage which is zero before the first earthquake hits and is assumed to be determined from previous earthquake and displacement response records for the succeeding earthquakes. $H(x)$ is the unit step function.

A novelty of the present model stems primarily from the modelling of $\alpha\big(D(t)\big)$ as a non-increasing function of the damage parameter $D(t)$. Since, $\alpha\big(D(t)\big)$ measures the fraction of the restoring force from linear elastic behaviour, this fraction must decrease as larger and larger parts of the structure become plastic. Note that initially, $\alpha\big(D(0)\big) = 1$, and, unless there is damage, still $\alpha(0) = 1$. The dependence of $\alpha\big(D(t)\big)$ on $D(t)$ as indicated by (4) has been selected to fulfil this boundary condition. The relative success of the model (1)-(8) in reproducing actually recorded displacement time series in the studied example is primarily due to this modelling.

The hysteretic parameters z_0, n_0 are to be identified from the experienced excitation and displacement response time series with an optimal system identification method. The Clough-Johnston hysteretic model was originally designed for reinforced concrete beams. The differential description of the model, applied herein, is due to Minai and Suzuki [6].

3. HYSTERETIC MODEL FOR MDOF SYSTEM

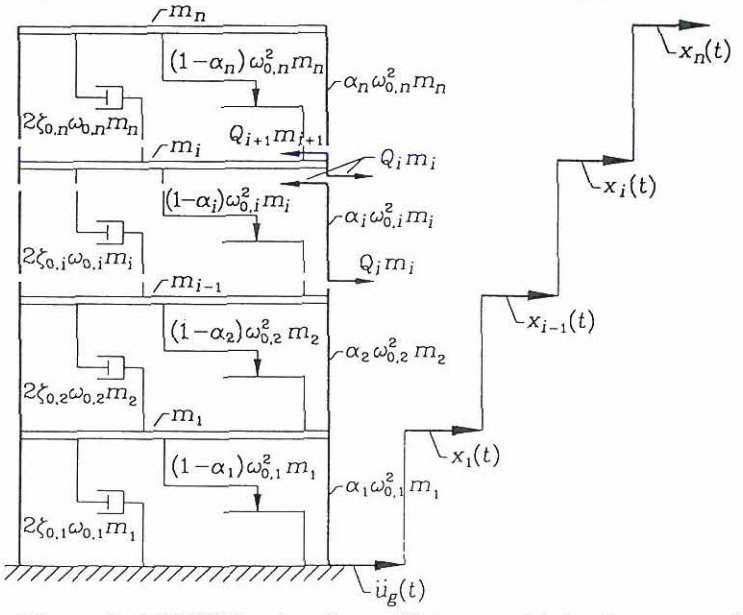

Figure 2. MDOF hysteretic oscillator model for the measuring points.

The horizontal displacement of the structure at a finite number of points is measured. The relative displacement between the ith and $(i+1)$th measure points is designated x_i, and x_1 signifies the displacement of the first measure point relative to the ground surface excited by the horizontal acceleration, $\ddot{u}_g$, see figure 2. For simplicity, the time dependence of $x, \ddot{u}_g$ etc. is not explicitly shown in the following notation used for

the MDOF system. With reference to the shear model shown in figure 2, the relative displacement x_i between the ith and $(i+1)$th measure point is assumed to cause a shear force of magnitude $Q_i m_i$ where m_i is the storey mass. The equations of motion in terms of the relative displacements can be written as,

$$\left.\begin{array}{lll} \ddot{x}_1 = \mu_2 Q_2 - Q_1 - \ddot{u}_g & , \; t > t_0 & \\ \ddot{x}_i = \mu_{i+1} Q_{i+1} - (\mu_i + 1) Q_i + Q_{i-1} & , \; t > t_0 \quad , \quad i = 2, 3, \cdots, n-1 & \\ \ddot{x}_n = -(\mu_n + 1) Q_n + Q_{n-1} & , \; t > t_0 & \\ x_i(t_0) = \dot{x}_i(t_0) = 0 & , \quad i = 1, 2, \cdots, n & \end{array}\right\} \tag{9}$$

$$Q_i = 2\zeta_{0,i}\omega_{0,i}\dot{x}_i + \omega_{0,i}^2\big(\alpha_i x_i + (1-\alpha_i) z_i\big) \quad , \qquad i = 1, 2, \cdots, n \tag{10}$$

$$\dot{z}_i = k(\dot{x}_i, z_i, D_i; z_{0,i})\dot{x}_i \quad , t > t_0 \quad , z_i(t_0) = 0 \quad , \qquad i = 1, 2, \cdots, n \tag{11}$$

$$\dot{D}_i = g(\dot{x}_i, z_i; z_{0,i})\dot{x}_i \quad , t > t_0 \quad , D_i(t_0) = D_{i,0} \quad , \qquad i = 1, 2, \cdots, n \tag{12}$$

$$\alpha_i = \Big(\frac{2z_{0,i}}{2z_{0,i} + D_i}\Big)^{n_{0,i}} \quad , \qquad i = 1, 2, \cdots, n \tag{13}$$

$$\mu_i = \frac{m_i}{m_{i-1}} \quad , \qquad i = 2, 3, \cdots, n \tag{14}$$

In (9), nth measure point is assumed to be located at the top storey. $k(\dot{x}_i, z_i, D_i; z_{0,i})$ and $g(\dot{x}_i, z_i; z_{0,i})$ are given by (5) and (6). $2\zeta_{0,i}\omega_{0,i}m_i$ and $\omega_{0,i}^2 m_i$ are respectively the damping coefficients and initial elastic spring stiffnesses between the storeys. Hence, $\omega_{0,i}$ and $\zeta_{0,i}$ $i = 1, 2, \cdots n$ are merely parameters to specify the linear parts of the shear forces and should not be confused with the natural frequencies and damping ratios of the structure. These parameters along with μ_i $i = 2, 3, \cdots n$ must be identified so that the elastic model of (9) and (10) with $\alpha_i = 1$ provides the same undamped circular eigenfrequencies ω_i, damping ratios ζ_i and modal participation factors β_i of the undamaged structure, as calculated or measured by non-destructive testing. Notice that the indicated discrete linear system has $3n - 1$ free parameters, $\omega_{0,i}$, $\zeta_{0,i}$ and μ_i, to fit the $3n$ parameters, ω_i, ζ_i and β_i, obtained from the primary linear system identification of the structure. Here, it is assumed that only the lowest n modes of the primary linear structure have been identified. There is an indeterminateness in the secondary system identification. This means that conditions can only be met at the lowest $n - 1$ modes.

The hysteretic parameters $z_{0,i}$ and $n_{0,i}$ are sequentially updated during the damage process after each severe earthquake by system identification.

4. GLOBAL DAMAGE INDICATORS : MAXIMUM SOFTENING INDEX

Consider the SDOF model. The instantaneous softening, $\delta(t)$, of the structure is defined as, Çakmak et al. [1,2,3].

$$\delta(t) = 1 - \frac{T_0}{T(t)} \tag{15}$$

where T_0 is the first period of the linear structure and $T(t)$ is the first period of the equivalent linear structure with slowly varying stiffness characteristics during an earthquake excitation. T_0 is assumed to be known from previous structural analysis or non-destructive experimentation of the structure and $T(t)$ is estimated from the excitation and displacment response time series of the experienced earthquake.

The maximum softening damage indicator, δ_M is the maximum of $\delta(t)$ during the seismic excitation.

$$\delta_M = \max\ \delta(t) \tag{16}$$

In the hysteretic model, the instantaneous slope of the hysteretic curve defines the varying instantaneous period of the equivalent linear structure. For Clough-Johnston model, the instantaneous slope is $A(t)$ for loading branches, 1 for unloading branches and 0 when yielding occurs. Therefore, instead of instantaneous softening, an average softening value is defined using the average slope, $\bar{m}$, of the hysteresis loop, the slope of the line through extreme points.

$$\bar{m} = \frac{2z_0}{2z_0 + D(t)} \tag{17}$$

The loop-averaged softening $S(t)$ is

$$S(t) = 1 - \sqrt{\frac{2z_0}{2z_0 + D(t)}\Big(1 - \alpha(D(t))\Big) + \alpha(D(t))} \tag{18}$$

where $\alpha(D(t))$ is given by (4). As seen from (18), $S(t)$ is non-decreasing during a seismic event and fully correlated to $D(t)$. $S(t)$ can then only measure the effect of the plastic deformations on the period of the structure since z_0 is considered to be non-degrading during a seismic event in this study.

Correspondingly, local softening can be defined for each measure point in the MDOF system.

$$S_i(t) = 1 - \sqrt{\frac{2z_{0,i}}{2z_{0,i} + D_i}(1 - \alpha_i) + \alpha_i} \quad , i = 1, 2, \cdots, n \tag{19}$$

where α_i is given by (13). $S_i(t)$ is a local damage indicator displaying the damaging effects of the local plastic deformations.

5. SYSTEM IDENTIFICATION

The proposed global damage indicator and the hysteretic model for the SDOF system are defined by six parameters, namely, $T(t)$, ζ_0 , ω_0 , β_0 , z_0 , n_0. $T(t)$ is estimated from the excitation and displacement response time series of the experienced earthquake using an ARMA model, e.g. [5], suited to the displacement response process and the estimated ARMA coefficients are mapped to determine the first period and the instantaneous softening, $S(t)^{ARMA}$, of the corresponding dynamic system. The next three parameters are assumed to be known before the arrival of the first earthquake, via linear structural analysis or previous non-destructive experimentation. The hysteresis parameters z_0 and n_0 are estimated from an iterative system identification procedure where a weighted error criterion for the jth iteration, $F^j(x(t), S(t); \hat{z}_0^j, \hat{n}_0^j)$, defined from the instantaneous softening and the displacement response time series is employed.

$$F^j(x(t), S(t); \hat{z}_0^j, \hat{n}_0^j) = w_1 \sum_k (\hat{x}_k^j - x_k)^2 + w_2 \sum_l (\hat{S}_l^j - S_l^{ARMA})^2 \tag{20}$$

where $x_k = x(t = t_k)$ etc. x_k are the measured displacements. $\hat{x}_k^j$ and $\hat{S}_l^j$ are model predictions using estimated hysteretic parameters, $\hat{z}_0^j$, $\hat{n}_0^j$. The summation over the index k is performed for the time interval where large oscillations occur, and, the summation over the index l is performed for the time interval where $S^{ARMA}(t)$ more or less stabilizes. This guarantees more weights given to large oscillations and large damage levels. Additionally, w_1 and w_2 are chosen such that the displacement and instantaneous softening contributions in the error are approximately equal, i.e.

$$\frac{w_1 \sum_k (\hat{x}_k^j - x_k)^2}{w_2 \sum_l (\hat{S}_l^j - S_l^{ARMA})^2} \simeq 1 \tag{21}$$

The new estimates for the hysteretic parameters are then obtained using the steepest descent method, e.g. [5].

$$z_0^{j+1} = z_0^j - \frac{\partial F^j}{\partial z_0} \epsilon_{z_0} \quad , \quad n_0^{j+1} = n_0^j - \frac{\partial F^j}{\partial n_0} \epsilon_{n_0} \tag{22}$$

the gradients $\frac{\partial F^j}{\partial z_0}$ and $\frac{\partial F^j}{\partial n_0}$ are computed numerically. ϵ_{z_0} and ϵ_{n_0} are step parameters calibrated from the numerical values of the gradients.

By these system identification procedures, $T(t)$ and hysteresis parameters z_0 and n_0 have been estimated using the observable measures; the excitation and displacement response time series only.

For MDOF systems, similar system identification methods can be introduced.

6. PREDICTION OF DAMAGE AND RELIABILITY

It will be assumed that the excitations from different earthquakes are mutually stochastically independent. Then, the memory of the previous earthquakes is carried over to the state vector $\mathbf{Z}^T(t) = [\mathbf{x}(t),\ \dot{\mathbf{x}}(t),\ \mathbf{z}(t),\ \mathbf{D}(t)]$ where $\mathbf{x}^T(t) = [x_1(t), \cdots, x_n(t)]$ etc. Since, it has been assumed above that the structural system returns to the equilibrium state after the previous earthquke corresponding to the initial values $\mathbf{x}(t_0) = \dot{\mathbf{x}}(t_0) = \mathbf{z}(t_0) = \mathbf{0}$, the memory of the previous earthquakes is then carried totally by the initial values $\mathbf{D}(t_0) = \mathbf{D}_0$. With these conditions on the initial values of the other state variables, the initial values of the damage vector $\mathbf{D}(t)$ in a sequence forms a Markov chain to the extent that the present mathematical model is an adequate representation of the RC-structure. Since the softening $S(t)$ and $\mathbf{S}(t)$ of the SDOF and MDOF systems only depend on the initial values D_0 and $\mathbf{D}_0$ of the damage process and the present earthquake $\ddot{u}_g(t)$, these quantities form a Markov chain. The consequences of these statements are that both the damage process and the reliability as measured using the maximum softening value in future earthquakes, can be predicted by the present model, if only the damage process, $D(t)$ and $\mathbf{D}(t)$ are updated after each seismic event, i.e. their terminal values in the previous earthquakes are calculated via updated hysteretic model parameters, z_0, n_0 and $\mathbf{z}_0$, $\mathbf{n}_0$.

The reliability of the structure subject to future earthquakes can be estimated using independent Monte Carlo simulations. This requires a suitable earthquake model for the generation of the mutually independent earthquake excitations. Running the hysteretic model subject to these excitations generates a sample set for the numerical values of maximum softening. These samples can further be used in evaluating the reliability of the structure based on the definition of failure event.

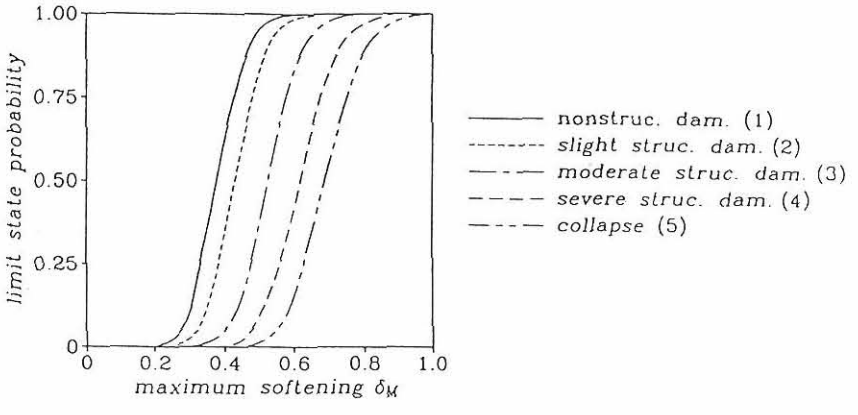

Fig.3: Distribution of observed limit state values of one-dimensional maximum softening [3].

In figure 3, the distribution function of observed values of the one-dimensional maximum softening, obtained from analysis of shake table experiments with reinforced concrete frames (Healey and Sozen (1978), Cecen (1979)), is shown. The limit state definition varied from insignificant damage to total collapse. In all cases a relatively small coefficient of variation was observed for the damage indicator. From this analysis it is

concluded that safe states of the structure can be separated from unsafe states with sufficient reliability, by determining whether or not the maximum softening δ_M exceeds a critical value δ_0. The failure event is then defined by $\{\delta_M \geq \delta_0\}$. For MDOF systems n-dimensional failure surfaces can be defined similarly [9].

7. EXAMPLE

In order to demonstrate the ability of the proposed hysteretic SDOF model to fit and predict actual seismic response of RC structures, experimentally recorded results on a 1:10 scaled planar 10 storey 3 bay reinforced concrete frame, shown in figure 4, tested at University of Illinois at Urbana Champaign [5], are used.

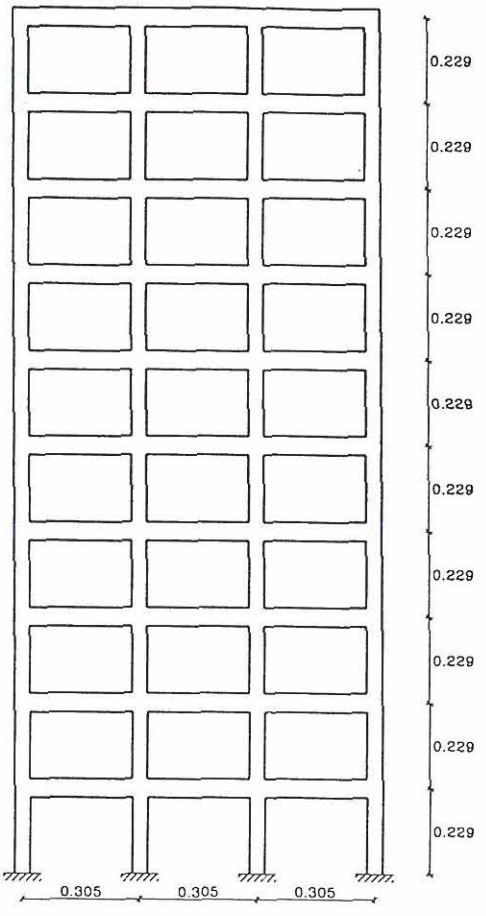

Figure 4. 10 storey 3 bay reinforced concrete frame.

The test structure consisted of two parallel frames working in parallel with ten uniformly distributed storey weights, attached in between. The beams and columns are symmetrically reinforced so that yield limits are the same in compression and tension, see [5] for more information about the geometrical and structural details of the structure.

a) H1-RUN1 ground acceleration

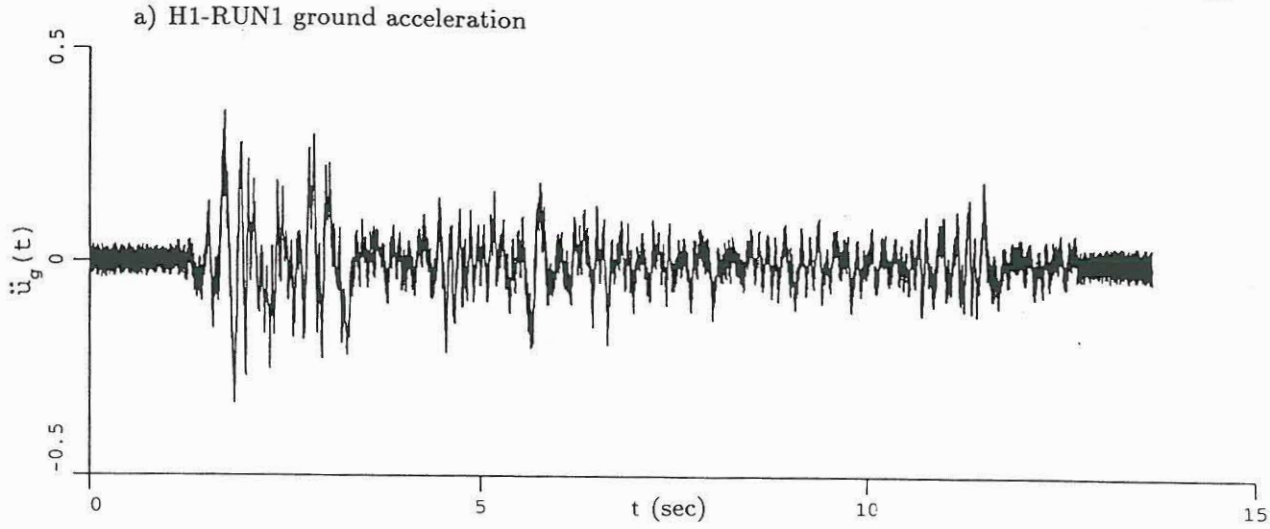

b) H1-RUN2 ground acceleration

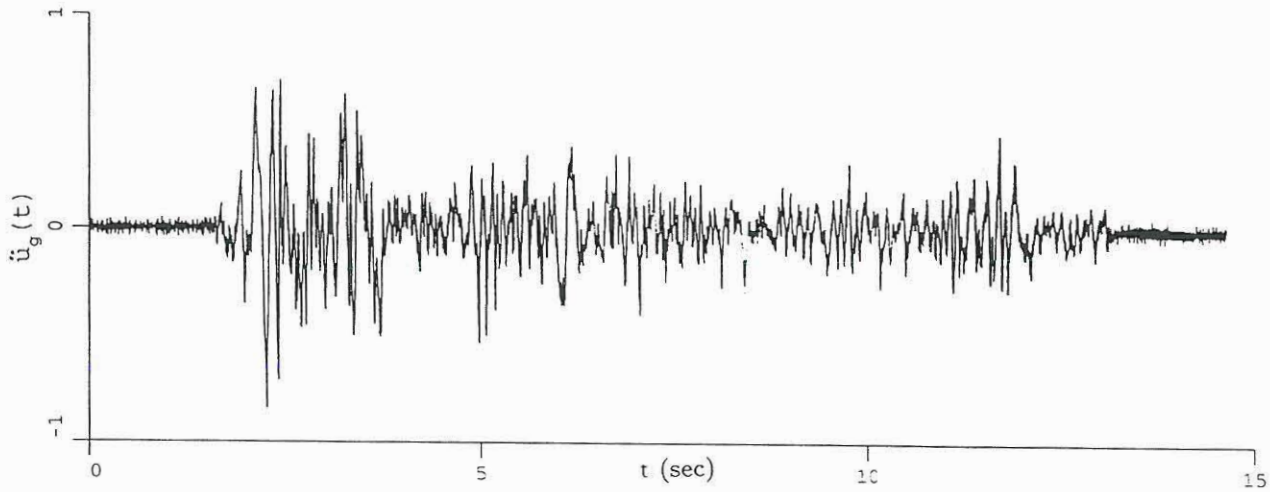

c) H1-RUN3 ground acceleration

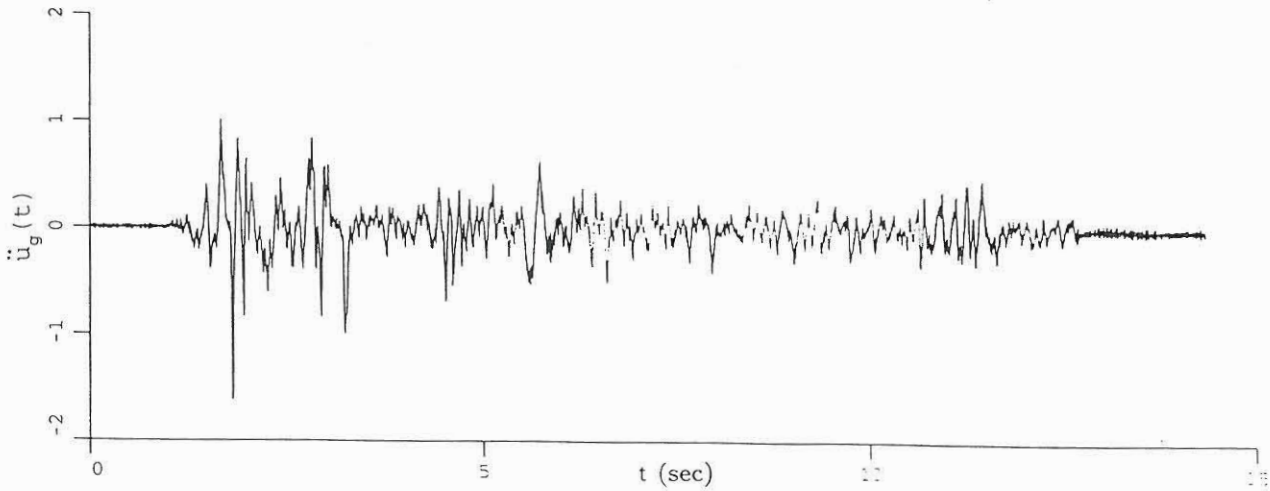

Figure 5. Ground accelerations normalized with respect to $g = 9810$ mm/sec^2 versus time, t, in seconds.

The eigenfrequency, damping ratio and modal participation factor for the first mode of the undamaged structure are $\omega_0 = 6\pi$, $\zeta_0 = 0.035$ and $\beta_0 = 1.32$. The first eigenvector is chosen such that displacement of the top storey is $1.32x(t)$ where $x(t)$ is the first modal coordinate.

This structure is excited by 3 consecutive horizontal acceleration processes at the ground surface which are simulated models of the El-Centro earthquake in 1940. These tests are called H1-RUN1, H1-RUN2 and H1-RUN3 in [5], so they are in this paper. The horizontal ground surface accelerations of these runs are given in figure 5 where $\ddot{u}_g(t)$ is normalized by the gravitational constant $g = 9810$ mm/sec^2.

$T(t)$ is estimated from the excitation and displacement response time series of the experienced earthquake using an ARMA model, e.g. [5], suited for the displacement response process. The time window size is chosen as 2.4 seconds and an ARMA model is fit for each 2.4 second time window. The estimate is located at the centre of the window and the estimates are smoothed. $S^{ARMA}(t)$ is then obtained using (15), see figure 8.

z_0 and n_0 are estimated using the predescribed steepest descent method. The identified numerical values for z_0 and n_0 using the correponding runs are listed in table 1.

RUN	z_0 (cm)	n_0
RUN1	2.68	0.83
RUN2	3.01	0.77
RUN3	3.14	0.73

Table 1. Estimated hysteretic parameters

The performance of the suited hysteretic models for each run using the values listed in table 1 is shown in figures 6 and 7 for the displacement of the top storey, $1.32x(t)$, and softening, $S(t)$, respectively. The prediction performance of the suited hysteretic model for RUN1 in the future earthquakes of tests RUN2 and RUN3 is shown in figures 8 and 9. Model predictions for $\hat{S}(t)$ are very good. The prediction performance of the suited hysteretic model for RUN2 in the future earthquake of test RUN3 is shown in figures 10 and 11. Comparison of figures 8 and 10, and 8 and 11 show that the updated model predicts better.

a) H1-RUN1 displacement of the top storey

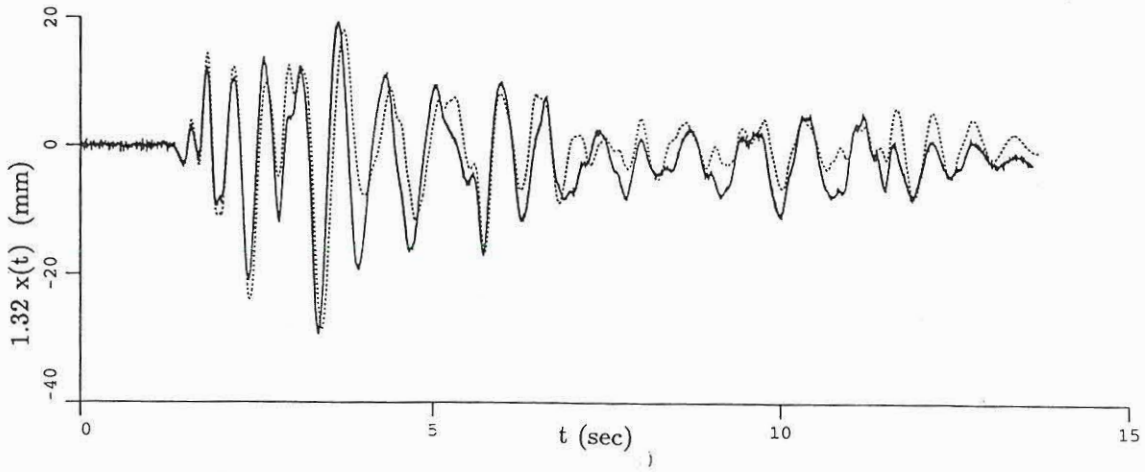

b) H1-RUN2 displacement of the top storey

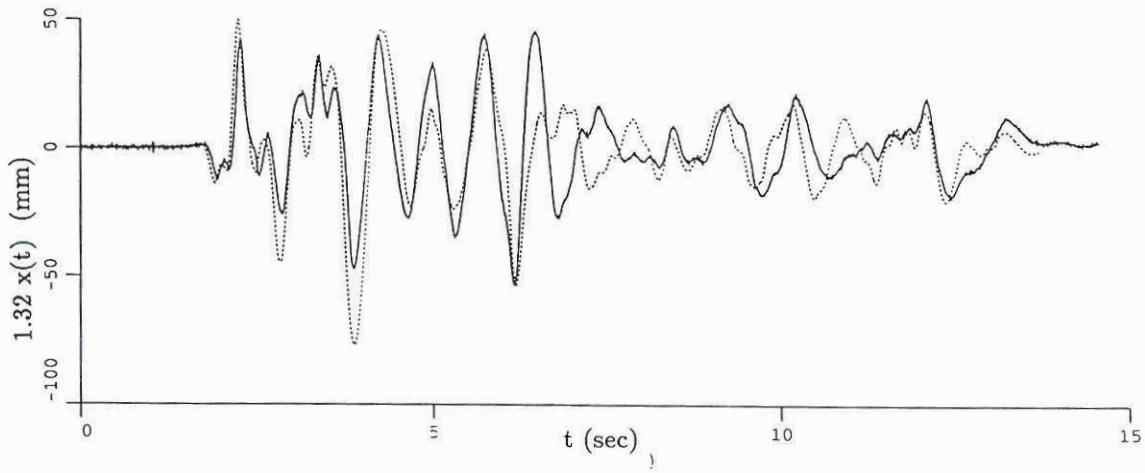

c) H1-RUN3 displacement of the top storey

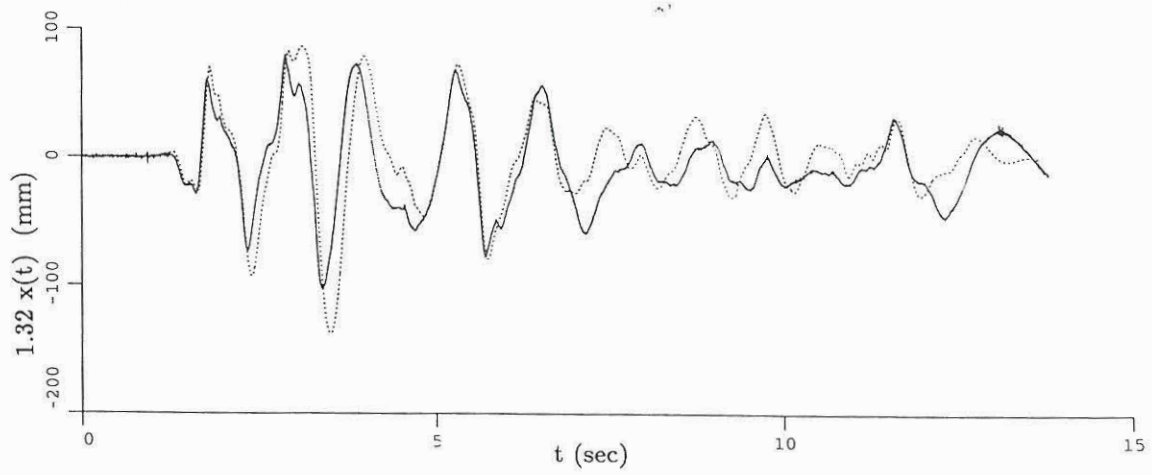

Figure 6. The performance of the suited hysteretic models for each RUN. Displacement of the top storey, $1.32x(t)$ and $1.32\hat{x}(t)$ in mm, versus time, t, in seconds.

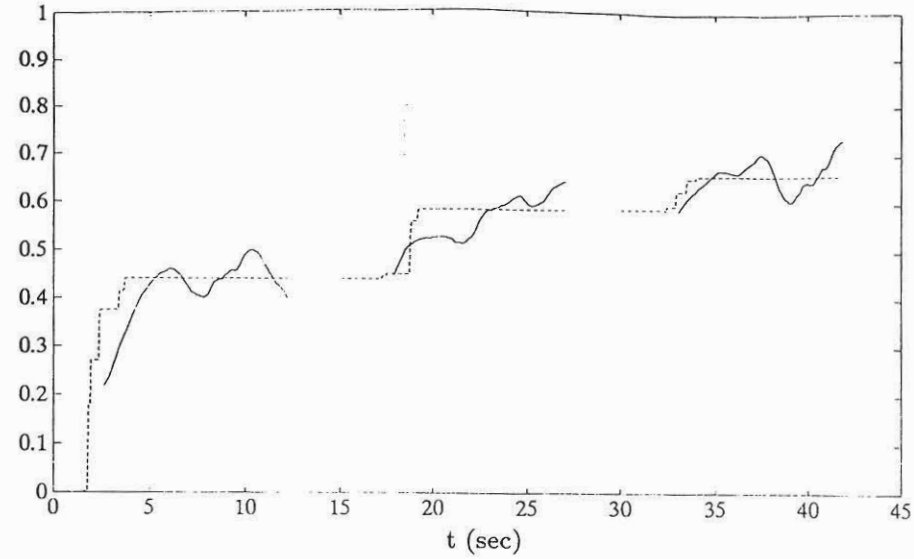

Figure 7. The performance of the suited hysteretic models for each RUN. Softening, $S^{ARMA}(t)$ and $\hat{S}(t)$, versus time, t, in seconds.

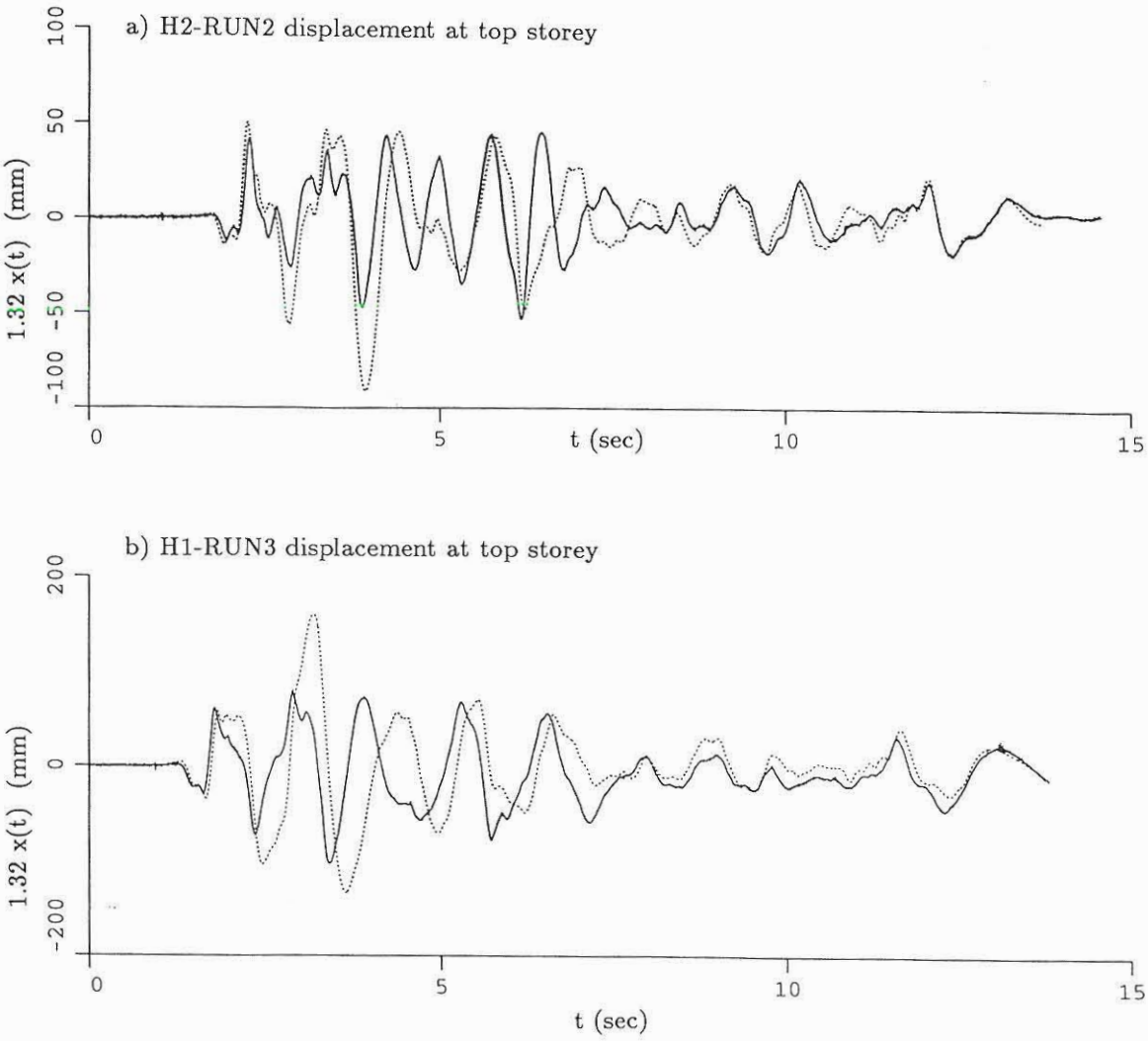

Figure 8. The prediction performance of the suited hysteretic model for RUN1 in RUN2 and RUN3 cases. Displacement of the top storey, $1.32x(t)$ and $1.32\hat{x}(t)$ in mm, versus time, t, in seconds.

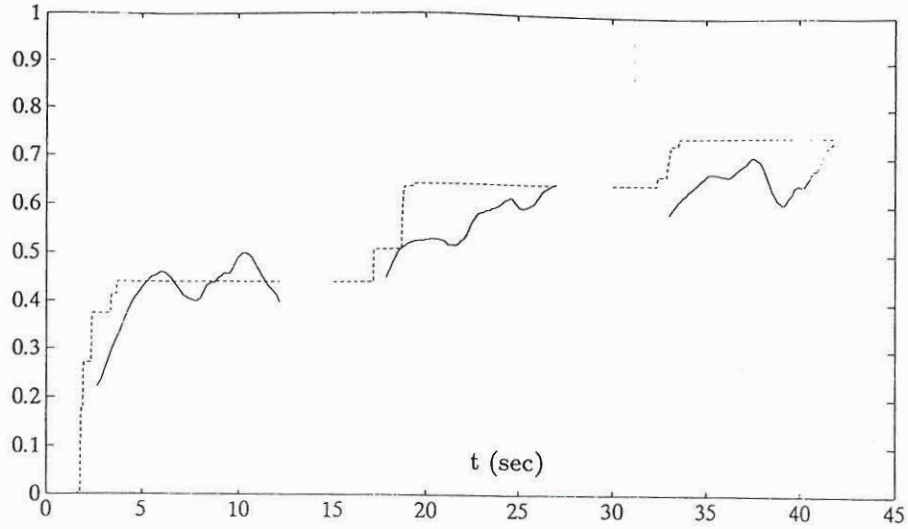

Figure 9. The prediction performance of the suited hysteretic model for RUN1 in RUN2 and RUN3 cases. Softening, $S^{ARMA}(t)$ and $\hat{S}(t)$, versus time, t, in seconds.

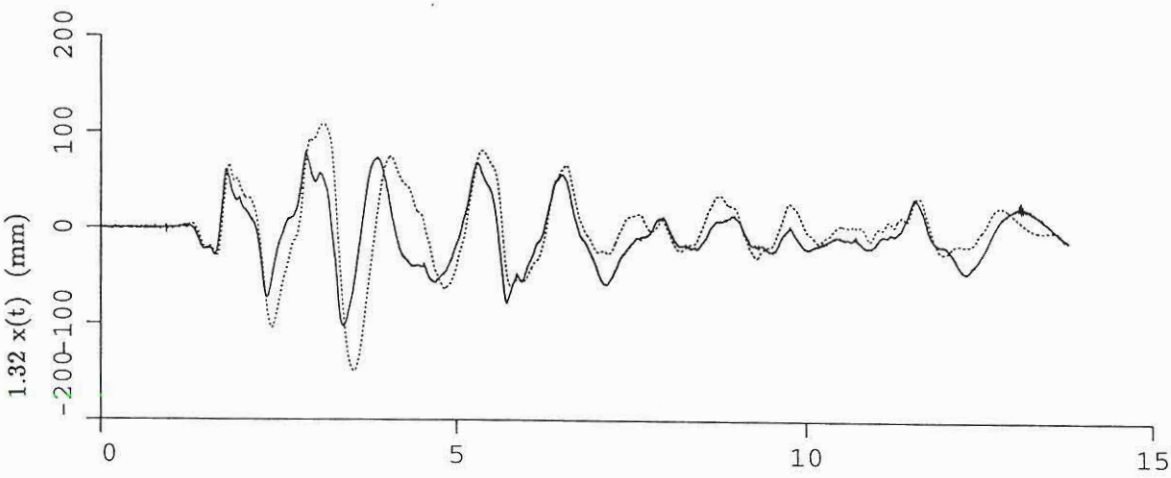

Figure 10. The prediction performance of the suited hysteretic model for RUN2 in RUN3 case. Displacement of the top storey, $1.32x(t)$ and $1.32\hat{x}(t)$ in mm, versus time, t, in seconds.

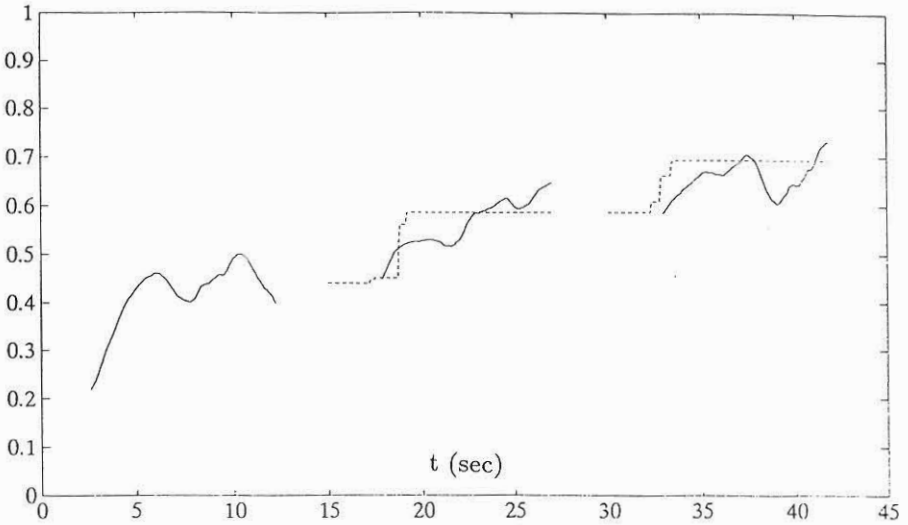

Figure 11. The prediction performance of the suited hysteretic model for RUN2 in RUN3 case. Softening, $S^{ARMA}(t)$ and $\hat{S}(t)$, versus time, t, in seconds.

Figure 12 shows the results obtained in earlier works by MDOF modelling of this structure using non-linear beam theories. The computer programs used in these are SARCF-II [10] and SARCOF [7]. A comparison of figure 12 with figures 6, 8 and 10 show that the proposed model fits better than the other two approaches, primarily because of the degrading model of the $\alpha(D(t))$ parameter.

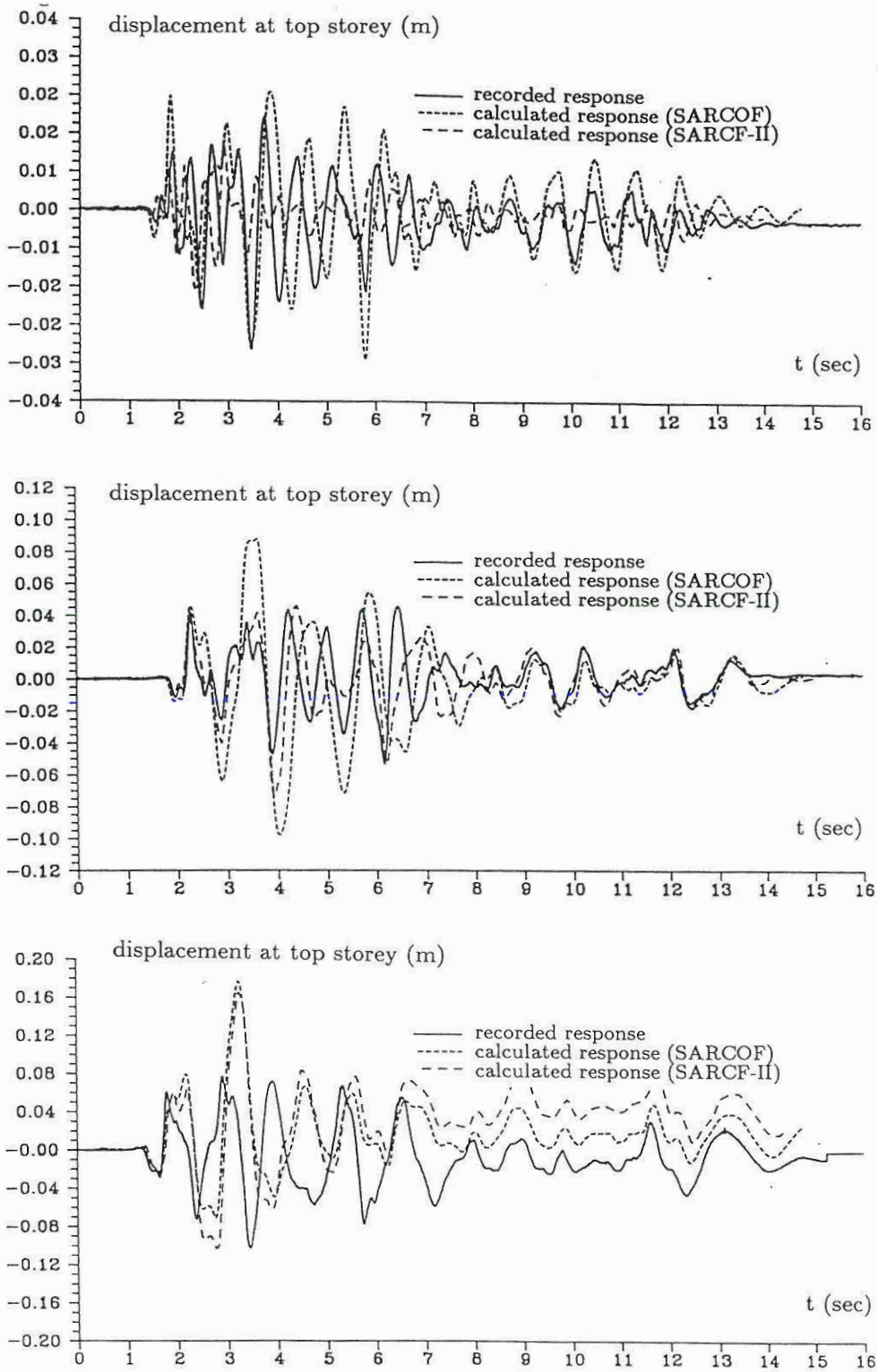

Figure 12. The performance of earlier models using SARCF-II and SARCOF for RUN1, RUN2 and RUN3. Displacement of the top storey in mm, versus time, t, in seconds.

8. CONCLUSIONS

A robust method is developed for the prediction of global and localized damage and the future reliability estimation of partly damaged reinforced concrete (RC) structures under seismic excitation. A global maximum softening damage indicator is considered based on the variation of the eigenfrequency of the first mode due to the stiffness and strength deterioration of the structure. The hysteresis of the first mode is modelled by a Clough and Johnston hysteretic oscillator [1], with degrading elastic fraction of the restoring force. The linear parameters of the model are assumed to be known, measured before the arrival of the first earthquake from non-destructive vibration tests or via structural analysis. The previous excitation and displacement response time series is employed for the identification of the instantaneous softening using an ARMA model. The hysteresis parameters are updated after each earthquake. The proposed model is next generalized for the MDOF system. Using the adapted models for the structure and the global damage state, the global damage in a future earthquake can then be estimated if a suitable earthquake model is applied. The performance of the model is illustrated by RC frames which were tested by Sözen and his associates [2,4] and the predicted results in terms of instantaneous softening and top storey displacement are in very good agreement with the ones recorded during the experiments.

9. ACKNOWLEDGEMENTS

The present research was partially supported by The Danish Technical Research Council within the research programme Dynamics of Structures.

10. REFERENCES

1. W. Clough and S.B. Johnston, 'Effect of Stiffness Degradation on Earthquake Ductility Requirements', *Proc. 2nd Japan Earthquake Symposium* 227-232 (1966).

2. H. Çeçen, 'Response of Ten Storey, Reinforced Concrete Model Frames to Simulated Earthquakes', Ph.D. thesis, University of Illinois at Urbana Champaign , 1979.

3. E. DiPasquale and A.Ş. Çakmak, A.Ş. 'Detection of Seismic Structural Damage using Parameter-Based Global Damage Indices', *Probabilistic Engineering Mechanics* **5**, 60-65 (1990).

4. T.J. Healey and M.A. Sözen 'Experimental Study of the Dynamic Response of a Ten Storey Reinforced Concrete with a Tail First Storey'. Report No. UILU-ENG-78-2012, University of Illinois at Urbana Champaign, 1978.

5. L. Ljung, 'System Identification Theory for the User', Prentice-Hall NewJersey U.S.A., 1987.

6. R. Minai and Y. Suzuki, 'Seismic Reliability Analysis of Building Structures', *Proc. ROC-Japan Joint Seminar on Multiple Hazards Mitigation*, National Taiwan University, Taiwan, ROC, March 1985, 193-207.

7. K.J. Mørk, 'Response Analysis of Reinforced Concrete Structures under Seismic Ex-

citation',*Earthquake Engineering and Structural Dynamics* **23** 33-48, (1993).

8. S.R.K. Nielsen and A.Ş. Çakmak, 'Evaluation of Maximum Softening as a Damage Indicator for Reinforced Concrete under Seismic Excitation', *Proc. First Int. Con. on Computational Stochastic Mechanics*, eds: Spanos and Brebbia, 169-184 (1992).

9. S.R.K. Nielsen, H.U. Köylüoğlu and A.Ş. Çakmak, 'One- and Two-Dimensional Maximum Softening Damage Indicators for Reinforced Concrete Structures under Seismic Excitation', *Soil Dynamics and Earthquake Engineering* **11**, 435-443 (1993).

10. S. Rodriguez-Gomez, Y.S. Chung and C. Meyer, 'SARCF-II User's Guide. Seismic Analysis of Reinforced Concrete Frames', Technical Report NCEER-90-27, National Center for Earthquake Engineering Research, State University of Buffalo, 1990.

PERTURBATION SOLUTIONS FOR RANDOM LINEAR STRUCTURAL SYSTEMS SUBJECT TO RANDOM EXCITATION USING STOCHASTIC DIFFERENTIAL EQUATIONS

H.U. Köylüoğlu
Department of Civil Engineering and Operations Research, Princeton University, Princeton, NJ 08544, USA

S.R.K. Nielsen
Department of Building Technology and Structural Engineering, Aalborg University, Sohngaardsholmsvej 57, DK-9000 Aalborg, Denmark

A.Ş. Çakmak
Department of Civil Engineering and Operations Research, Princeton University, Princeton, NJ 08544, USA

SUMMARY

The paper deals with the first and second order statistical moments of the response of linear systems with random parameters subject to random excitation modelled as white-noise multiplied by an envelope function with random parameters. The method of analysis is basically a second order perturbation method using stochastic differential equations. The joint statistical moments entering the perturbation solution are determined by considering an augmented dynamic system with state variables made up of the displacement and velocity vector and their first and second derivatives with respect to the random parameters of the problem. Equations for partial derivatives are obtained from the partial differentiation of the equations of motion. The zero time-lag joint statistical moment equations for the augmented state vector are derived from the Itô differential formula. General formulation is given for multi-degree-of-freedom (MDOF) systems and the method is illustrated for a single-degree-of-freedom (SDOF) oscillator. The results are compared to those of exact results for a random oscillator subject to white noise excitation with random intensity.

1. INTRODUCTION

Structural uncertainties due to physical imperfections, model inaccuracies and system complexities are spatially distributed over the structure and can be mathematically modelled using either random variables or random processes which may be functions of time and/or space. The uncertainty of the structural model parameters and of the excitation parameters may induce uncertainty in the system response of the same magnitude as the random dynamic loads, and should therefore be included in the analysis. In the 1980s, the analysis of the response variability of stochastic structural systems

recieved a lot of attention, consequently a new field, "Stochastic Finite Elements" was coined to stochastic mechanics. Although there have been papers on computationally expensive Monte Carlo solutions and reliability considerations, most of the studies done in stochastic finite elements have been on the second moment analysis of the response of stochastic systems under deterministic loading. The developments in this field are reviewed in [17,2,6,8,3]. This paper considers the approximate solution methods for the stochastic differential equations arising in stochastic finite elements for dynamic problems. In this respect, ordinary perturbations [9], mean-centered second-order perturbation solutions [15,11,5,12] and orthogonal polynomial expansions for the covariances [10] have been proposed as solution procedures. Divergent secular terms have been detected in the time domain analysis [9,15,12] and these are cured in the frequency domain [11,12]. The partial derivatives of the response processes with respect to random variables are proportional to time, hence perturbation solutions carry divergent secular terms and might blow up with time for undamped systems. For damped systems, since the divergent secular terms are under the governing control of the exponential damping decay, the existing deviations in the perturbation solutions become neither observable nor important with time [12].

For the random vibration of random systems, Chang and Yang [5] developed a mean-centered approximate second-order perturbation method in conjuction with modal expansion and an iterative scheme to solve non-linear dynamic problems for a beam element with structural uncertainities subject to Gaussian white noise excitation. They employed equivalent linearization with Gaussian closure to obtain equivalent linear system stiffness matrix and the local averaging method of Vanmarcke [18] to discretize random fields, thus, it is necessary to investigate the sensitivity of the response statistics to the density of the finite element mesh. Jensen and Iwan [10] employed an expansion of the covariances of the response in terms of a series of orthogonal polynomials that depend on the coefficients of the spectral decomposition of the uncertain parameters of the system. The accuracy of the approximation increases as the number of terms in the expansion is increased. Increase in the number of terms in the expansion is used to solve problems with high variabilities.

The authors have previously considered the stationary response of random linear elastic [13] as well as geometrically non-linear frame structures [14] subject to stationary random excitation based on a second order perturbation analysis. The random fields of the structure have been discretized by the weighted integral method of Deodatis [7] and Takada [16] in which Galerkin finite elements with deterministic shape functions are applied to stochastic differential equations. This provides consistency in the discretization of the random fields since the deterministic continuum and the random field are discretized by the same shape functions. The stochastic analysis of the geometrically non-linear structure was performed by an equivalent linearization approach in combination with a spectral approach. Since only the stationary response characteristics are to be computed, secular terms never arised. In both studies, the effects of the variability and the correlation length of the random fields of concern on the response are parametrically examined. Through comparisons with extensive Monte Carlo simulations and analytically available results, the second order perturbation method is observed to be a good

approximation for variabilities up to 25-30 per cent.

Stochastic response of linear systems subject to white noise can be studied by means of Itô stochastic differential equations [1]. For random dynamic systems, the stochastic differential equations of motion have random coefficients. In this paper a second order perturbation method is developed for the stationary or non-stationary statistical moments of the response of MDOF structural systems subject to Gaussian white noise excitation multiplied by an envelope with random parameters, based on stochastic differential equations. The coefficients in the perturbation solution for the covariance are made up of time-dependent zero-time lag joint statistical moments of the responses and their first and second partial derivatives with respect to the random parameters. The necessary expectations are determined considering a sequence of augmented dynamic systems with the state vector made up of the displacement and velocity and their first and second derivatives with respect to the random parameters. This provides a very compact notation. Equations for the partial derivatives are obtained from the differentiation of the equations of motion.

The method is illustrated on a random linear SDOF oscillator subject to white noise excitation with random intensity. The obtained results have been compared to exact ones. The exact reults are obtained via the application of the total probability to the conditional analytical results.

2. LINEAR RANDOM MDOF STRUCTURAL SYSTEMS

The equations of motion of linear MDOF systems with random parameters subject to random excitation modelled as unit white noise multiplied by an envelope matrix with random parameters are

$$\mathbf{M}(\mathbf{X})\ddot{\mathbf{Y}}(\mathbf{X},t) + \mathbf{C}(\mathbf{X})\dot{\mathbf{Y}}(\mathbf{X},t) + \mathbf{K}(\mathbf{X})\mathbf{Y}(\mathbf{X},t) = \mathbf{Q}(\mathbf{X},t)\mathbf{W}(t) \tag{1}$$

where $\mathbf{M}(\mathbf{X})$, $\mathbf{C}(\mathbf{X})$ and $\mathbf{K}(\mathbf{X})$ are random mass, damping and stiffness matrices of dimension $p \times p$. $\mathbf{X}$ is a vector of dimension $d \times 1$ denoting all random variables of the structural and the load models. $\mathbf{Q}(\mathbf{X},t)$ is a matrix of dimension $p \times r$ indicating the envelope functions with random parameters. $\{\mathbf{W}(t), t \in]-\infty,\infty[\}$ is a vector of dimension $r \times 1$ of mutually independent unit white noise processes, i.e. a Gaussian process with the mean value and auto-covariance function as

$$E\big[W_\alpha(t)\big] = 0 \tag{2}$$

$$E\big[W_\alpha(t_1)W_\beta(t_2)\big] = \delta(t_1 - t_2)\delta_{\alpha\beta} \tag{3}$$

where $\delta(t_1 - t_2)$ signifies Dirac's delta function and $\delta_{\alpha\beta}$ is the Kronecker's delta. $\mathbf{X}^T = [X_1, \ldots, X_d]$ are zero-mean random variables with the covariances $\kappa_{X_i X_j}$, i.e.

$$E[X_i] = 0 \tag{4}$$

$$E[X_i X_j] = \kappa_{X_i X_j} \tag{5}$$

$X_1, \ldots, X_d$, which will be referred to as the basic variables, are all assumed to be stochastically independent of the external excitation process $\{\mathbf{W}(t), t \in]-\infty, \infty[\}$.

Consider the following Taylor expansion of the structural random matrices and the excitation envelope matrix in terms of random parameters.

$$\left.\begin{aligned}
\mathbf{M}(\mathbf{X}) &= \mathbf{m}_0 + \mathbf{m}_i X_i + \frac{1}{2}\mathbf{m}_{ij} X_i X_j + \cdots \\
\mathbf{C}(\mathbf{X}) &= \mathbf{c}_0 + \mathbf{c}_i X_i + \frac{1}{2}\mathbf{c}_{ij} X_i X_j + \cdots \\
\mathbf{K}(\mathbf{X}) &= \mathbf{k}_0 + \mathbf{k}_i X_i + \frac{1}{2}\mathbf{k}_{ij} X_i X_j + \cdots \\
\mathbf{Q}(\mathbf{X}, t) &= \mathbf{q}_0(t) + \mathbf{q}_i(t) X_i + \frac{1}{2}\mathbf{q}_{ij}(t) X_i X_j + \cdots
\end{aligned}\right\} \tag{6}$$

where $\mathbf{m}_0 = \mathbf{M}(\mathbf{0})$, $\mathbf{m}_i = \frac{\partial}{\partial x_i}\mathbf{M}(\mathbf{0})$, $\mathbf{m}_{ij} = \frac{\partial^2}{\partial x_i x_j}\mathbf{M}(\mathbf{0})$, etc. and the summation convention is applied over the dummy indices $i, j = 1, 2, \ldots, d$. $\mathbf{m}_0$, $\mathbf{c}_0$, $\mathbf{k}_0$, $\mathbf{m}_i$, $\mathbf{c}_i$, $\mathbf{k}_i$, $\mathbf{m}_{ij}$, $\mathbf{c}_{ij}$ and $\mathbf{k}_{ij}$ $i, j = 1, 2, \ldots, d$ are deterministic constant matrices of dimension $p \times p$. $\mathbf{q}_0(t)$, $\mathbf{q}_i(t)$ and $\mathbf{q}_{ij}(t)$ $i, j = 1, 2, \ldots, d$ are deterministic matrices of dimension $p \times r$ which are functions of time.

The displacement response process $\{\mathbf{Y}(\mathbf{X}, t), t \in [0, \infty[\}$ and the velocity response process $\{\dot{\mathbf{Y}}(\mathbf{X}, t), t \in [0, \infty[\}$ of (1) are random partly because of the functional dependency of the external excitation process and partly because of the random basic variables $\mathbf{X}$. $\{\mathbf{Y}(\mathbf{0}, t), t \in [0, \infty[\}$ and $\{\dot{\mathbf{Y}}(\mathbf{0}, t), t \in [0, \infty[\}$ indicate the response process on condition of $\mathbf{X} = \mathbf{0}$, i.e. the stochastic displacement process obtained from (1) with mean values for the basic variables. Consider the following Taylor expansion of the stochastic system from the mean value system to the second order in the basic variables $X_1, \ldots, X_d$

$$Y_m(\mathbf{X}, t) \simeq Y_m(\mathbf{0}, t) + Y_{m,x_i}(\mathbf{0}, t) X_i + \frac{1}{2} Y_{m,x_i x_j}(\mathbf{0}, t) X_i X_j + \cdots \quad m = 1.2, \ldots, p \tag{7}$$

$$\dot{Y}_m(\mathbf{X}, t) \simeq \dot{Y}_m(\mathbf{0}, t) + \dot{Y}_{m,x_i}(\mathbf{0}, t) X_i + \frac{1}{2} \dot{Y}_{m,x_i x_j}(\mathbf{0}, t) X_i X_j + \cdots \quad m = 1.2, \ldots, p \tag{8}$$

where $Y_{m,x_i}(\mathbf{0}, t) = \frac{\partial}{\partial x_i} Y_m(0.t)$ etc. Further, the summation convention has been applied for the dummy indices $i, j = 1, \ldots, d$. Use of (7), (8) and retaining terms up to the second order in the basic variables provides the following approximation for the

unconditional covariance of the response processes.

$$\kappa_{Y_m Y_n}(t) = E\big[Y_m(\mathbf{X},t)Y_n(\mathbf{X},t)\big] =$$

$$E\big[Y_m(\mathbf{0},t)Y_n(\mathbf{0},t)\big] + E\big[Y_m(\mathbf{0},t)Y_{n,x_i}(\mathbf{0},t)X_i\big] + E\big[Y_n(\mathbf{0},t)Y_{m,x_i}(\mathbf{0},t)X_i\big] +$$

$$E\Big[\big\{Y_{m,x_i}(\mathbf{0},t)Y_{n,x_j}(\mathbf{0},t) + \frac{1}{2}Y_m(\mathbf{0},t)Y_{n,x_ix_j}(\mathbf{0},t) + \frac{1}{2}Y_n(\mathbf{0},t)Y_{m,x_ix_j}(\mathbf{0},t)\big\}X_iX_j\Big] + \cdots$$

$$\simeq E\big[Y_m(\mathbf{0},t)Y_n(\mathbf{0},t)\big] +$$

$$\Big\{E\big[Y_{m,x_i}(\mathbf{0},t)Y_{n,x_j}(\mathbf{0},t)\big] + \frac{1}{2}E\big[Y_m(\mathbf{0},t)Y_{n,x_ix_j}(\mathbf{0},t)\big] + \frac{1}{2}E\big[Y_n(\mathbf{0},t)Y_{m,x_ix_j}(\mathbf{0},t)\big]\Big\}\kappa_{X_iX_j} \tag{9}$$

$$\kappa_{\dot{Y}_m \dot{Y}_n}(t) = E\big[\dot{Y}_m(\mathbf{X},t)\dot{Y}_n(\mathbf{X},t)\big] \simeq E\big[\dot{Y}_m(\mathbf{0},t)\dot{Y}_n(\mathbf{0},t)\big] +$$

$$\Big\{E\big[\dot{Y}_{m,x_i}(\mathbf{0},t)\dot{Y}_{n,x_j}(\mathbf{0},t)\big] + \frac{1}{2}E\big[\dot{Y}_m(\mathbf{0},t)\dot{Y}_{n,x_ix_j}(\mathbf{0},t)\big] + \frac{1}{2}E\big[\dot{Y}_n(\mathbf{0},t)\dot{Y}_{m,x_ix_j}(\mathbf{0},t)\big]\Big\}\kappa_{X_iX_j} \tag{10}$$

$$\kappa_{Y_m \dot{Y}_n}(t) = E\big[Y_m(\mathbf{X},t)\dot{Y}_n(\mathbf{X},t)\big] \simeq E\big[Y_m(\mathbf{0},t)\dot{Y}_n(\mathbf{0},t)\big] +$$

$$\Big\{E\big[Y_{m,x_i}(\mathbf{0},t)\dot{Y}_{n,x_j}(\mathbf{0},t)\big] + \frac{1}{2}E\big[Y_m(\mathbf{0},t)\dot{Y}_{n,x_ix_j}(\mathbf{0},t)\big] + \frac{1}{2}E\big[\dot{Y}_n(\mathbf{0},t)Y_{m,x_ix_j}(\mathbf{0},t)\big]\Big\}\kappa_{X_iX_j} \tag{11}$$

In deriving (9), (10) and (11) zero mean response has been assumed, i.e. $E\big[\mathbf{Y}(\mathbf{0},t)\big] = E\big[\dot{\mathbf{Y}}(\mathbf{0},t)\big] = \mathbf{0}$. Further, the independence of the basic variables on the white noise excitation processes is used.

In order to evaluate the expectations on the right hand sides of these solutions, stochastic differential equations must be formulated specifying the development of $\mathbf{Y}(\mathbf{0},t)$, $\dot{\mathbf{Y}}(\mathbf{0},t)$ and of the partial derivatives $\mathbf{Y}_{,x_i}(\mathbf{0},t)$, $\dot{\mathbf{Y}}_{,x_j}(\mathbf{0},t)$, $\mathbf{Y}_{,x_ix_j}(\mathbf{0},t)$, $\dot{\mathbf{Y}}_{,x_ix_j}(\mathbf{0},t)$. These are obtained from partial differentiation of (1) with respect the basic variables, evaluated at the mean structure $\mathbf{X} = \mathbf{0}$ and from the expansions listed in equation (4). A sufficient condition for the development of these state variables fulfilling the resulting equations is obtained if the mentioned state variables fulfil the following differential equations.

$$\mathbf{m}_0\ddot{\mathbf{Y}}(\mathbf{0},t) + \mathbf{c}_0\dot{\mathbf{Y}}(\mathbf{0},t) + \mathbf{k}_0\mathbf{Y}(\mathbf{0},t) = \mathbf{q}_0(t)\mathbf{W}(t) \tag{12}$$

$$\begin{aligned}
&\mathbf{m}_0\ddot{\mathbf{Y}}_{,x_i}(\mathbf{0},t) + \mathbf{c}_0\dot{\mathbf{Y}}_{,x_i}(\mathbf{0},t) + \mathbf{k}_0\mathbf{Y}_{,x_i}(\mathbf{0},t) = \\
&-\mathbf{m}_i\ddot{\mathbf{Y}}(\mathbf{0},t) - \mathbf{c}_i\dot{\mathbf{Y}}(\mathbf{0},t) - \mathbf{k}_i\mathbf{Y}(\mathbf{0},t) + \mathbf{q}_i(t)\mathbf{W}(t) = \\
&-\mathbf{m}_i\mathbf{m}_0^{-1}\big[-\mathbf{c}_0\dot{\mathbf{Y}}(\mathbf{0},t) - \mathbf{k}_0\mathbf{Y}(\mathbf{0},t) + \mathbf{q}_0(t)\mathbf{W}(t)\big] \\
&-\mathbf{c}_i\dot{\mathbf{Y}}(\mathbf{0},t) - \mathbf{k}_i\mathbf{Y}(\mathbf{0},t) + \mathbf{q}_i(t)\mathbf{W}(t) = \\
&\big(\mathbf{m}_i\mathbf{m}_0^{-1}\mathbf{c}_0 - \mathbf{c}_i\big)\dot{\mathbf{Y}}(\mathbf{0},t) + \big(\mathbf{m}_i\mathbf{m}_0^{-1}\mathbf{k}_0 - \mathbf{k}_i\big)\mathbf{Y}(\mathbf{0},t) + \\
&\big(\mathbf{q}_i(t) - \mathbf{m}_i\mathbf{m}_0^{-1}\mathbf{q}_0(t)\big)\mathbf{W}(t)
\end{aligned} \tag{13}$$

$$
\begin{aligned}
&\mathrm{m}_0\ddot{\mathrm{Y}}_{,x_ix_j}(0,t)+\mathrm{c}_0\dot{\mathrm{Y}}_{,x_ix_j}(0,t)+\mathrm{k}_0\mathrm{Y}_{,x_ix_j}(0,t)=\\
&-\mathrm{m}_i\ddot{\mathrm{Y}}_{,x_j}(0,t)-\mathrm{m}_j\ddot{\mathrm{Y}}_{,x_i}(0,t)-\mathrm{m}_{ij}\ddot{\mathrm{Y}}(0,t)-\mathrm{c}_i\dot{\mathrm{Y}}_{,x_j}(0,t)-\mathrm{c}_j\dot{\mathrm{Y}}_{,x_i}(0,t)-\\
&\mathrm{c}_{ij}\dot{\mathrm{Y}}(0,t)-\mathrm{k}_i\mathrm{Y}_{,x_j}(0,t)-\mathrm{k}_j\mathrm{Y}_{,x_i}(0,t)-\mathrm{k}_{ij}\mathrm{Y}(0,t)+\mathrm{q}_{ij}(t)\mathrm{W}(t)=\\
&-\mathrm{m}_i\mathrm{m}_0^{-1}\Big\{\big(\mathrm{m}_j\mathrm{m}_0^{-1}\mathrm{c}_0-\mathrm{c}_j\big)\dot{\mathrm{Y}}(0,t)+\big(\mathrm{m}_j\mathrm{m}_0^{-1}\mathrm{k}_0-\mathrm{k}_j\big)\mathrm{Y}(0,t)+\\
&\big(\mathrm{q}_j(t)-\mathrm{m}_j\mathrm{m}_0^{-1}\mathrm{q}_0(t)\big)\mathrm{W}(t)-\mathrm{c}_0\dot{\mathrm{Y}}_{,x_j}(0,t)-\mathrm{k}_0\mathrm{Y}_{,x_j}(0,t)\Big\}-\\
&\mathrm{m}_j\mathrm{m}_0^{-1}\Big\{\big(\mathrm{m}_i\mathrm{m}_0^{-1}\mathrm{c}_0-\mathrm{c}_i\big)\dot{\mathrm{Y}}(0,t)+\big(\mathrm{m}_i\mathrm{m}_0^{-1}\mathrm{k}_0-\mathrm{k}_i\big)\mathrm{Y}(0,t)+\\
&\big(\mathrm{q}_i(t)-\mathrm{m}_i\mathrm{m}_0^{-1}\mathrm{q}_0(t)\big)\mathrm{W}(t)-\mathrm{c}_0\dot{\mathrm{Y}}_{,x_i}(0,t)-\mathrm{k}_0\mathrm{Y}_{,x_i}(0,t)\Big\}-\\
&\mathrm{m}_{ij}\mathrm{m}_0^{-1}\big[-\mathrm{c}_0\dot{\mathrm{Y}}(0,t)-\mathrm{k}_0\mathrm{Y}(0,t)+\mathrm{q}_0(t)\mathrm{W}(t)\big]-\\
&\mathrm{c}_i\dot{\mathrm{Y}}_{,x_j}(0,t)-\mathrm{c}_j\dot{\mathrm{Y}}_{,x_i}(0,t)-\mathrm{c}_{ij}\dot{\mathrm{Y}}(0,t)-\\
&\mathrm{k}_i\mathrm{Y}_{,x_j}(0,t)-\mathrm{k}_j\mathrm{Y}_{,x_i}(0,t)-\mathrm{k}_{ij}\mathrm{Y}(0,t)+\mathrm{q}_{ij}(t)\mathrm{W}(t)
\end{aligned}
\tag{14}
$$

(12), (13) and (14) can next be combined into the following closed system of equivalent 1st order stochastic differential equations

$$
\dot{\mathrm{Z}}(t)=\mathrm{A}\mathrm{Z}(t)+\mathrm{b}(t)\mathrm{W}(t)\quad,\quad \mathrm{Z}(0)=0 \tag{15}
$$

$$
\mathrm{Z}(t)=\begin{bmatrix}
\mathrm{Y}(0,t)\\
\dot{\mathrm{Y}}(0,t)\\
\mathrm{Y}_{,x_i}(0,t)\\
\dot{\mathrm{Y}}_{,x_i}(0,t)\\
\mathrm{Y}_{,x_j}(0,t)\\
\dot{\mathrm{Y}}_{,x_j}(0,t)\\
\mathrm{Y}_{,x_ix_j}(0,t)\\
\dot{\mathrm{Y}}_{,x_ix_j}(0,t)
\end{bmatrix}
$$

$$
\mathrm{b}(t)=\begin{bmatrix}
0\\
\mathrm{m}_0^{-1}\mathrm{q}_0(t)\\
0\\
-\mathrm{m}_0^{-1}(\mathrm{m}_i\mathrm{m}_0^{-1}\mathrm{q}_0(t)-\mathrm{q}_i(t))\\
0\\
-\mathrm{m}_0^{-1}(\mathrm{m}_j\mathrm{m}_0^{-1}\mathrm{q}_0(t)-\mathrm{q}_j(t))\\
0\\
\mathrm{m}_0^{-1}\Big[(\mathrm{m}_i\mathrm{m}_0^{-1}\mathrm{m}_j+\mathrm{m}_j\mathrm{m}_0^{-1}\mathrm{m}_i-\mathrm{m}_{ij})\mathrm{m}_0^{-1}\mathrm{q}_0(t)-\mathrm{m}_j\mathrm{m}_0^{-1}\mathrm{q}_i(t)-\mathrm{m}_i\mathrm{m}_0^{-1}\mathrm{q}_j(t)+\mathrm{q}_{ij}(t)\Big]
\end{bmatrix}
\tag{16}
$$

$$\mathbf{A} = \begin{bmatrix} \mathbf{0} & \mathbf{I} & \mathbf{0} & \mathbf{0} & \mathbf{0} & \mathbf{0} & \mathbf{0} & \mathbf{0} \\ -\mathbf{m}_0^{-1}\mathbf{k}_0 & -\mathbf{m}_0^{-1}\mathbf{c}_0 & \mathbf{0} & \mathbf{0} & \mathbf{0} & \mathbf{0} & \mathbf{0} & \mathbf{0} \\ \mathbf{0} & \mathbf{0} & \mathbf{0} & \mathbf{I} & \mathbf{0} & \mathbf{0} & \mathbf{0} & \mathbf{0} \\ \mathbf{G}_i & \mathbf{H}_i & -\mathbf{m}_0^{-1}\mathbf{k}_0 & -\mathbf{m}_0^{-1}\mathbf{c}_0 & \mathbf{0} & \mathbf{0} & \mathbf{0} & \mathbf{0} \\ \mathbf{0} & \mathbf{0} & \mathbf{0} & \mathbf{0} & \mathbf{0} & \mathbf{I} & \mathbf{0} & \mathbf{0} \\ \mathbf{G}_j & \mathbf{H}_j & \mathbf{0} & \mathbf{0} & -\mathbf{m}_0^{-1}\mathbf{k}_0 & -\mathbf{m}_0^{-1}\mathbf{c}_0 & \mathbf{0} & \mathbf{0} \\ \mathbf{0} & \mathbf{0} & \mathbf{0} & \mathbf{0} & \mathbf{0} & \mathbf{0} & \mathbf{0} & \mathbf{I} \\ \mathbf{G}_{ij} & \mathbf{H}_{ij} & \mathbf{m}_0^{-1}\mathbf{m}_j\mathbf{m}_0^{-1}\mathbf{k}_0 & \mathbf{m}_0^{-1}\mathbf{m}_j\mathbf{m}_0^{-1}\mathbf{c}_0 & \mathbf{m}_0^{-1}\mathbf{m}_i\mathbf{m}_0^{-1}\mathbf{k}_0 & \mathbf{m}_0^{-1}\mathbf{m}_i\mathbf{m}_0^{-1}\mathbf{c}_0 & -\mathbf{m}_0^{-1}\mathbf{k}_0 & -\mathbf{m}_0^{-1}\mathbf{c}_0 \end{bmatrix} \tag{17}$$

$$\left.\begin{aligned} \mathbf{G}_i &= \mathbf{m}_0^{-1}(\mathbf{m}_i\mathbf{m}_0^{-1}\mathbf{k}_0 - \mathbf{k}_i) \\ \mathbf{H}_i &= \mathbf{m}_0^{-1}(\mathbf{m}_i\mathbf{m}_0^{-1}\mathbf{c}_0 - \mathbf{c}_i) \\ \mathbf{G}_{ij} &= \mathbf{m}_0^{-1}[\mathbf{m}_j\mathbf{m}_0^{-1}(\mathbf{k}_i - \mathbf{m}_i\mathbf{m}_0^{-1}\mathbf{k}_0) + \mathbf{m}_i\mathbf{m}_0^{-1}(\mathbf{k}_j - \mathbf{m}_j\mathbf{m}_0^{-1}\mathbf{k}_0) + \mathbf{m}_{ij}\mathbf{m}_0^{-1}\mathbf{k}_0] \\ \mathbf{H}_{ij} &= \mathbf{m}_0^{-1}[\mathbf{m}_j\mathbf{m}_0^{-1}(\mathbf{c}_i - \mathbf{m}_i\mathbf{m}_0^{-1}\mathbf{c}_0) + \mathbf{m}_i\mathbf{m}_0^{-1}(\mathbf{c}_j - \mathbf{m}_j\mathbf{m}_0^{-1}\mathbf{c}_0) + \mathbf{m}_{ij}\mathbf{m}_0^{-1}\mathbf{c}_0] \end{aligned}\right\} \tag{18}$$

Zero initial conditions of the system have been assumed as shown in (15). The white noise excited system in (15) is the engineering interpretation of a Stratonovich differential system with linear drift-vector $\mathbf{AZ}(t)$ and diffusion vector $\mathbf{b}(t)$. Since the diffusion vector is state independent, the Stratonovich and Itô interpretation of equation (15) are identical with probability 1 [1].

The state vector $\mathbf{Z}(t)$ has the dimension $N = 2p + 4pd + 2pd^2$. If the basic variables are assumed to be uncorrelated, only the coefficients for $i = j$ in the inner sums on the right hand sides of (9), (10) and (11) contribute. Moreover, since partial derivatives with respect to i and j are identical, the coefficients can be determined from the differential system for the following reduced state state vector of the dimension $N = 6p$ for a fixed i.

$$\mathbf{Z}^T(t) = \left[\mathbf{Y}(0,t), \dot{\mathbf{Y}}(0,t), \mathbf{Y}_{,x_i}(0,t), \dot{\mathbf{Y}}_{,x_i}(0,t), \mathbf{Y}_{,x_ix_i}(0,t), \dot{\mathbf{Y}}_{,x_ix_i}(0,t)\right] \tag{19}$$

Here, the differential equations for the state vector (19) is obtained as a sub-system of (16).

3. DIFFERENTIAL EQUATIONS FOR STATISTICAL MOMENTS

(15) is a linear stochastic differential equation subject to Gaussian white noise, therefore, the state vector $\mathbf{Z}(t)$ is Gaussian. Further, the system has zero initial values, thus, $E[\mathbf{Z}(t)] = \mathbf{0}$. The covariances of $\mathbf{Z}(t)$ fully describe the joint probability density function of $\mathbf{Z}(t)$. Applying the Itô-formula and then performing the expectations, the following differential equations and associated initial values are obtained for the covariances, $\mu_{ij}(t) = E[Z_i(t)Z_j(t)]$, see e.g [1].

$$\dot{\mu}_{ij}(t) = A_{ik}\mu_{kj}(t) + A_{jk}\mu_{ki}(t) + b_i(t)b_j(t) \quad , \quad \mu_{ij}(0) = 0 \tag{20}$$

where summation convention is applied on dummy index $k = 1, 2, \ldots, N$.

4. LINEAR SDOF RANDOM OSCILLATOR

Next, the method is illustrated for a linear random SDOF oscillator subject to white noise excitation with random intensity. The equation of motion of a SDOF linear oscillator with random parameters subject to white noise excitation with random intensity is

$$M(\mathbf{X})\ddot{Y}(\mathbf{X},t) + C(\mathbf{X})\dot{Y}(\mathbf{X},t) + K(\mathbf{X})Y(\mathbf{X},t) = Q(\mathbf{X})W(t) \tag{21}$$

where $M(\mathbf{X})$, $C(\mathbf{X})$ and $K(\mathbf{X})$ are random mass, damping and stiffness. $Q(\mathbf{X})$ indicates the random intensity of the excitation which is taken as time-invariant in this problem. $\{W(t), t \in]-\infty, \infty[\}$ is a unit white noise process.

The four random parameters, entering the above equations are all modelled as random variables written on the following form.

$$\left.\begin{aligned} M(\mathbf{X}) &= m_0(1+X_1) \\ C(\mathbf{X}) &= c_0(1+X_2) \\ K(\mathbf{X}) &= k_0(1+X_3) \\ Q(\mathbf{X}) &= q_0(1+X_4) \end{aligned}\right\} \tag{22}$$

where $\mathbf{X}^T = [X_1, \ldots, X_4]$ are zero-mean random variables with the co-variances $\kappa_{X_iX_j}$. As previously, these random variables referred to as the basic variables are all assumed to be stochastically independent of the external excitation process $\{W(t), t \in]-\infty, \infty[\}$.

Equation (22) states that $m_1 = m_0$, $m_2 = m_3 = m_4 = 0$, $c_2 = c_0$, $c_1 = c_3 = c_4 = 0$, $k_3 = k_0$, $k_1 = k_2 = k_4 = 0$, $q_4 = q_0$, $q_1 = q_2 = q_3 = 0$ and $m_{ij} = c_{ij} = k_{ij} = q_{ij} = 0$ for $i, j = 1, 2, 3, 4$. Kronecker delta is introduced to eliminate the zero terms. For this oscillator problem, (15)-(18) then become

$$\dot{\mathbf{Z}}(t) = \mathbf{A}\mathbf{Z}(t) + \mathbf{b}W(t) \quad , \quad \mathbf{Z}(0) = \mathbf{0} \tag{23}$$

$$\mathbf{Z}(t) = \begin{bmatrix} Y(\mathbf{0},t) \\ \dot{Y}(\mathbf{0},t) \\ Y_{,x_i}(\mathbf{0},t) \\ \dot{Y}_{,x_i}(\mathbf{0},t) \\ Y_{,x_j}(\mathbf{0},t) \\ \dot{Y}_{,x_j}(\mathbf{0},t) \\ Y_{,x_ix_j}(\mathbf{0},t) \\ \dot{Y}_{,x_ix_j}(\mathbf{0},t) \end{bmatrix} \quad , \quad \mathbf{b} = \begin{bmatrix} 0 \\ \frac{q_0}{m_0} \\ 0 \\ -\frac{q_0}{m_0}\delta_{1i} + \frac{q_0}{m_0}\delta_{4i} \\ 0 \\ -\frac{q_0}{m_0}\delta_{1j} + \frac{q_0}{m_0}\delta_{4j} \\ 0 \\ 2\frac{q_0}{m_0}\delta_{1i}\delta_{1j} - \frac{q_0}{m_0}\delta_{1j}\delta_{4i} - \frac{q_0}{m_0}\delta_{1i}\delta_{4j} \end{bmatrix} \tag{24}$$

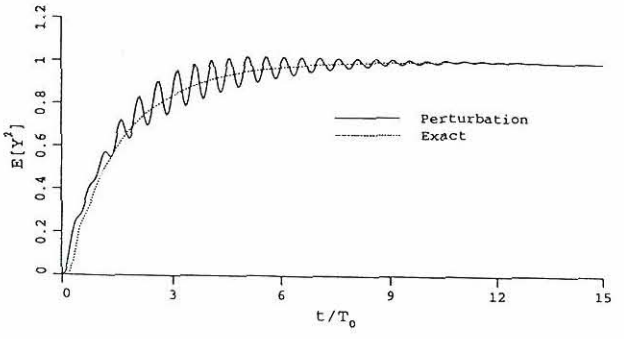

Figure 1. Unconditional variance of displacement, $\kappa_{YY}(t)$, versus undimensional time, $\frac{t}{T_0}$. Only M is random.

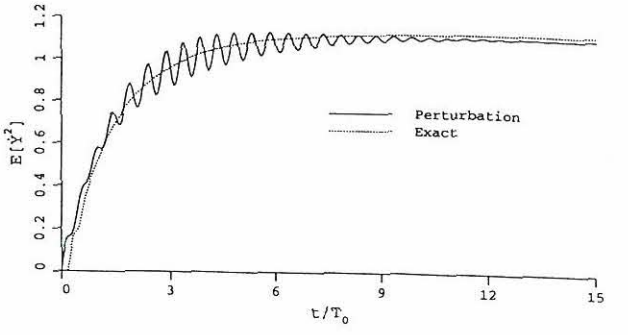

Figure 2. Unconditional variance of velocity, $\kappa_{\dot{Y}\dot{Y}}(t)$, versus undimensional time, $\frac{t}{T_0}$. Only M is random.

$$\mathbf{A} = \begin{bmatrix} 0 & 1 & 0 & 0 & 0 & 0 & 0 & 0 \\ -\frac{k_0}{m_0} & -\frac{c_0}{k_0} & 0 & 0 & 0 & 0 & 0 & 0 \\ 0 & 0 & 0 & 1 & 0 & 0 & 0 & 0 \\ G_i & H_i & -\frac{k_0}{m_0} & -\frac{c_0}{m_0} & 0 & 0 & 0 & 0 \\ 0 & 0 & 0 & 0 & 0 & 1 & 0 & 0 \\ G_j & H_j & 0 & 0 & -\frac{k_0}{m_0} & -\frac{c_0}{m_0} & 0 & 0 \\ 0 & 0 & 0 & 0 & 0 & 0 & 0 & 1 \\ G_{ij} & H_{ij} & \frac{k_0}{m_0}\delta_{1j} & \frac{c_0}{m_0}\delta_{1j} & \frac{k_0}{m_0}\delta_{1i} & \frac{c_0}{m_0}\delta_{1i} & -\frac{k_0}{m_0} & -\frac{c_0}{m_0} \end{bmatrix} \tag{25}$$

$$\left.\begin{aligned} G_i &= \frac{k_0}{m_0}(\delta_{1i} - \delta_{3i}) \\ H_i &= \frac{c_0}{m_0}(\delta_{1i} - \delta_{2i}) \\ G_{ij} &= \frac{k_0}{m_0}(-2\delta_{1i}\delta_{1j} + \delta_{1i}\delta_{3j} + \delta_{3i}\delta_{1j}) \\ H_{ij} &= \frac{c_0}{m_0}(-2\delta_{1i}\delta_{1j} + \delta_{1i}\delta_{2j} + \delta_{2i}\delta_{1j}) \end{aligned}\right\} \tag{26}$$

5. NUMERICAL RESULTS

In what follows, a numerical example is worked out for an SDOF oscillator. The random parameters M, C, K and Q are assumed to be mutually stochastically independent and uniformly distributed, $M \sim U(a_M, b_M)$, $C \sim U(a_C, b_C)$, $K \sim U(a_K, b_K)$, $Q \sim U(a_Q, b_Q)$, where $a_M = E[M](1-\sqrt{3}V[M])$, $b_M = E[M](1+\sqrt{3}V[M])$, etc. The follow-

ing mean values ($E[\cdot]$) and variational coefficients ($V[\cdot]$) are considered.

$$\left.\begin{array}{lll} E[M] = m_0 = 1.0 & , & V[M] = 0.3 \\ E[C] = c_0 = 0.1 & , & V[C] = 0.3 \\ E[K] = k_0 = 1.0 & , & V[\beta] = 0.3 \\ E[Q] = q_0 = \sqrt{2c_0k_0} & , & V[Q] = 0.3 \end{array}\right\} \tag{27}$$

The corresponding circular eigenfrequency, $\omega_0 = \sqrt{\frac{k_0}{m_0}}$, and damping ratio, $\zeta_0 = \frac{c_0}{2m_0\omega_0}$, of the mean oscillator are 1.0 and 0.05, respectively. The variance of the displacement and the velocity of the mean linear oscillator are both equal to 1. The variational coefficients of the parameters also indicate the standard deviation of the zero-mean basic variables X_i defined in (22). The proposed perturbation method is a very good approximation for small variabilities, i.e. small $V[\cdot]$. $V[\cdot] = 0.3$ is a rather high coefficient of variation, almost the limit of the proposed method. The results with $V[\cdot]$ are presented in figures 1-8 to show the performence of the method at such a large variability.

The linear statistical moment differential equations, listed in (20), are numerically solved by a 4th order Runge-Kutta scheme, with time step selected as $\Delta t = T_0/20$, where $T_0 = 2\pi$ is the eigenperiod of the mean linear oscillator. The results obtained by the present approximate second order perturbation method are compared to the exact ones in all the following figures. Since a joint probability function is assigned for the random variables, $f_{\mathbf{X}}(\mathbf{x})$, i.e.,

$$f_{\mathbf{X}}(\mathbf{x}) = \frac{1}{(b_M - a_M)(b_C - a_C)(b_K - a_K)(b_Q - a_Q)} \tag{28}$$

the exact unconditional non-stationary variances, $\kappa_{YY}(t)$ can be computed from the application of the total probability theorem on the conditional non-stationary variances, $\kappa_{YY}(\mathbf{X} = \mathbf{x})$, of the oscillator as

$$\kappa_{YY}(t) = \int_{\mathbf{x}} \kappa_{YY}(t \mid \mathbf{X} = \mathbf{x}) f_{\mathbf{X}}(\mathbf{x}) d\mathbf{x} \tag{29}$$

The non-stationary variances $\kappa_{YY}(t \mid \mathbf{X} = \mathbf{x})$ and $\kappa_{\dot{Y}\dot{Y}}(t \mid \mathbf{X} = \mathbf{x})$ on condition of the system $\mathbf{X} = \mathbf{x}$ are analytically available as follows

$$\kappa_{YY}(t \mid \mathbf{X} = \mathbf{x}) = \frac{q^2 \left(-{\omega_d}^2 + e^{2\zeta\omega t}\, {\omega_d}^2 - \omega^2\, \zeta^2 + \omega^2\, \zeta^2\, \cos(2\omega_d t) - \omega\, \omega_d\, \zeta\, \sin(2\omega_d t)\right)}{4 e^{2\zeta\omega t}\, m^2 \omega^3 \omega_d^2 \zeta} \tag{30}$$

$$\kappa_{\dot{Y}\dot{Y}}(t \mid \mathbf{X} = \mathbf{x}) = \frac{q^2 \left(-{\omega_d}^2 + e^{2\zeta\omega t}\, {\omega_d}^2 - \omega^2\, \zeta^2 + \omega^2\, \zeta^2\, \cos(2\omega_d t) + \omega\, \omega_d\, \zeta\, \sin(2\omega_d t)\right)}{4\, e^{2\zeta\omega t}\, m^2\, \omega\, {\omega_d}^2\, \zeta} \tag{31}$$

where $\omega = \sqrt{\frac{k}{m}}$, $\zeta = \frac{c}{2m\omega}$ and $\omega_d = \omega\sqrt{1-\zeta^2}$. The exact non-stationary unconditional variances presented in figures 1-8 are calculated from the numerical integration of (29) using equations (30) and (31).

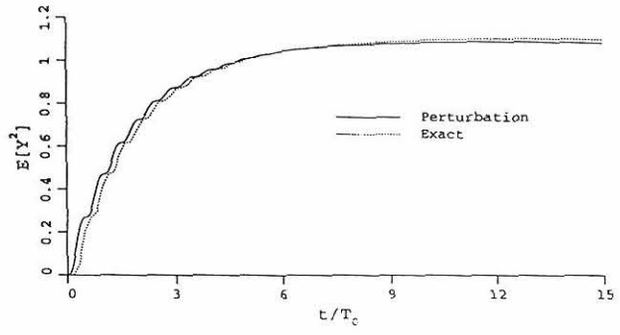

Figure 3. $\kappa_{YY}(t)$ versus $\frac{t}{T_0}$. Only C is random.

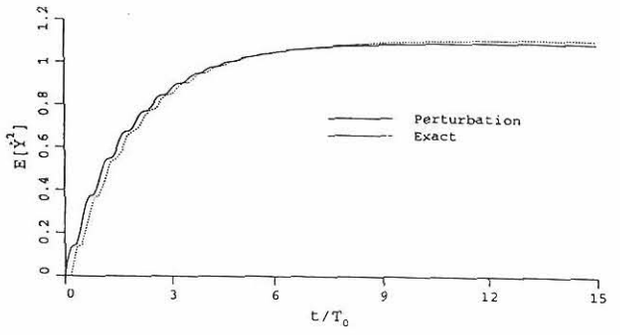

Figure 4. $\kappa_{\dot{Y}\dot{Y}}(t)$ versus $\frac{t}{T_0}$. Only C is random.

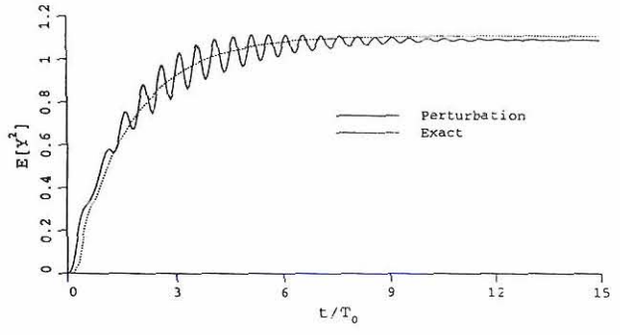

Figure 5. $\kappa_{YY}(t)$ versus $\frac{t}{T_0}$. Only K is random.

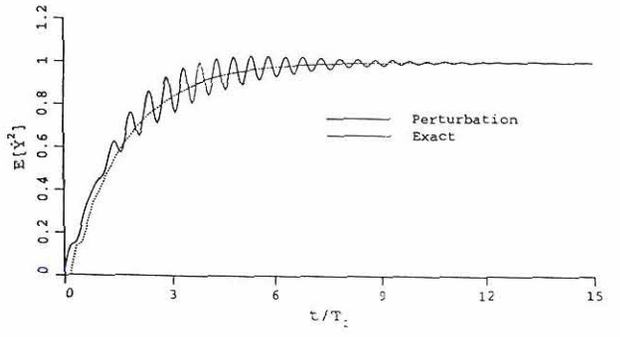

Figure 6. $\kappa_{\dot{Y}\dot{Y}}(t)$ versus $\frac{t}{T_0}$. Only K is random.

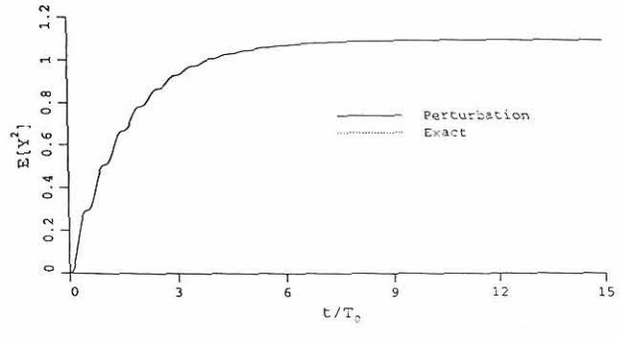

Figure 7. $\kappa_{YY}(t)$ versus $\frac{t}{T_0}$. Only Q is random.

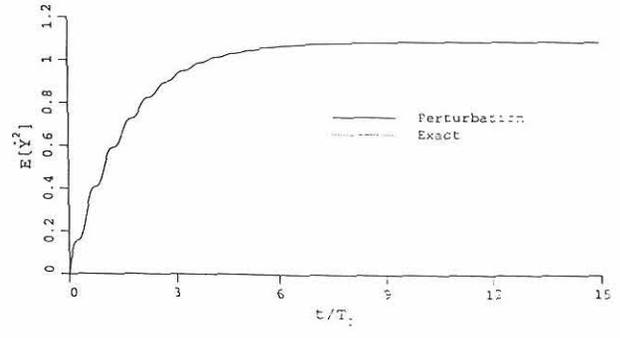

Figure 8. $\kappa_{\dot{Y}\dot{Y}}(t)$ versus $\frac{t}{T_0}$. Only Q is random.

As seen clearly from figures 1,2 and 5,6, the perturbation solution carry divergent secular terms in the non-stationary regime. Since the partial derivatives of the response processes with respect to random variables are proportional to time. To explain how these secular terms arise, a perturbation solution of order n for (30) and (31) from the mean structure can be performed. Then, terms of the types $t^n e^{-\zeta_0 \omega_0 t} \cos(w_d t)$ and $t^n e^{-\zeta_0 \omega_0 t} \sin(w_d t)$ will appear. Obviously, these terms will be dissipated as $t \to \infty$, but can be dominating at small t, especially if the damping is small. In the proposed second order perturbation method, the divergent terms are quadratic with time, t^2. Hence, extensions to higher order perturbations will not improve the solution for the non-stationary regime. The solutions would have blown up with time if there hadn't been any damping. For damped systems, since the divergent secular terms are under the governing control of the exponential damping decay, the existing deviations in the perturbation solutions become neither observable nor important at large t. Similar secular terms were previously detected by the authors in the perturbation solutions of linear oscillators with random stiffness subject to short duration earthquakes, [12]. On the other hand, for the studied example, no significant secular terms are present for only the random damping case, figures 3-4. The results are exact for only random white noise intensity case, figures 7-8. Further, the stationary results are estimated with high accuracy in all cases even for such high variabilities, $V[\cdot]$. The deviations between the perturbation results and the exact solutions in the stationary regime are due to latter's being dependent on the selected distribution (in this example, uniform distribution) whereas perturbation solutions are distribution free.

Analytical derivations yield the following exact stationary unconditional variances.

$$\kappa_{YY} = E\left[\frac{Q^2}{2CK}\right] = \frac{1}{6(b_C - a_C)(b_K - a_K)} \ln\left(\frac{b_C}{a_C}\right) \ln\left(\frac{b_K}{a_K}\right) (b_Q^2 + b_Q a_Q + a_Q^2) \quad (32)$$

$$\kappa_{\dot{Y}\dot{Y}} = E\left[\frac{Q^2}{2MC}\right] = \frac{1}{6(b_M - a_M)(b_C - a_C)} \ln\left(\frac{b_M}{a_M}\right) \ln\left(\frac{b_C}{a_C}\right) (b_Q^2 + b_Q a_Q + a_Q^2) \quad (33)$$

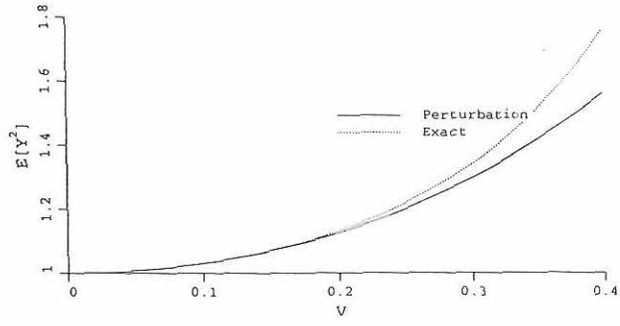

Figure 9. κ_{YY} versus V. All parameters are random with the same coefficient of variation V.

(32) is employed to illustrate the validity range of the second order perturbation solution for the stationary results in figure 9 where all random variables are given the same coefficient of variation, V. The stationary results for the perturbation solution can be obtained from the solution of linear equations listed in (20) with left hand sides equal to zero. From the comparison of exact stationary results and the second order perturbation results, it is concluded that the proposed second order perturbation method yields good results for variablities up to 25-30 per cent for stationary results.

6. CONCLUSIONS

A second order perturbation method using stochastic differential equations is developed for the stochastic response problem of linear systems with random parameters subject to random excitation modelled as white-noise multiplied by an envelope function with random parameters. The joint statistical moments entering the perturbation solution are determined by considering an augmented dynamic system with state variables made up of the displacement and velocity vector and their first and second derivatives with respect to the random parameters of the problem. Equations for partial derivatives are obtained from the partial differentiation of the equations of motion. The zero time-lag joint statistical moment equations for the augmented state vector are derived from the Itô differential formula. This provides a very compact formulation. Secular terms arise in the perturbation solution in the non-stationary phase until stationarity is attained in case of random mass and random stiffness paramaters. These are under the governing control of the structural damping of the system in the way that they are eventually dissipated.

From the studied numerical comparisons with the exact results for a random linear oscillator, it is concluded that the proposed second order perturbation method possesses secular divergent terms which are under the control of damping in the non-stationary regime and that it yields very good results for variablities up to 25-30 per cent for stationary response statistics.

7. ACKNOWLEDGEMENTS

The present research was partially supported by The Danish Technical Research Council within the research programme Dynamics of Structures.

8. REFERENCES

1. L. Arnold, *Stochastic Differential Equations: Theory and Applications*. John Wiley and Sons, 1974.

2. H. Benaroya & M. Rehak, 'Finite Element Methods in Probabilistic Structural Analysis : A Selective Review', *Appl. Mech. Rev.* 40, 201-213 (1988).

3. C. Brenner, 'Stochastic Finite Elements (Literature Review)', *Internal Working Report No. 35-91*, Institute of Engrg. Mech., University of Innsbruck, Austria, 1991

4. R.W. Clough and J. Penzien, 'Dynamics of structures', McGraw-Hill, New York, 1975.

5. C.C. Chang & H.T.Y. Yang, 'Random Vibration of Flexible Uncertain Beam Element', *J. Engrg. Mech.*, ASCE **117**, 2369-2351 (1991).

6. A. Der Kiureghian, C.C. Li & Y. Zhang, 'Recent Developments in Stochastic Finite Element', *Lecture Notes in Engineering IFIP 76, Proc. Fourth IFIG WG 7.5 Conference, Germany*, ed. R. Rackwitz & P. Thoft-Christensen, Springer-Verlag, 1991.

7. G. Deodatis,'Weighted integral Method. I: Stochastic stiffness matrix', *J. eng. mech ASCE* **117**, 1851-1864 (1991).

8. R. Ghanem & P.D. Spanos, *Stochastic Finite Elements : A Spectral Approach*, Springer-Verlag, NewYork, 1991.

9. T. Hisada & S. Nakagiri, 'Role of the Stochastic Finite Element Method in Structural Safety and Reliability', *ICOSSAR'85, 4^{th} Int. Con. Str. Safety and Reliability I* ed. I. Konishi, A.H-S. Ang and M. Shinozuka, pp. 385-394 (1985).

10. H. Jensen & W.D. Iwan , 'Response of Systems with Uncertain Parameters to Stochastic Excitation', *J. Engng. Mech. ASCE* 118 (5), 1012-1025 (1992).

11. M. Kleiber & T.D. Hien *The Stochastic Finite Element Method*, Wiley, Chichester, 1992.

12 H.U. Köylüoğlu, S.R.K. Nielsen & A.Ş. Çakmak, 'Linear Dynamic Analysis of SDOF Systems with Random Parameters subject to Earthquake Excitations', *SDEE'93, 6^{th} Int. Con. Soil Dyn. and Earthquake Engrg.,*, ed. A.Ş.Çakmak, C.A. Brebbia, 775-795 (1993).

13. H.U. Köylüoğlu and S.R.K. Nielsen,'Stochastic dynamics of linear structures with random stiffness properties and random damping subject to random loading', *Proc. 2nd European Conf. on Structural Dynamics, Eurodyn'93* ed. Moan et al.**2**, 705-711 (1993).

14. H.U. Köylüoğlu, S.R.K. Nielsen and A.Ş. Çakmak,'Stochastic dynamics of geometrically non-linear random structures subject to stationary random excitation', *Structural Reliability Theory. Paper No. 116.. ISSN 0902-7513 R9418*, University of Aalborg, Denmark, 1993 (submitted to Journal of Sound and Vibration).

15. W.K. Liu, T. Belytschko& A. Mani 'Probabilistic Finite Elements for Nonlinear Structural Dynamics', *Com. Meth. Appl. Mech. Engrg.* **56**, 61-81 (1986).

16. T. Takada, 'Weighted Integral Method in Stochastic Finite Element Analysis', *J. Prob. Engrg. Mech.* **5**, 146-156 (1990).

17. E.H. Vanmarcke, M. Shinozuka, S. Nakagiri, G. Schueller & M. Grigoriu, 'Random Fields and Stochastic Finite-Elements', *Structural Safety* **3**, 143-166 (1986).

18. E.H. Vanmarcke, 'Probabilistic Modelling of Soil Profile', *J. Geotech. Engrg. ASCE* **103**, 1227-1246 (1977).

MEASURED AND PREDICTED DYNAMIC BEHAVIOUR OF AN OFFSHORE GRAVITY PLATFORM

by

Ivar Langen, Høgskolen i Stavanger, Stavanger, Norway

EXTENDED ABSTRACT

The Gullfaks C platform which was installed in May 1989 on 217 metres water depth in the North Sea, is the largest offshore gravity base concrete structure in the world up to now. The general layout of thew platform is given in Figure 1. This huge platform is furthermore placed on a site with multilayered soft and geotechnically complex soil conditions. To obtain necessary stability and bearing capacity a new foundation solution was introduced with circular concrete skirts penetrating 22 metres into the soil and with a drainage system by which consolidation of the soil can be accelerated and controlled.

On this background a comprehensive foundation and structure monitoring system was installed including 207 sensors which measure environmental conditions, structural behaviour and foundation behaviour. The purpose of the instrumentation was both design verification and short and long term monitoring of the platform.The instrumentation system is summarized in Figure 2.

This paper discusses the measured dynamic behaviour of the platform. The foundation behaviour and special features of the instrumentation is covered in papers by Tjelta and al. [1] and Myrvoll [2]. Two subjects are emphasized: Identification of a dynamic model of the platform and a discussion of the dynamic response.

In the identification procedure both natural frequencies and mode shapes are used. These and the damping are estimated from the measurements using a multichannel ARMA model [3,4]. The first natural period is 3.01 sec and the damping ratio 1.4 - 2. The dynamic model as shown in Figure 3 is based on the design dynamic model and as built documentation. Uncertain parameters in this model as foundation spring stiffness, modulus of elasticity for concrete, deck stiffness and added mass are varied to obtain fit with the natural frequencies and mode shapes from the measurements. The identified model is furthermore compared with the design model, and predicted response obtained in the frequency domain using the model and a theoretical load model, is compared with measured response.

In the discussion of the measured dynamic response the paper features response composition, the probabilistic nature of the response, and possible nonlinearities in the soil structure interaction and wave loading. Special attention is given to observed ringing response in the platform.

As an example the wave and response spectral density in the highest seastate measured (H_s= 13.6, T_p =16.7) are shown in Figure 4. The response is mainly quasistatic. The resonance contribution to standard deviation is very small. Time series and polar plots of displacements are shown in Figure 5 and 6; both total response and response bandpass filtered at 0.25 Hz to give the wave frequency part and the resonant part. Of special interest is the resonant part which show transient

or nonstationary behaviour. The probability distributions of waves and response are presented in Figure 7. The wave frequency response is close to Gaussian indicating a linear soil structure interaction. The trendency of skewness in the waves does not show up in the response. The resonant response is clearly non Gaussian with a kurtosis value of 5.4 due to the transients. This transient resonant response also called ringing must be due to nonlinear wave loading. The mechanism is up to now not really understood and modelled. The effect does not influence the total response of Gullfaks C significantly in this sea state since resonance contributes very little.

Figure 8 shows time series of resonant response in a lower sea state (Hs = 9m, Tp = 15) where ringing is pronounced (kurtosis 10.4). These transient resonance phenomena are clearly felt by the personnel onboard and have in some cases caused uneasiness. They are, however, not important for the the integrity of the Gullfaks C structure due to the low general contribution of resonance in higher sea states. But for large volume structures with longer natural period than Gullfaks C the effect has turned out to be important [5,6.]

REFERENCES

[1] Tjelta, T.I., Janbu, N. and Grande, L., ,"Observations on Drainage Control Effects on Gullfaks C Gravity Structure", BOSS 92 International Conference on Behaviour of Offshore Structures, London, 7 - 10 July 1992

[2] Myrvoll, F.,1992,"Instrumentation of the Skirt Piled Gullfaks C Gravity Platform for Performance Monitoring", BOSS 92 International Conference on Behaviour of Offshore Structures, London, 7 - 10 July 1992

[3] Hoen, C., MARCO - A Program System for Estimation of Structural System Modal Parameters from Vibration Measurements. Theory Manual, SINTEF Report STF71 F87057, SINTEF, Trondheim, 1987

[4] Hoen, C., System Identification of Structures Excited by Stochastic Load Processes, Dr.ing. Thesis, 1991:37, Division of Marine Structures, The Norwegian Institute of Technology, Trondheim, 1991

[5] Høyere ordens lastvirkninger på bærende konstruksjoner - ringing, Norwegian Petroleum Directorate, Stavanger, December 1992

[6] Ahilan, R.V., Munthe-Kaas, Ø. and Langen, I.: "Analysis of Dynamic Transient Response (Ringing) in a Gravity Base Structure", Proc. Offshore Technology Conference, Paper No OTC 7464, Houston, 1994

[7] Langen, I og Skjåstad, O.: Gullfaks C SEM data. Identifikasjon av dynamisk modell, Statoil rapport KUP PLT 91040, Stavanger, 1993

[8] Skjåstad, O og Langen, I.: Gullfaks C SEM data. Konstruksjonsoppførsel i storm, Statoil rapport KUP PLT 91042, Stavanger, 1994

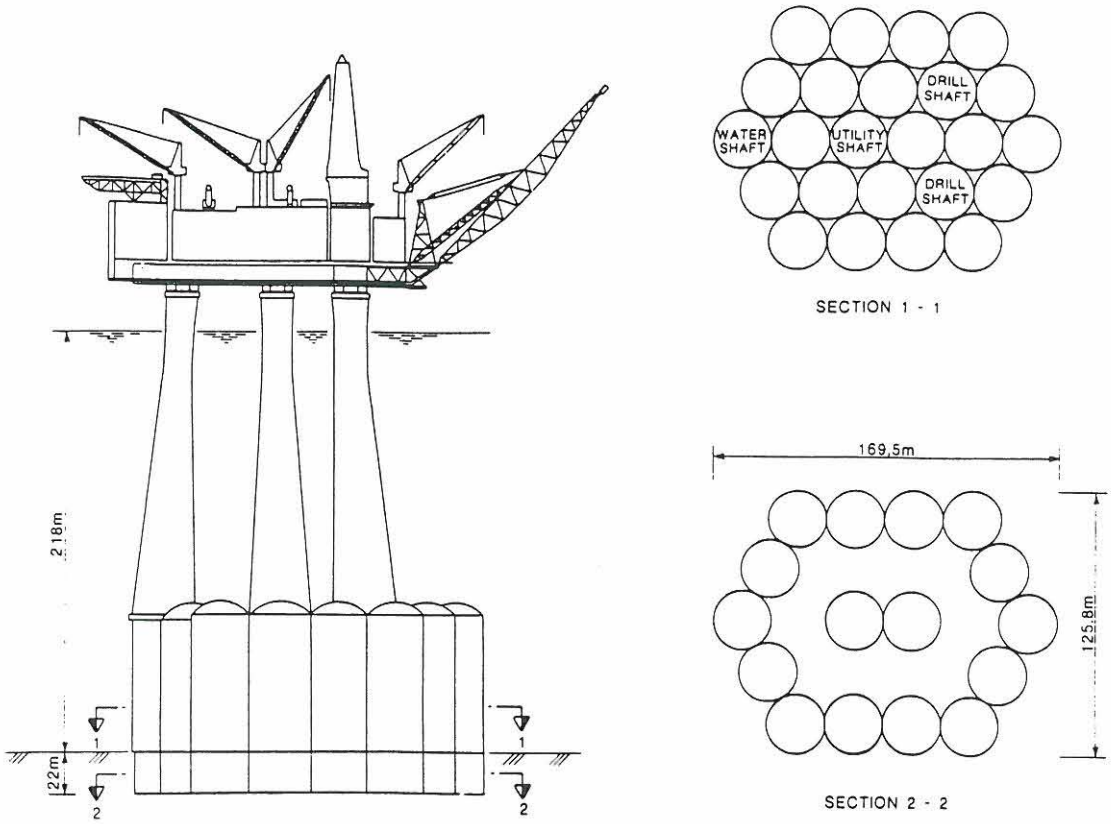

Figure 1 Platform geometry

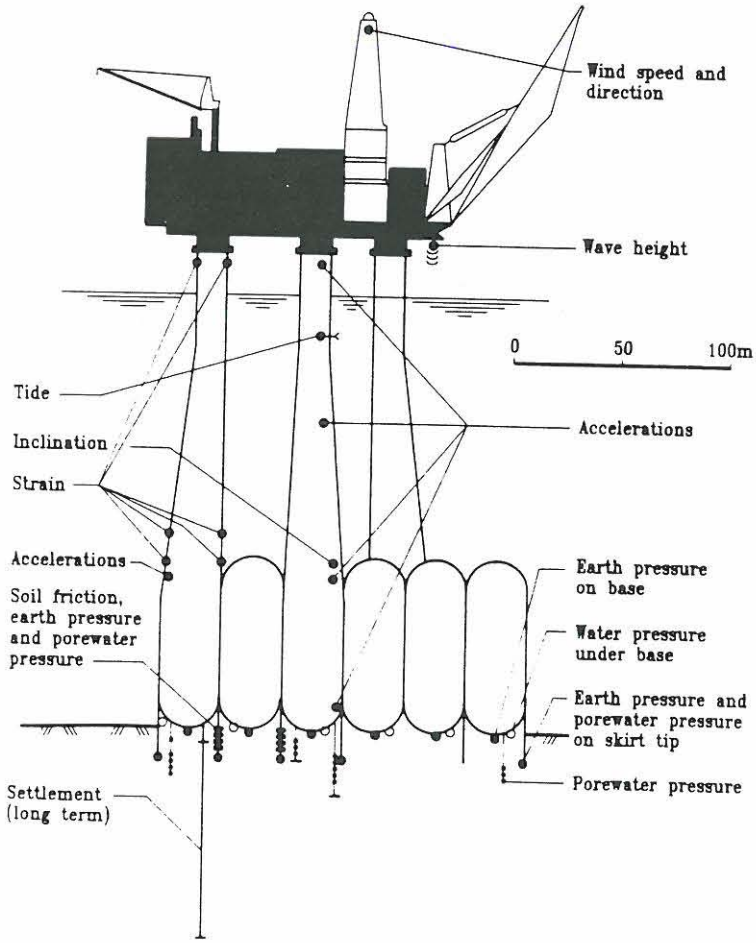

Figure 2 Instrumentation system

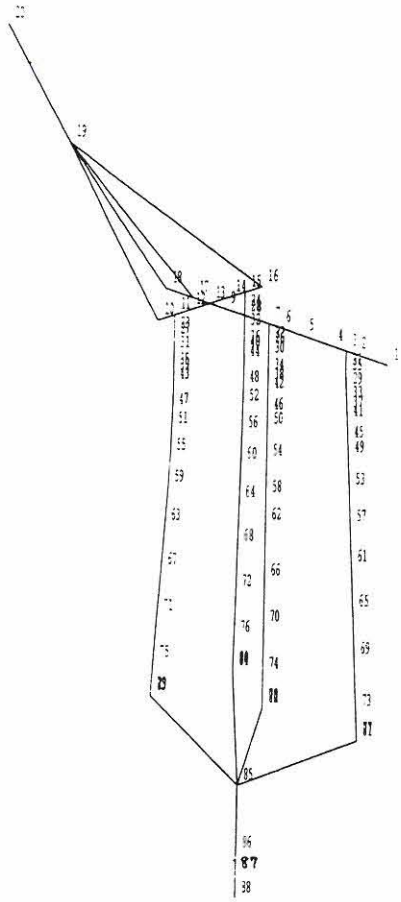

Figure 3 Frame model for dynamic analysis

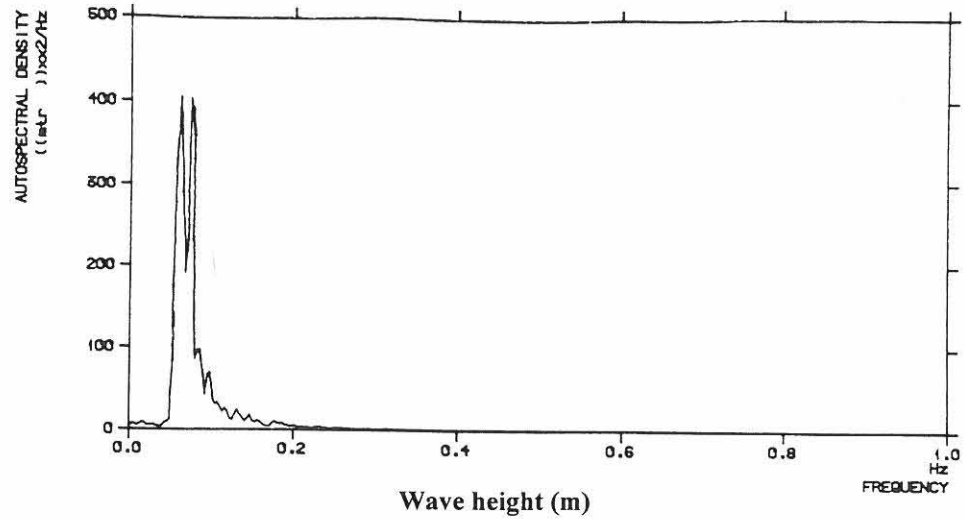

Wave height (m)

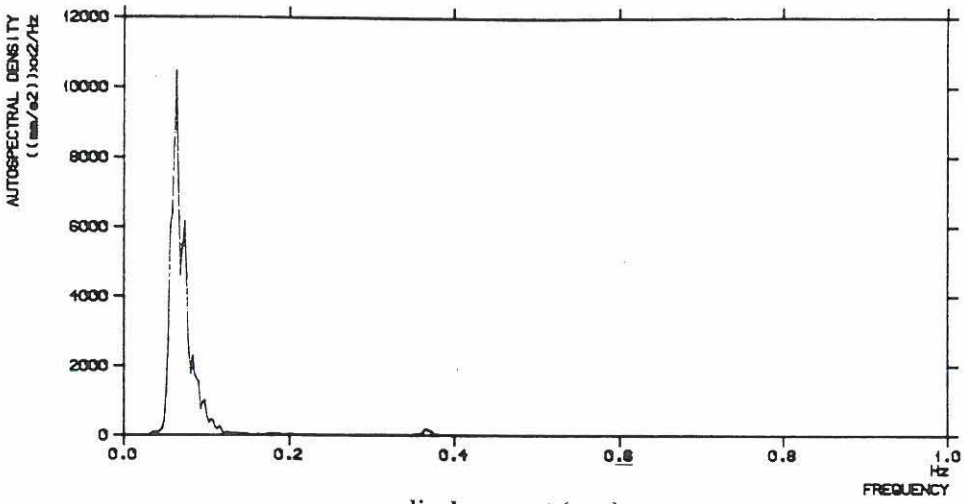

x-displacement (mm)

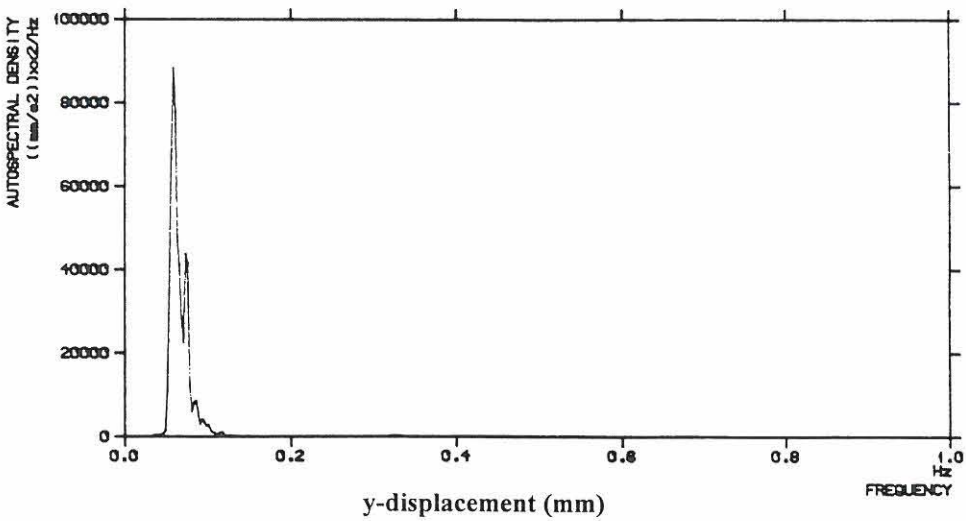

y-displacement (mm)

Figure 4 Spectral density for wave height and displacement of utility shaft. (Level 159m) Recording period 901212 09:00. H_s = 13.6 m and T_p = 16.7 sec.

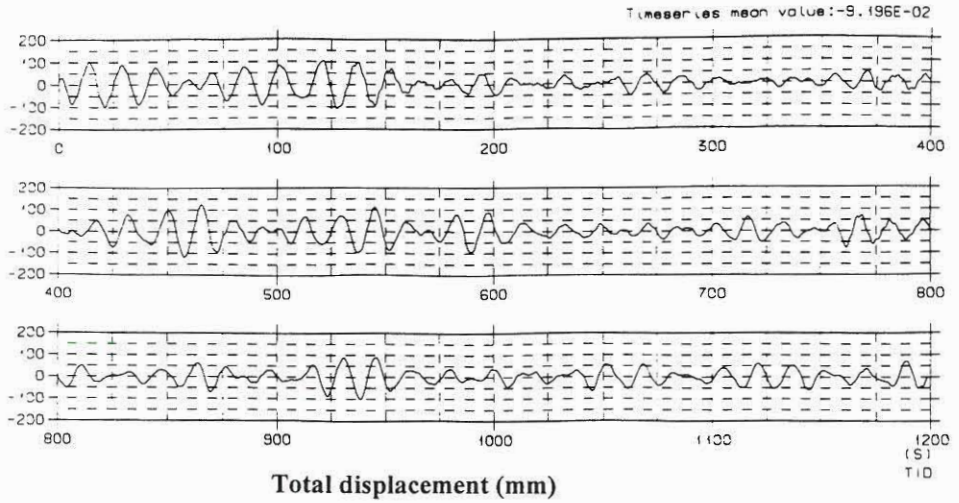

Total displacement (mm)

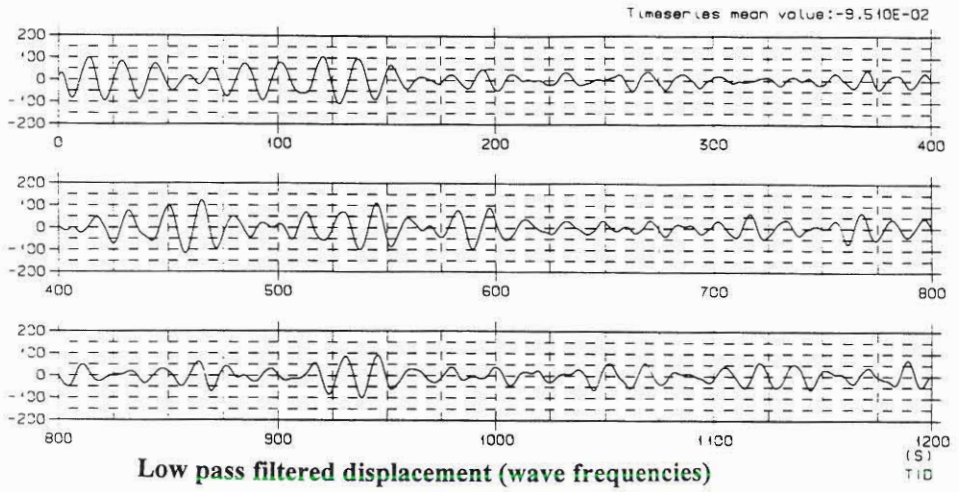

Low pass filtered displacement (wave frequencies)

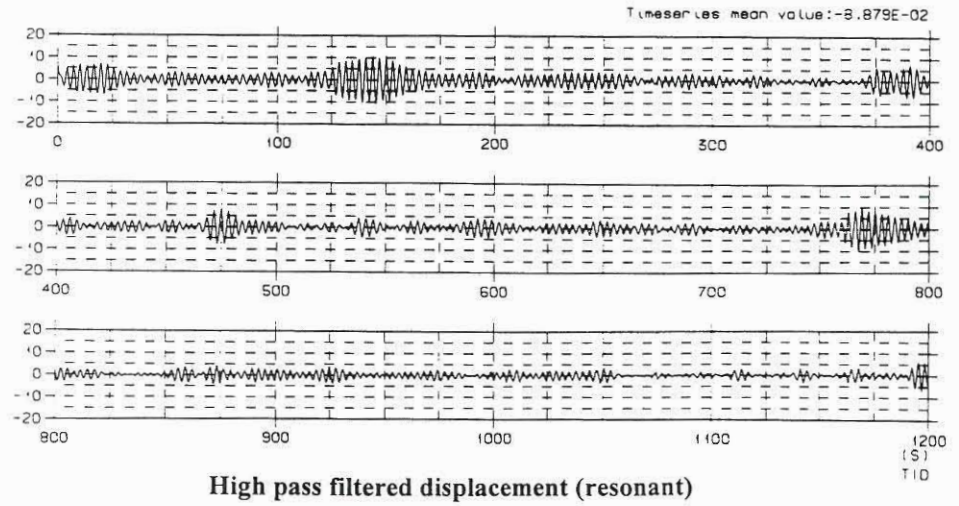

High pass filtered displacement (resonant)

Figure 5 Time series of y-displacement in utility shaft (Level 159 m) Recording period 901212 09:00. H_s = 13.6 m and T_p = 16.7 sec.

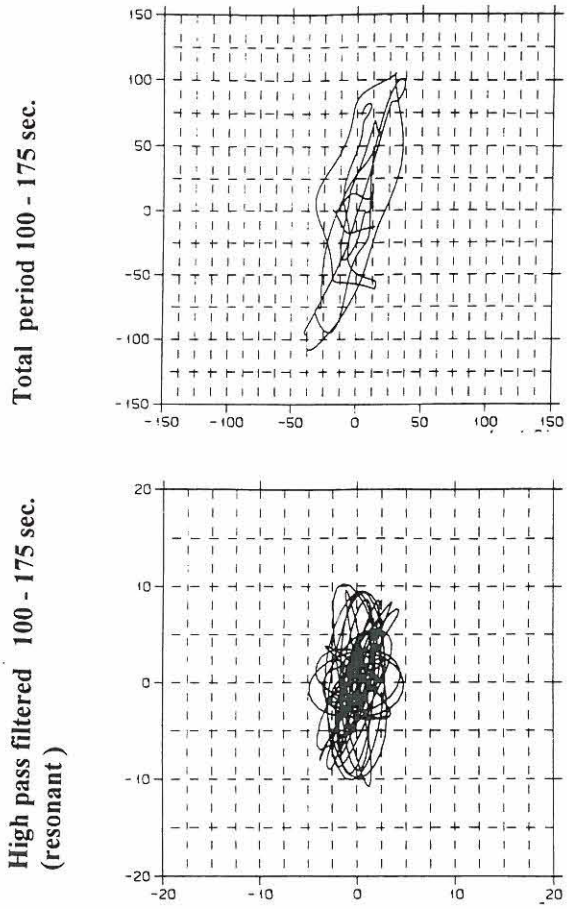

Figure 6. Displacement pattern of utility shaft (Level 159 m) Recording period 901212 09:00. H_s = 13.6 m and T_p = 16.7 sec.

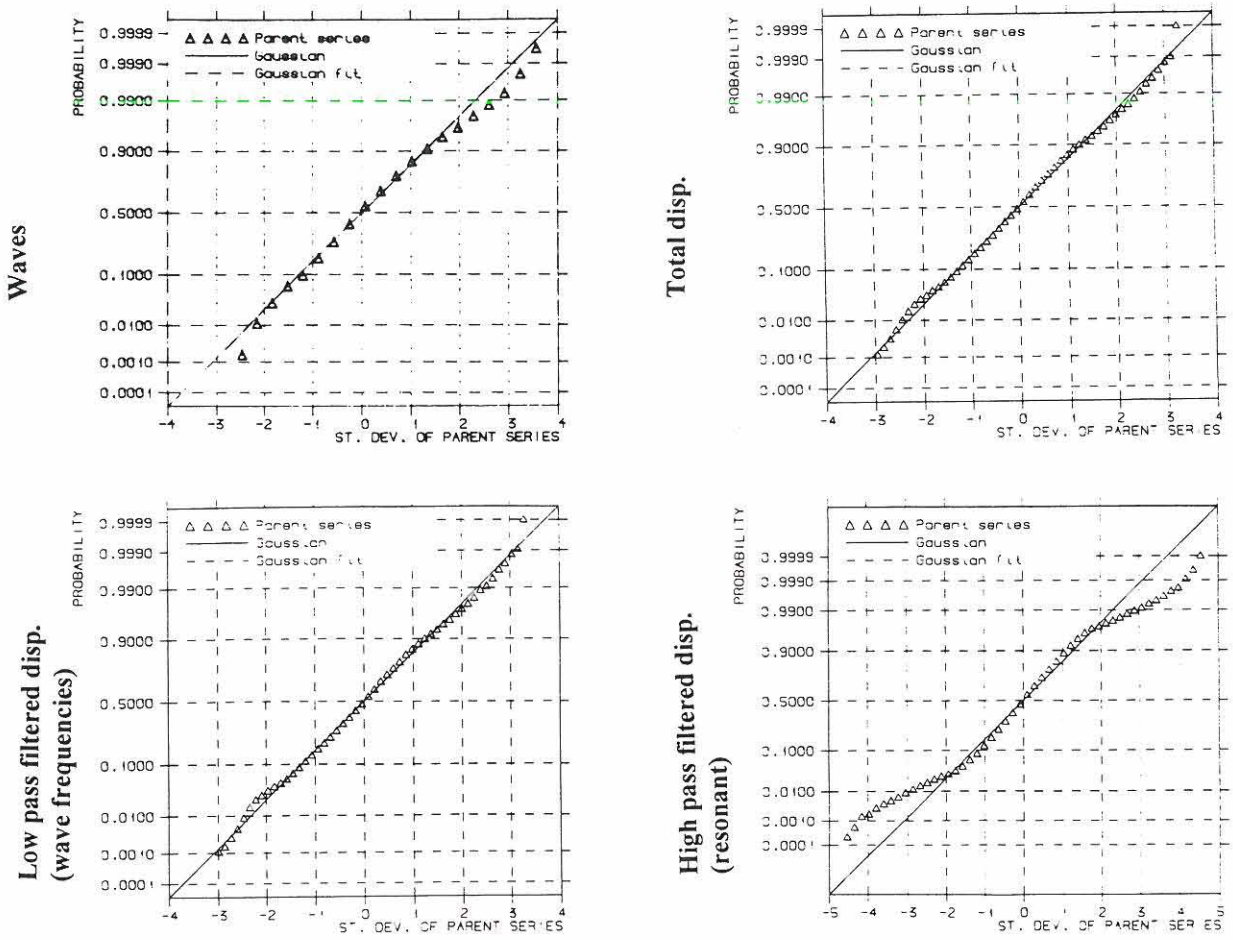

Figure 7. Probability distribution for waves and y-displacement of utility shaft (L 156m) Recording period 901212 09:00. H_s = 13.6 m and T_p = 16.7 sec.

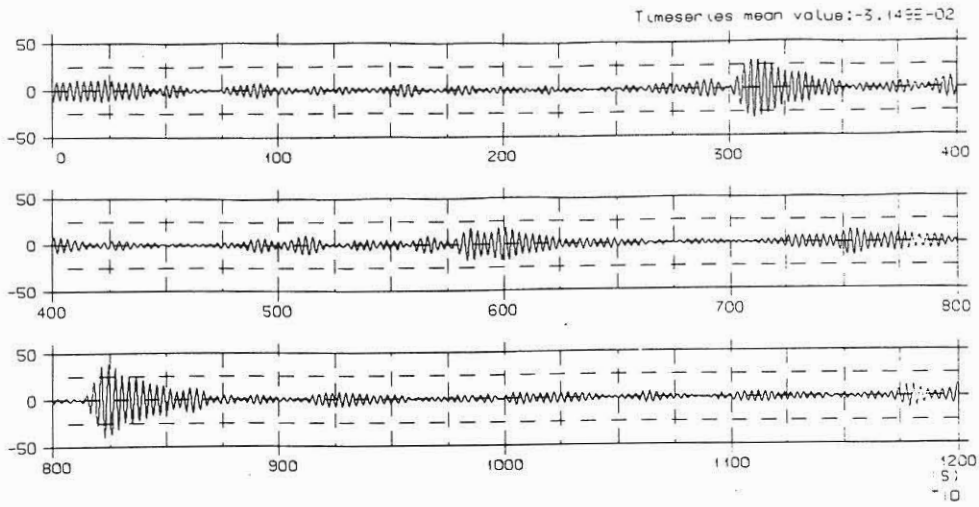

Figure 8. Time series of resonant y-displacement in top utility shaft (Level 223 m) Recording period 911018 : 0220. H_s = 9.05 m and T_p = 15.1 sec.

DYNAMIC ASPECTS OF BRIDGE PIERS WITH PLANE BASE PLATE

by
Helge Gravesen and Ole A. Madsen, Carl Bro Civil and Transportation a/s

List of contents:

Abstract:
The paper summarizes some important experienced obtained from the West Bridge in the Storebælt Link. The alternative of the Contractor (ESG) included bridge piers with a plane base of reinforced concrete instead of open bottom caissons with in-situ casting of tremie concrete. The design change gives rise to a number of special requirements.

The paper includes first a review of the major dynamic loads of importance for the bridge piers (ultimate and accidental loads). Then the requirements to and the experiences with the stonebed under the caisson bottom are reviewed. Next the consequences in terms of base plate design are reviewed. Finally, because of problem experienced with some valves in the bottom plate to be used in connection with placing the caissons on the stonebeds, the consequences for the bearing capacity of sandfilling the stonebed are reviewed.

The problems associated with the filter criteria between stone bed and soil and the consequences of sandfilling of the stonebed are the same for the alternative caissons considered.

1. Introduction

The design of the bridge piers for the West Bridge in Storebælt, Denmark, has included several alternatives from the outline design to the tender design and the contract design. During outline design several alternative superstructures including one level concrete and steel structures and two level composite structures resulted in very different bridge piers. The successful tender from ESG included a one level concrete superstructure; but it included also as a major difference, that the bridge piers were constructed as caissons with a plane base of reinforced concrete instead of open bottom caissons with in-situ casting of tremie concrete, see Fig.1.1.

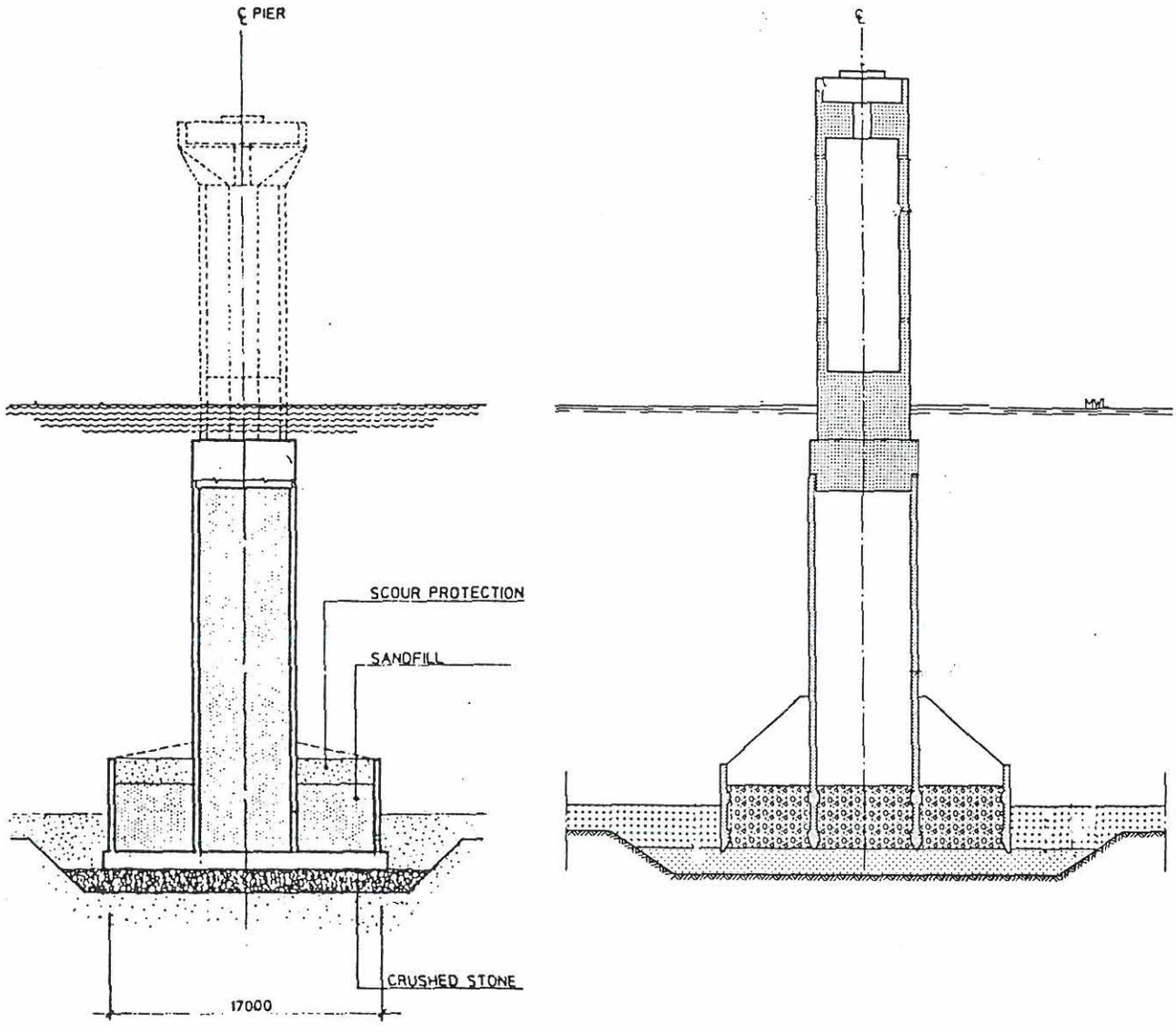

Fig 1.1 Caisson with plane base plate and open caisson with in-situ casting of tremie concrete

The present paper summarizes some of the major experiences obtained during checking the design and the installation procedures and following the installation of the pier caissons with plane base plate.

Caissons with fixed base plate placed directly on a stonebed gives rise to a number of special requirements and associated analyses, of which some appeared more critical than initially assumed. The West Bridge is today successfully installed so the problems associated with the chosen caisson concept have been overcome. But the experiences obtained are important for future alternatives including caissons with plane base plate specially when exposed to dynamic loads.

2. Load cases (waves, ice, ship impact)

The main environmental or accidental loads to the bridge piers include waves (plus current), ice, and ship impact. They are briefly described in the following as they are determining also for some special requirements due to the concept with a plane base plate.

2.1 Waves

The wave load design has been described in Gravesen (1993a).

During the project the design conditions were modified to the ones shown in Fig. 2.1:

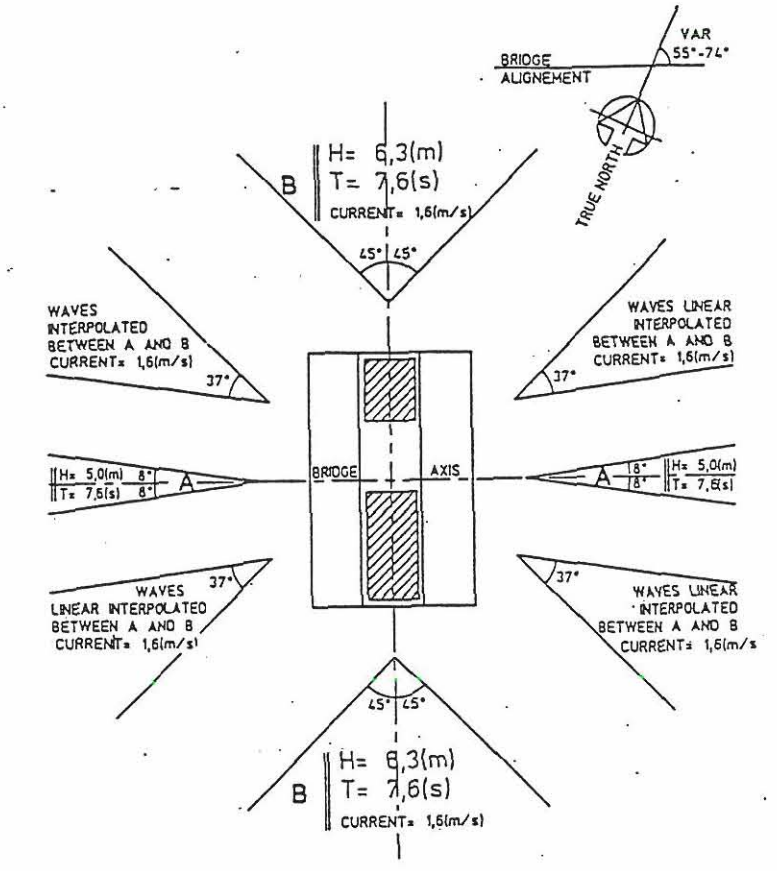

Fig 2.1 Wave load design conditions

An example of the total force design is shown in Table 2.1

CALCULATIONS No.	Pier no.	W.L. (m)	H. (m)	T. (s)	DIR. (°)	F X				M Y			
						BMT	ESG	%	Phase (°)	BMT	ESG	%	Phase (°)
A.1	44	-1,2	5	7	0°	20,4	21,4	1,05	37	319	355	1,11	37
A.2	44	-1,2	6,3	7,6	22,5°	25,6	27,0	1,05	33	380	434	1,14	33
A.3	44	-1,2	6,3	7,6	45°	18,6	19,01	1,03	33	275	300	1,09	33
A.4	44	-1,2	6,3	7,6	90°	—	—	—	—	—	—	—	—
A.5	44	-1,2	5,0	7,6	0°	22,5	—	—	32	333	—	—	32
A.6	44	-1,2	6,3	7,0	22,5°	23,0	N.A	—	38	360	N.A.	—	38
A.7	44	-1,2	6,3	7,0	90°	—	—	—	—	—	—	—	—

Table 2.1 Example of final results for pier 44 with water depth of 29 m (diffraction analysis ("BMT") plus effect of finite wave heights and pressure on the bottom of the pier added ("ESG")

2.2 Ice

The ice load design has been described in the proceedings from the seminar in Danish Society of Hydraulic Engineering on "Design of exposed bridge piers, 1. Dynamic ice load". The paper by Christensen et al (1991) describes the overall results inclusive the results of the ice model test later published in Christensen and Klinting (1992), Timco et al (1994), and Christensen et al (1994). The paper by Christensen and Skourup (1990) describes the extreme ice properties. The cyclic soil tests are described in Kleven and Andersen (1992) and the integrated soil resistance analysis is described in Andersen et al (1992). A further overall description has been given in Chistensen et al (1993).

The selected design time series are presented in Fig 2.2

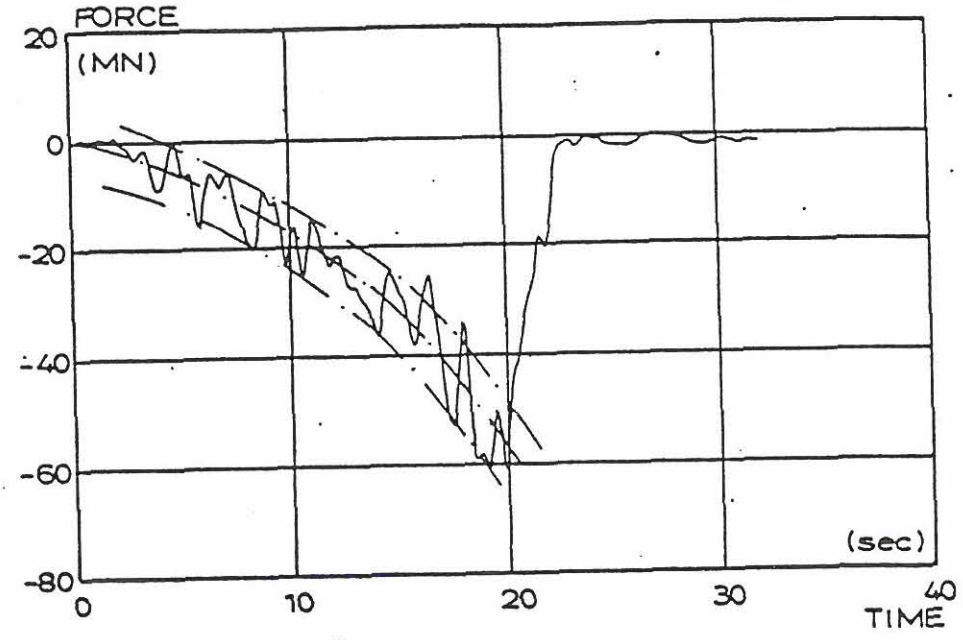

Fig 2.2 Selected design time series, accidental ice load. The indicated band envelopes load fluctuations caused by spalling. The design time series is scaled to both the desired load level and coincidence between spalling frequency and pier vibration frequency (lock-on).

The structure/soil response in terms of the sectional forces and moments at foundation level calculated by applying the complicated non-linear structure and soil are illustrated in Fig 2.3.

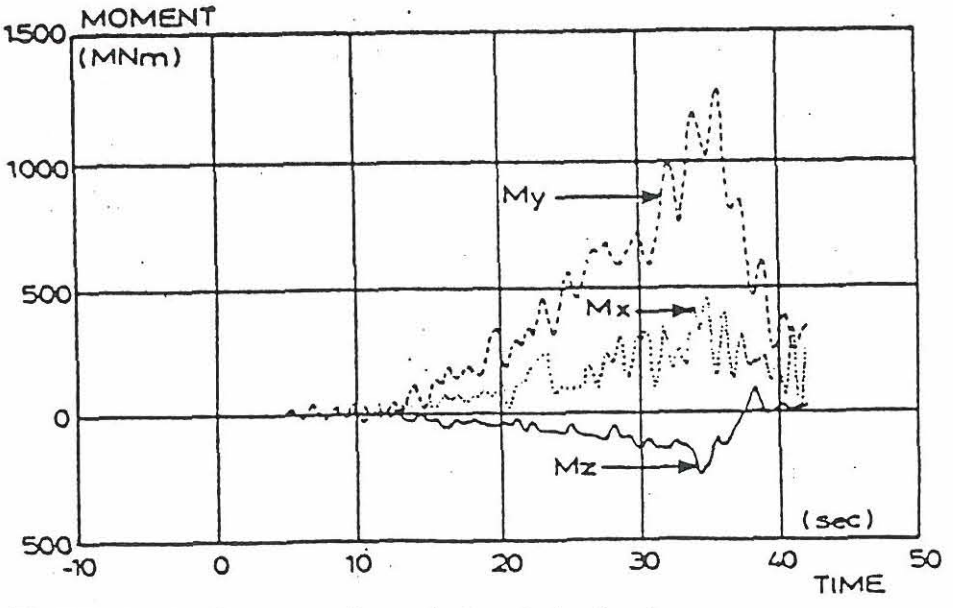

Fig 2.3 Ice load response forces in foundation level

The static design forces as specified in the contract were defined as:

F_{max} = 44 MN for an incident angle of α = 63 °, combined with a torsion moment of 220 MNm (corresponding to a torsion arm of 5 m.)

The force distribution corresponds to:

F(perpend. to bridge axis) = 20 MN
F(parall. to bridge axis) = 38 MN

The main result of the investigation was that the "real" design forces gave a slightly (few percent) larger load on the structure than the specified "equivalent static load" , but the increase could be converted to an acceptable slightly larger risk for exceedance from the ice load.

2.3 Ship impact

The ship impact investigations have been described in Gravesen (1993b).

The "real" load scenario with the selected 2,000 dwt incident ship is illustrated in Fig. 2.4 and 2.5

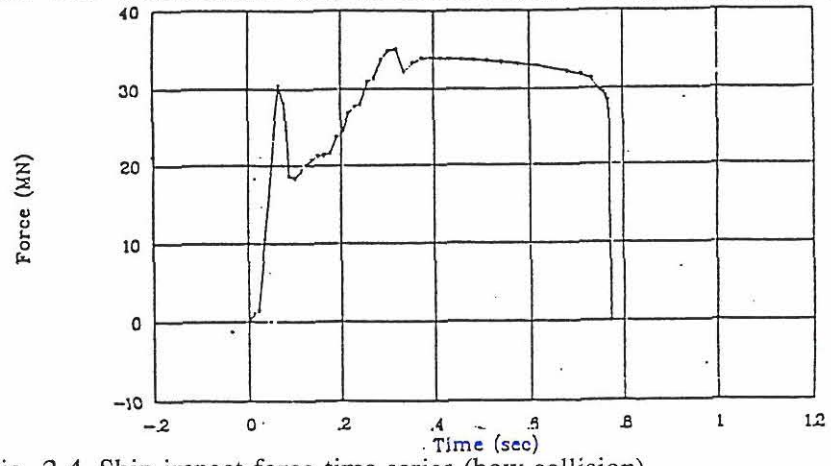

Fig. 2.4 Ship impact force time series (bow collision)

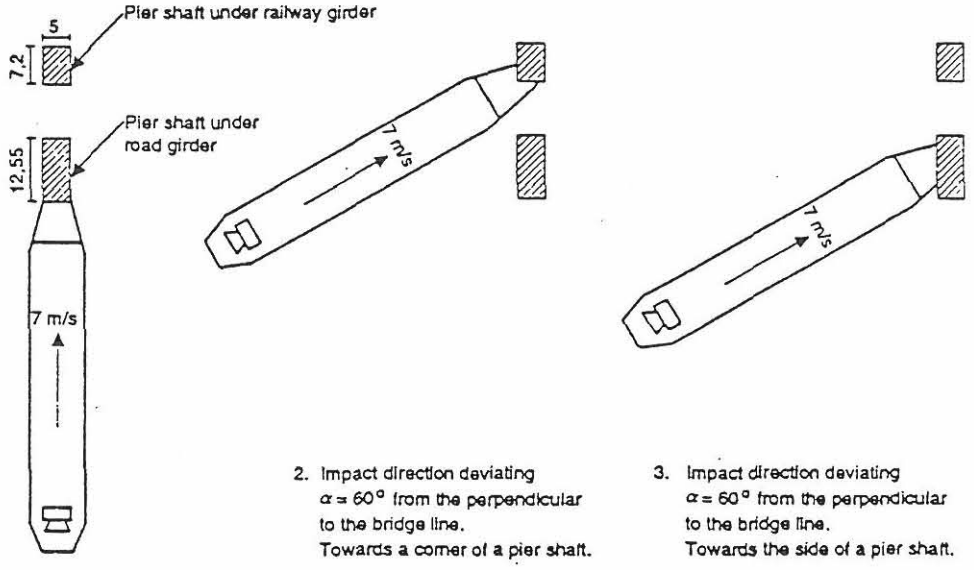

Fig 2.5 Schematic view of impact locations from bow collision

The "equivalent static design forces" in the contract were specified from the directions and at the locations shown on Figure 2.5.

The design forces and the levels of impact were

- 40 MN at level + 0.5m (for a loaded ship)
- 36 MN at level + 3.5m (for a ship in ballast)

2.4 Soil resistance model(s)

The foundations were designed in accordance with DS 415 cl. 6.1 for direct foundations and the contract was based on soils with an undrained cohesion of 225 kPa. For ship impact (short term load) the soil strength was increased by 3 times 5% corresponding to 3 decades because the impact is assumed to be 1,000 times faster than used in soil tests. Where weaker soil required larger foundation, the Contractor was paid for the additional costs for foundation and structures.

For ultimate limit state (ULS) calculations (DL + LL + wind and waves) a factor of safety of 2.0 is used, whereas for accidental limit state calculations (ALS) (DL + LL + ice or ship impact), the factor of safety is 1.0.

The assumed soil reaction distributions are described further in section 4.

2.5 Discussions

As presented above the accidental ice loads and ship impacts were in the design basis simplified to "equivalent static loads".

For the ice load an initial estimate was required, because the contract design based on ESG's alternative had not been tested for ice loads. By utilizing very comprehensive tests and analysis the final calculated accidental ice forces showed to be only few percent larger than corresponding to the estimated "equivalent static forces". However, the bridge piers could have been designed more favourable to ice forces so this load case could have been less critical.

For the ship impact it may be concluded, that it as for example in connection with the East Bridge would have been more convenient, if the "real" load in terms of force versus time had been included in the design basis.

Then the Contractors design would automatically be required to include dynamic effects like requirements to bridge bearings and a realistic foundation bearing capacity analysis including considering build-up of pore pressures, for the case when damages to ball valves in the bottom of some caissons made it required to assume sandfilling of the stonebed.

Too large simplifications in the design basis should be avoided because such simplifications may be very inconvenient for example in case of Contractor alternatives being selected, where new critical design cases not foreseen in the simplified design basis may occur. Further, special conditions experienced during construction have also shown to be inconvenient to treat within a too simplified design basis.

3. Stonebed

3.1 Requirements to stonebed

The stonebed generally with a height of 1.5 m - 1.7 m consists of a lower compacted layer with a height of typically 1.2 m crushed stones within the diameter range 5 - 70 mm (5 - 90 mm at shallow water).

On the top of this layer a 0.3 - 0.5 m screeding layer typically consisting of 70 mm heavy density stones (see section 3.4) is placed.

The lower stone bed should be compacted to a relative density of 80 % in order to ensure strength and to safeguard against shake-down in case of dynamic loads such as ice and ship impact.

3.2 Levelling of screeding layer

The fixed bed in the caissons give rise to very stringent requirements to the allowable unevenness in the final surface of the screeding layer.

The jack-up barge "Buzzard" was equipped to carry out the various required actions:

- cleaning of the surface of the excavated area
- placing of the stones in layers
- compacting the stones in the lower layer(s)
- levelling the final surface
- surveying of the surface of the excavation, the uncompacted/compacted layers, and especially of the final screeding in order to control the strict requirements

"Buzzard" capabilities are illustrated on Fig. 3.1:

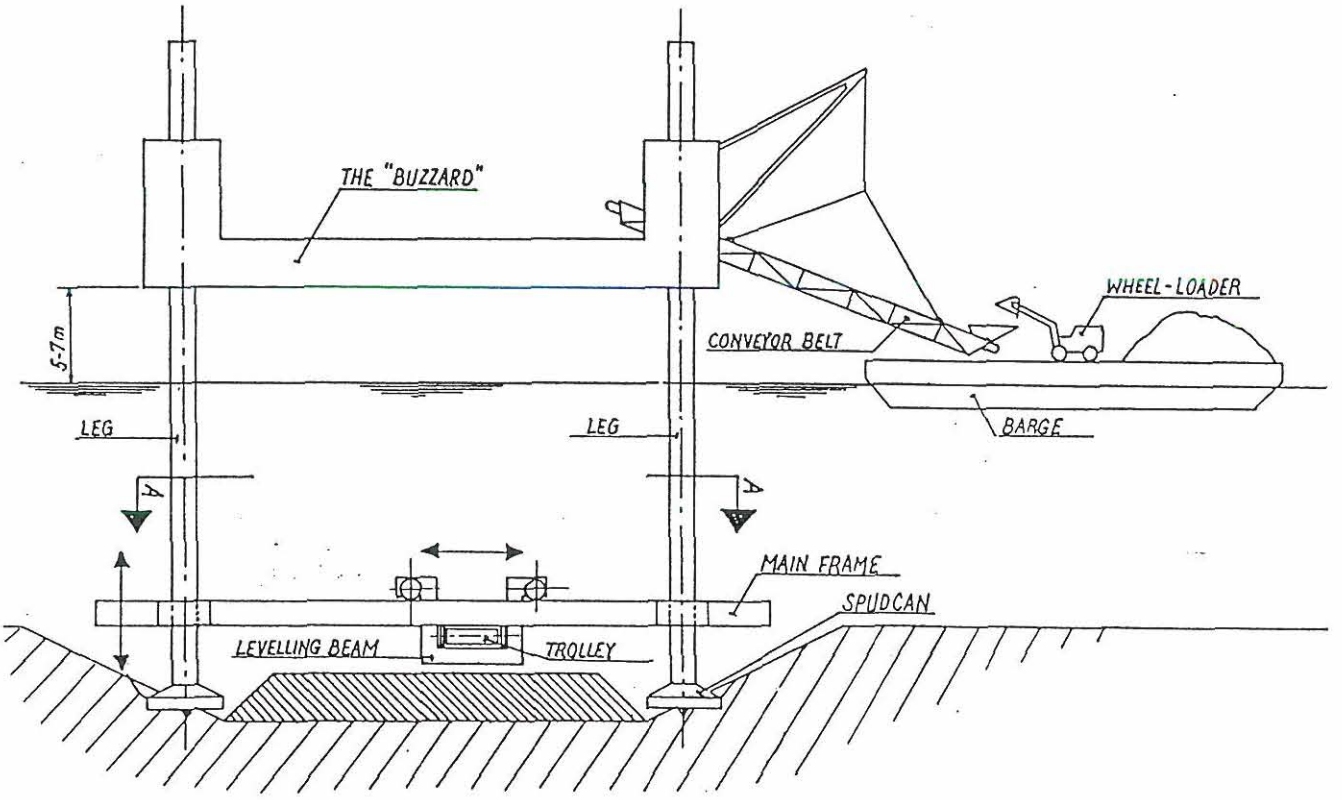

Fig 3.1 "Buzzard"

The assumed stiffness of the stone bed and the final levelling criteria are described in section 4. Tests with "Buzzard" showed, that it was possible to obtain the required evenness of the screeding layer. It may be concluded, that apparently no less advanced equipment than "Buzzard" could have been applied for the work. An unacceptable evenness of the screeding layer would have resulted in that the caissons be undergrouted so the basic idea of the "plane base plate on a stone bed without undergrouting" could have disappeared in a late stage of the project with quite drastic technical and cost consequences.

3.3 Stability of stone bed before installation of pier

An important requirement to the stone bed, on which a caisson with fixed bottom has to be placed, is that the accurately installed stonebed remains stable from the time of screeding to the time of installation. This is more critical for caissons with a plane base than for caissons to be undergrouted later.

The general scour design including the results of the scour model tests is described in Hebsgaard et al (1994).

The scour requirements in the intermediate situations were originally specified on the basis of theoretical analysis using a Shield criterion ($\theta = 0.03$). Later, some additional model tests were carried out (Delft Hydraulics, 1990) in connection the ESG's supplementary scour model tests.

The following cases were considered:

	Design conditions				Return period
	Waves dominant		Current dominant		
	H_s (m)	U_c (m/s)	H_s (m)	U_c (m/s)	
1. Screeding layer completed	2.1	1.1	1.2	1.55	1 year
2. Placing pier	< 0.7			< 1.50	
3. Pier placed	1.5	1.1	1.2	1.30	2 weeks

The review included analysis of the current amplification due to the neighbourhood of the piers and the induced currents due to vertical pier oscillations during installation.

The determining criteria showed to be case 1. "Screeding layer completed", which appeared to result in quite larger stones than initially assumed to minimize risk for damage to the evenness of the screeded layer. In order to reduce the practical problems associated with screeding of the upper stone layer emphasis was given to determine the minimum possible diameter of the stones in the screeding layer. Therefore, an upper stones layer with a relative density of 1.9 was recommended. The analysis resulted in stone diameter requirements (d_{50}) of 80 mm, 55 mm and 35 mm for water depths of 10 m, 15 m and 20 m, respectively.

Model tests with corresponding stones of usual density showed the very few stones were moved during installation, but severe damage could occur in the period after placing the caissons before the final scour protection could be installed.

3.4 Filter criteria between stonebed and underlying soils

Where the excavated sea bed consists of fine sand it was necessary to construct a filter layer between the stonebed and the fine sand bottom, because there could be risk of mixing giving settlements and reduced bearing capacity for oscillating loads from waves. For stonebeds on clay till a filter layer is not considered required.

Design principles for granular filters have been improved the recent years mainly through the dutch experiences obtained in connection with the Eastern Schelde project, see for example Graauw et al (1984).

Below is given a brief simplified order of magnitude analysis illustrating, why a filter layer is required for fine sands.

A typical oscillating wave load results in a stress variation in the sea bed below the stone bed of 86 kPa and 135 kPa, respectively for a bridge pier on 13 m and 29 m water depth. The pore pressure u is assumed to vary within the same range. Then u/γ_m is varying between 8.6 and 13.5 m.

For fine sand the hydraulic conductivity is estimated to k = 2 x 10^{-5} m/s. The sand stiffness module is estimated to D = 260 MPa. The consolidation time scale (Lambe and Whitman, 1969) is for t = 2 sec:

$T = k\ D\ t/(\gamma_m\ H^2) = 1\ m^2/H^2$, where H = soil depth

For T = 0.05 is found H = 4.5 m, which is a possible sand layer thickness. To estimate the maximum gradient is used Fig. 27.2 from Lambe and Whitman (1969):

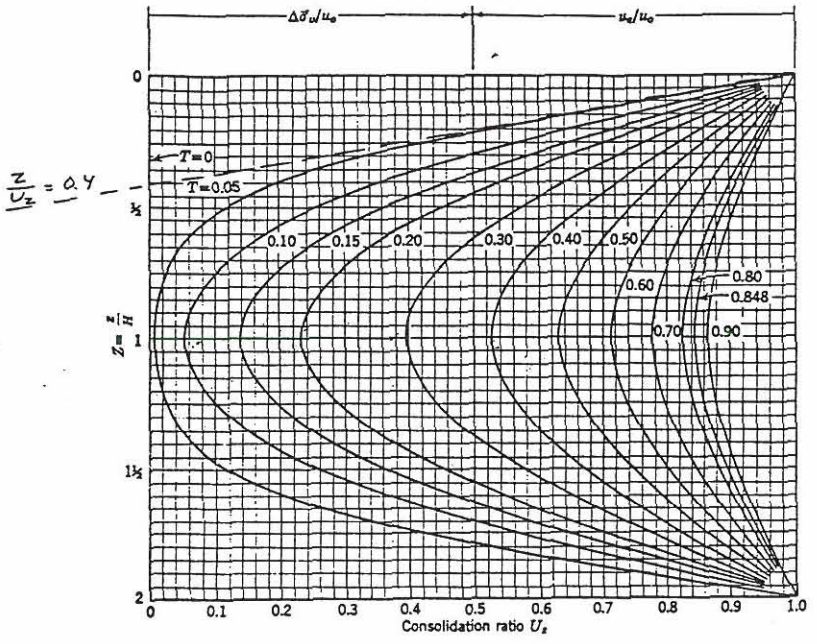

Fig. 3.2 Consolidation ratio as function of depth and time factor: uniform initial excess pore pressure.

For T = 0.05 is obtained a slope $Z/U_z = 0.4$. The maximum gradient i^{max} is estimated to

$i^{max} = (u/\gamma_m \text{ x } H)(U_z/Z) = (8.6 \text{ a'} 13.5/\ 4.5)/0.4 = 5 \text{ a'}\ 7.5 > 1$

From above simplified analysis it follows, that conditions with critical gradient (i > 1.0) may occur at the surface from the stonebed to an underlying fine sand during wave loads.

Thereby an appropriate filter (0 - 8 mm) is required between the stonebed of 5 - 70 mm stones and underlying fine sands to avoid (uneven) settlements of the stone bed under the most exposed sections of the bottom plate during wave loads. Lack of appropriate filter could in addition to uneven settlements lead to severe changes in the uniform pressure transfer from the stonebed and associated larger cracks in the bottom plate than those originally obtained through the accurate levelling.

4. Base plate design

4.1 General

The plane base plates are designed and constructed as integral elements of the bridge piers. They are designed according to the theory of elasticity, so they can transfer all forces from the bridge to the foundations.

4.2 Loads from the bridge plus waves, ice, and ship impact.

For a concrete bridge as the West Bridge, the dead load (DL) is by far the dominating vertical load on the foundation. However, the foundation and base plate dimensions are calculated based on combinations of horizontal and vertical loads, because the horizontal components moves the centre of gravity and reduces the contact area as well as the allowed vertical bearing capacity.

For a typical pier on deep water, loads and foundation stresses are listed in table 4.1.

Load case dominated by	Effective foundation surface m^2	Vertical normal stress kPa	Horizontal shear stress kPa
110% DL	569	520	17
Wave & Current	523	500	61
Ice	305	750	207
Ship Impact	340	680	223

Table 4.1 Pier no 31 on 28.5 m of water depth and with base plate dimensions 33.0 m by 21.0 m

For this pier ice forces are governing, but it should be noted, that for other piers the internal "ranking" is different.

Because of variation in pier types, water depths, soil strengths and the different safety factors on different load cases all four load combinations mentioned above are decisive for base plate dimensioning of some piers.

Load case dominated by	Decisive for base plate dimensioning of approximately below indicated number of piers
110% DL	11-12
Wave & Current	15-30
Ice	6-20
Ship impact	16-20

Table 4.2 Decisive load case for base plate area

The numbers in the table indicate that sometimes the dimensions are limited by more than one load combination and also that "relaxing" of one of the criteria would automatically make another load case decisive without any significant saving.

4.3 Foundation reaction pattern

According to the contract, the pier structure should be designed for foundation reaction according to DS 415 for cast in-situ footing foundations.

This include:

- Effective area reaction
- Linear varying reaction
- Reaction pattern according to DS 415 cl 6.1.2.1 giving + 50% under the corner sections and - 50% under the central part of the base.

Other requirements to the strength of the pier structure were:

- A "local" block load of 1200 kPa over a 3x3 m area assuming a local heap of gravel
- Compatibility requirement demanding that the base and the structure shall be designed for the actual reactions from the gravel pad as constructed.

4.4 Stonebed, construction tolerances

During the design and construction process, the Contractor decided to prepare his construction specifications including screeding tolerances and compaction quantities so that the compatibility requirement mentioned above would never lead to more adverse sectional forces in the bridge piers than the other four foundation reaction pattern requirements.

In fact, this approach was also necessary, because at that time some of the bridge pier caissons were already constructed.

The contractor verified the foundation reaction pattern for selected piers by means of the computer programme PLAXIS.

In the calculations he used the deformation parameters from the soil investigations and the subgrade reaction moduli of the compacted/uncompacted gravel pad were established based on plate load tests at Lindholm.

For a gravel pad of 1.2 m compacted and 0.3 m uncompacted stone, the PLAXIS investigations proved that calculated reaction pattern could be held within the limits when the screeding was conducted to very strict limits characterized a.o. by

- Plane or parabolic shape with maximum (average) deviation of a 3x3 m zone of 25 mm.
- Global "sag" of the parabolic shape to be less than 50 mm down in the centre and never upwards.
- One corner maximum 15 mm out of plane defined by the three other corners (to minimize twist load)

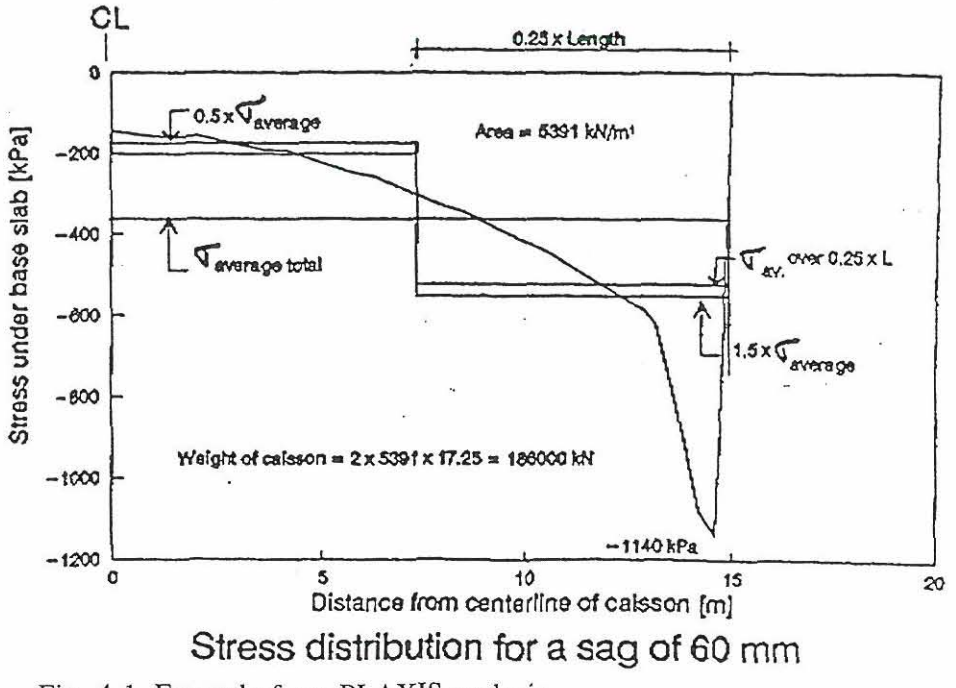

Fig. 4.1 Example from PLAXIS analysis

4.5 Structural consequences of the foundation reaction patterns

The close review of the design resulted in rather large reinforcement demands in the base plate and the lower crosswalls in the pier caissons. Stringent stress/crack criteria was a main reason that the first caissons with low slender crosswalls on a thick base plate needed considerable strengthening compared with the first estimates.

Apparently the initial serious underestimates of required reinforcement was the result of much too simplified structural analysis disregarding relative stiffness of the structural elements and the fact that the moments are transferred from walls to plates and visa versa.

Later the base plates of the piers were prestressed in the transversal directions and the crosswalls were given adequate height so that a "harmonic" structural concept was achieved.

5. Sandfilling the stonebed

5.1 Open ball valves

In order to provide an easy water filling of the bridge piers during placement and in addition close during sand filling the piers of the West Bridge were provided with 6 ball valves consisting of concrete balls fixed with steel chains in the bottom of the caissons.

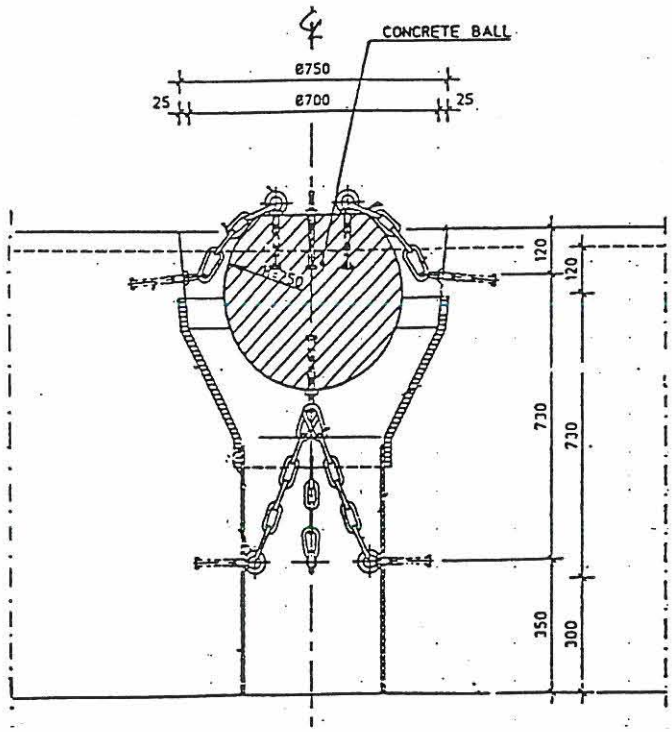

Fig. 5.1 Ball valves, original design

The ball valves were not tested before use. As a consequence of severe vortex shedding, damages occurred to the valves. Then appropriate closure from leaking sand was not obtained as openings were found due to chain elements between the ball and the cone or the ball been turned so eyebolt been present between the ball and the cone. Further, this was first experienced after 20 caissons was placed.

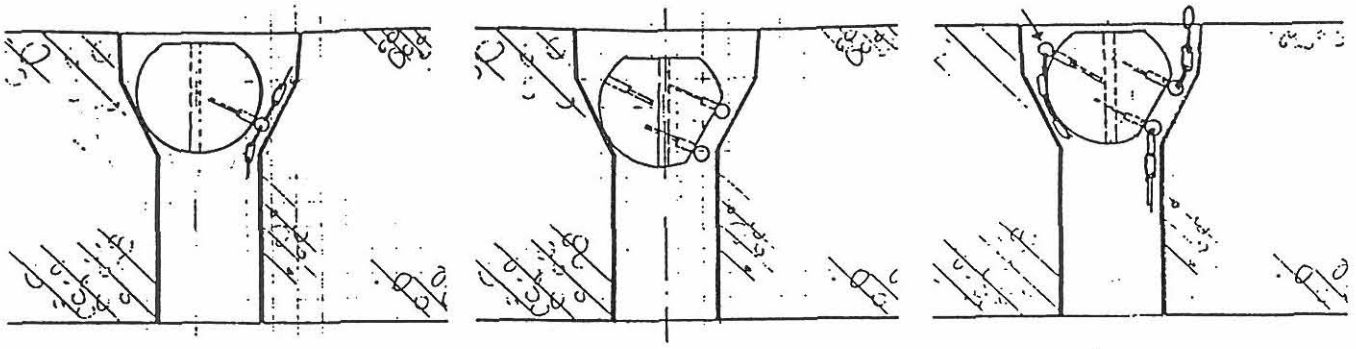

Fig. 5.2 Sketches of damages to ball valves

Due to lack of access the actual number of cases with (partly) open ball valves could not be verified so for these caissons an unpredictable number of caissons have partly open ball valves. This led to the following serious questions:

- would sandfill flow out and how large sand cone could develop below each of the open ball valves?
- could the flow pattern and the wave load distribute the sand so nearly the complete stonebed could be sandfilled?
- what is bearing capacity of a sand filled stonebed?

These aspects and main results of the quite extensive tests specified by prof S. Bernander carried out by Skanska Teknik AB on Chalmers Technical University (Gothenborg) are described in the following.

5.2 Sand cone development

Initial tests showed that it could not be proved that sand would stop falling out from partly open valves after some time with "bridging".

The Contractor initiated model test (ESG, 1993a) to estimate how much sand would probably fall out and which configuration would the outfaling sand develop.

Loading condition was an oscillating pressure gradient from the waves plus an asymmetrical constant superimposed pressure gradient caused partly by the current and the non-linearities in the waves.

Fig. 5.3 shows a result from such a test

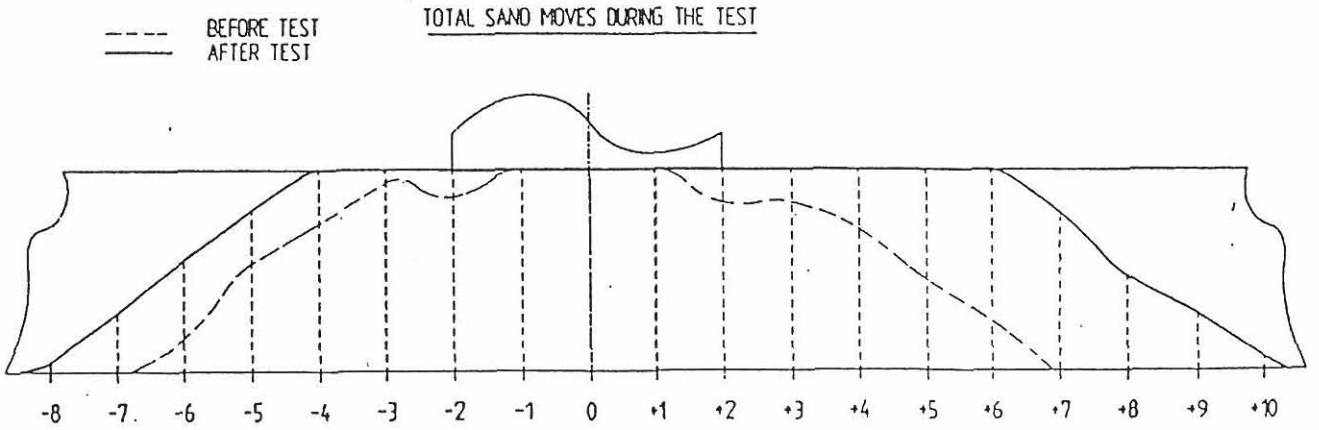

Fig. 5.3 Results from a sand filling test

It is remarkable, that a relative large cone develops, and that the growth of the cone is reduced after a certain period of time. But there always seems to remain an open slot above the sand cone, so at least the possibility of further extension of the cone is not out of question. The cone size is further quite sensitive to the asymmetry in the load scenario.

In addition to this comes, that wave loading to the sand filled cones could generate flow conditions in the sand cone with critical gradient on the cone surface, so an unpredictable additional mechanism to further spread the outflowing sand and not included in the model tests was present.

A/S Storebæltsforbindelsen and their Consultants (CCL and specialists) were of the opinion that nearly complete sandfilling was a possible scenario with potential adverse consequences.

5.3 Pore pressures in sandfilled stonebed

This led to further tests (ESG, 1993b) to measure the permeability and to measure, if the stone bed included contractive or a diletative characteristics under dynamic loadings.

If diletative characteristics were present, then no excessive pore pressure would occur under the loadings so same bearing capacity of the caissons as originally assumed was present. Visa versa if contractive characteristics were present. The most critical case was due to the short loading time considered to be ship impact (bow collision direct to a pier).

Due to the size of the stonebed materials this required quite large and complicated model tests. The permeability test were carried out in a 550 mm high ø 500 mm cylinder. Shear tests were made in a shear box with a height of 500 mm and a diameter of 1,000 mm. The shear box included 7 free ring cylinders in addition to the 2 rings attached to the top and the bottom Between the rings a 5 mm gab was maintained to avoid skin friction.

The shear box model is illustrated on Fig. 5.4:

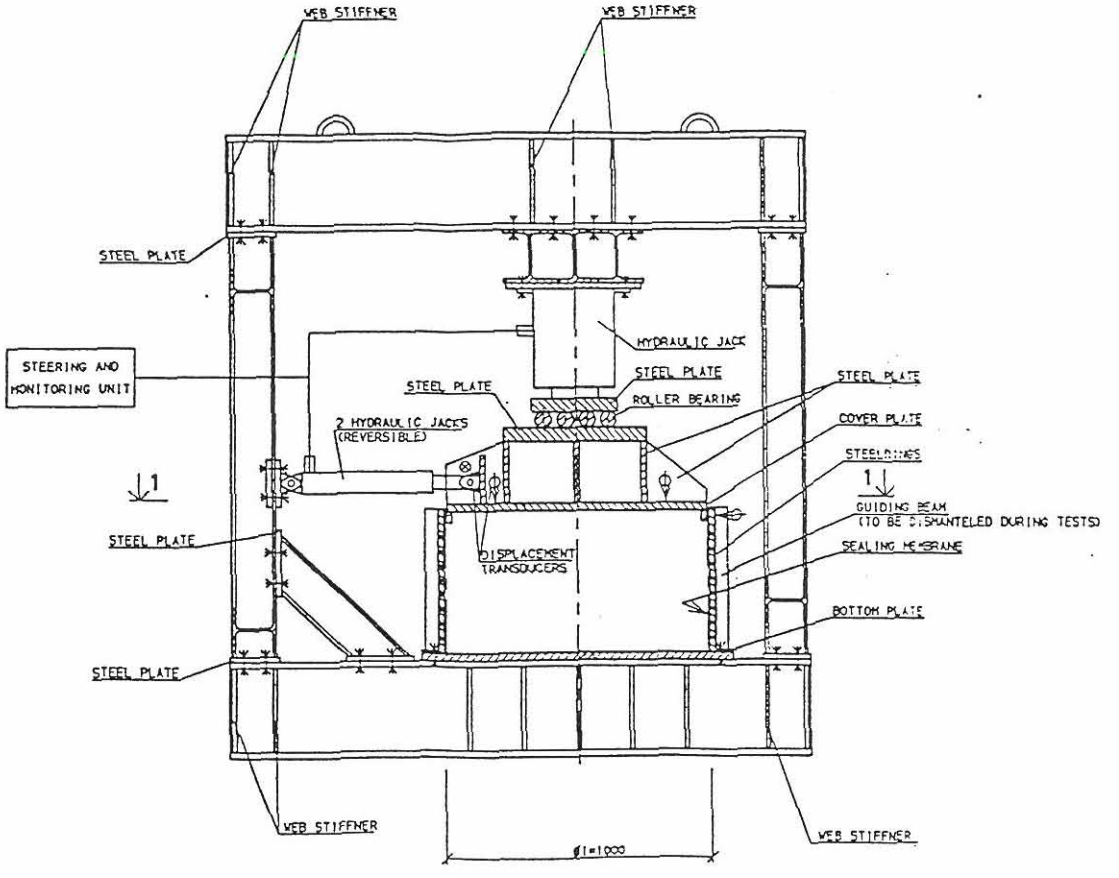

Fig. 5.4 Shear box model

The permeability tests showed some tendency to piping in certain preferential flow channels; but the results could not be interpretated so clear, that undrained conditions in certain critical area in a sandfillled stonebed could not be disregarded.

Due to uneven stress conditions in various sections of the test cylinder, shear box tests are difficult to obtain unambiguous results from. However, certain overall conclusions could be drawn from the average results:

Contrary to the Contractor's expectations, the sand filled stonebed showed to be contracting so a positive pore pressure was existing for an effective vertical stress from 380 to 700 kPa combined with a shear stress from 0 to 220 kPa and also for a maintained effective vertical stress of 380 kPa combined with a shear stress ranging from 0 to 220 kPa. In other words a negative conclusion was also a result of the shear-box tests. But as a sub-result the shear box test showed a friction between the base plate and the stonebed of 0.8 instead of 0.6 previously assumed.

From this followed that sufficient bearing capacity would occur even under undrained conditions in the stonebed (no pore pressure drainage). On the basis of negative results from all the investigations except from the sub-results with friction it still could be concluded, that sufficient bearing capacity exist even with leaking ball valves.

A complicated and expensive closing of all the possible leaking ball valves could be avoided.

5.4 Risk of sandfilling from outside

From a retrospective point of view it has to be agreed that at some areas in Storebælt it cannot completely be disregarded that there exist a risk for that a certain sandfilling may take place from bed load transport during certain wave/current situations. The current concentration and the vortex shedding caused by the presence of the structure (see Hebsgaard et al, 1994) may counteract siltation close to the piers. But even though the possibility cannot complete be disregarded.

With the positive conclusion above there appears no need for a further analysis in connection with the West Bridge prtoject. But for future project the aspect should be included in the investigations.

6. Acknowledgements

Several engineers and scientists from the contractor ESG, Storebæltsforbindelsen (SBF), and SBF's consultant, CCL, have given valuable contributions to the design and construction of the bridge piers with plane base in the West Bridge.

But we would like to emphasize the contibutions from our colleague from Cowisonsult, P. Sandgaard Kristensen, who has been a key person in all design aspects within soils and foundation for the West Bridge. In addition it should also be emphasized, that Jørgen Fredsøe (ISVA, DTU) and Jørgen Stenfeldt (DGI) have contributed to the analyses of the various problems associated with sandfilling of the stonebed from damaged ball valves.

7. References

/1/ Hebsgaard, M. , Ennemark, F. , Spangenberg, S. , Fredsøe, J., and Gravesen, H. (1994): Scour model tests with bridge piers, PIANC, Bull. no. 82 - 84, june 1994.

/2/ Delft Hydraulics (1990): Storebælt West Bridge, Scour protection, report prepared for European Storebælt Group

/3/ Graauw, A. F. de, Meulen, T. v.d.,and Does de Bye, M. R. v.d. (1984): Granular filters: Design criteria, ASCE, Journ. Waterways, Ports, Coastal, and Ocean Engng.,Vol 110. No. 1, Febr. 1984.

/4/ Lambe, T. W., and Whitman, R. V. (1969): Soil mechanics, J. Wiley & Sons.

/5/ ESG (1993a): Tech. note on ball valves in caissons with open valves. Report from 3-D tests (with sandfilling)

/6/ ESG (1993b): Ball valves in connection with open valves. Testing methods and results of tests with permeability and shear tests.

/7/ Gravesen, H. (1993a): Wave forces on bridge piers. Seminar on design of exposed bridge piers. 2. Scour, waves and ship impact. Danish Society of Hydraulic Engng. Published dec. 1993.

/8/ Gravesen, H. (1993b): Modelling of ship impact on bridge piers and on bridge girders. Seminar on design of exposed bridge piers. 2. Scour, waves and ship impact. ,Danish Society of Hydraulic Engng. Published dec. 1993.

/9/ Christensen, F. T., Gravesen, H., Thomsen, J. R., Ennemark, F., and Spangenberg, S. (1991): Accidental limit state loads on bridge piers, PIANC Bulletin 1991 no 72.

/10/ Kleven, A. and Andersen K. H. (1992): Cyclic laboratory tests on Storebaelt clay. Seminar on design of exposed bridge piers. 1. Dynamic ice load. ,Danish Society of Hydraulic Engng. Published 1992.

/11/ Andersen, K. H., Hansteen, O. E., and Gutierrez, M. (1992): Bearing capacity, displacements, stiffness and hysteretic damping of Storebælt bridge piers under ice cloading-. Seminar on design of exposed bridge piers. 1. Dynamic ice load. ,Danish Society of Hydraulic Engng. Published 1992.

/12/ Christensen, F. T., and Skourup, J. (1990): Extreme ice properties, ASCE, Journ. Cold Region Engng.

/13/ Christensen, F. T., and Klinting, P. (1992): Ice load tests on bridge pier at two different model scales, ASCE, Journ. Cold Region Engng., Vol 6, No. 3, sept 1992, pp 93 - 110.

/14/ Timco, G. W., Nwogu, O. G., and Christensen, F. T. (1994): Compliant model tests with the Great Belt West Bridge pier in ice, Part 1: Test methods and key results. Cold Regions Science and Technology, Elsevier. In press.

/15/ Christensen, F. T., Timco, G. W., and Nwogu, O. G. (1994): Compliant model tests with the Great Belt West Bridge piers in ice, Part 2: Analyses of results, Cold Region Science and Technology, Elsevier. In press.

/16/ Christensen, F.T., Gravesen, H., Kristensen, P.S., and Thomsen, J.R. (1993): Geotechnical design of Denmark's Great Belt West Bridge for dynamic loading, 4th Canadian Marine Geotechnical Conf. St. John's Canada.

Man-Induced Vibrations

J. Jönsson and L. Pilegaard Hansen
Department of Building Technology and Structural Engineering,
Aalborg University, Sohngaardsholmsvej 57, 9000 Aalborg, Denmark

Introduction

Human motion can cause various types of periodic or transient dynamic loads. The periodic loads are mainly due to jumping, running, dancing, walking and body rocking. Transient loads primarily result from single impulse loads, such as jumping and falling from elevated positions. The response to these loads are of primary interest for the structural engineer, whereas the exact load as a function of time generally is of minor importance. This is true when the loading time (contact duration) t_p is small compared to the largest natural periods $T_n = 2\pi/\omega_n$ of the structure. The present study is mainly concerned with spectator-induced vertical vibrations on grandstands. The idea is to use impulse response analysis and base the load description on the load impulse. If the method is feasable, it could be used in connection with the formulation of requirements in building codes.

During the last two decades work has been done on the measurement of the exact load functions and related reponse analysis. A recent work using a spectral description has been performed by Per-Erik Erikson [9] and includes a good literature survey. Bachmann and Ammann [1] give a good overview of vibrations caused by human activity. Other relevante references have been included in the reference list.

Periodic motion

The forces acting on a human body performing periodic motion can be decomposed in several ways. In this section the vertical motion is considered. A body shown in figure 1 (left) with mass m is acted upon by a gravitation force $F_g = mg$, a constant reaction force $F_c = \gamma mg$ and a dynamic force F_d. The constant reaction force F_c exists, if the body is in continous contact with a structure and it is the

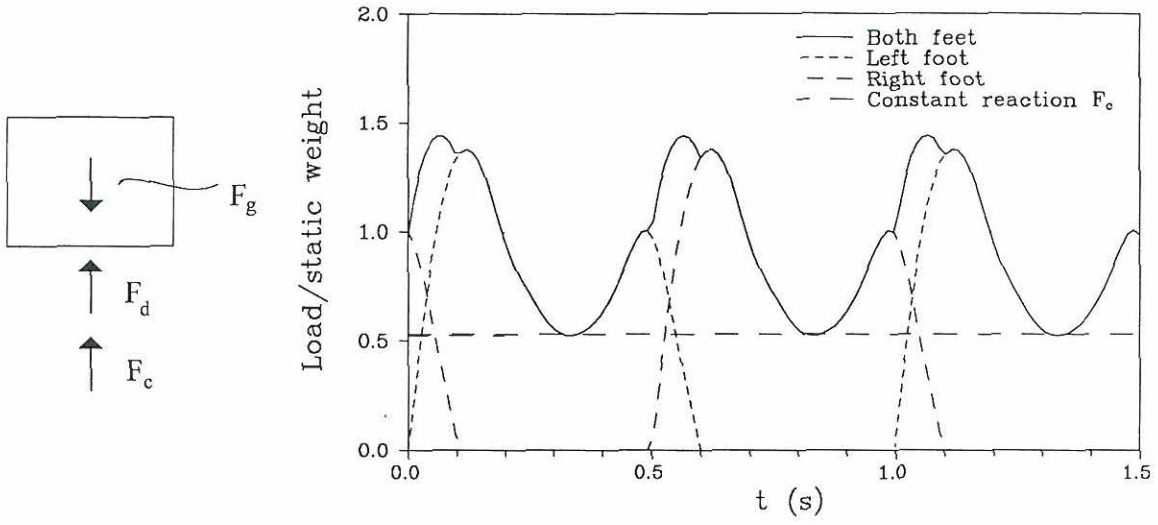

Figure 1: Forces on body and load-time function for brisk walk.

minimum value of the total reaction force ($R = F_c + F_d$). The remaining force is the dynamic force $F_d \geq 0$. The motion of the body is determined by

$$m\ddot{x} = F_d + F_c - F_g \tag{1}$$

The momentum of the periodic motion is also periodic. Conservation of momentum over one time period T_p is found as

$$\int_0^{T_p} (F_d + F_c - F_g)\, dt = 0 \tag{2}$$

Upon inserting the constant forces F_g and F_c the equation (2) yields the periodic impulse I of the dynamic force:

$$I = \int_0^{T_p} F_d\, dt = (1-\gamma)mgT_p \tag{3}$$

Simple human motions can often be modelled by a few periodic impulses. The load-time function of walking, shown in figure 1 (right) could be modelled by a constant reaction force F_c and one periodic load function F_d (impulse). In a simple model F_d would consist of periodic Dirac impulses corresponding to impacts on the structure. Between impacts the body moves in a conservative force field. The simple model then corresponds to bouncing of a ball. Anticipating that the center of mass of the body moves a distance h in the vertical direction, the maximum change in potential energy is $(1-\gamma)mgh$. Setting the maximum potential energy equal to the kinetic energy before impact $\frac{1}{2}mv^2$ yields the impact velocity:

$$v = \sqrt{2(1-\gamma)gh} \tag{4}$$

The change in momentum ΔP due to impact is determined by the mass and the change in velocity $2v$:

$$\Delta P = 2mv = 2m\sqrt{2(1-\gamma)gh} \tag{5}$$

Setting the momentum change equal to the impulse of the dynamic force $I = \Delta P$ yields

$$\gamma = 1 - \frac{8h}{gT_p^2} \tag{6}$$

For discontinous contact such as jumping ($\gamma = 0$) equation (6) gives a direct mechanical link between the motion height and the time period, eg. $h = \frac{1}{8}gT_p^2$. For continous contact it can be used for estimation of the static reaction force. Using a load time function from brisk walk from Baumann & Bachmann [2] with $T_p = 0.5s$ and $\gamma = 0.53$, shown in figure 1 (right), the vertical movement of the center of mass becomes $h = 0.14m$.

In the case of human motion we can estimate the movement of the center of mass, whereby it is possible using equation and (3) and (5) to find the impulse needed for the periodic motion. If the human motion is known as a function of time, the time derivative of the momentum gives the total force on the body $F = \frac{d}{dt}(mv)$. This would enable determination of the load function.

Impulse response

The structural response to the impulsive loads from for example human motion is considered in the next two sections, først for a single impulse load and secondly for one periodic impulse load.

For a single degree of freedom system with (structural) mass M, undamped eigenfrequency ω_n and damping ratio ξ the displacement response to a Dirac impulse I is given by

$$\delta = \frac{I}{M\omega_d} e^{-\xi\omega_n t} \sin \omega_d t \tag{7}$$

where the damped eigenfrequency is $\omega_d = \omega_n\sqrt{1-\xi^2}$. For impulses of finite time duration t_p, the shape of the force time function has to be taken into account. For different impulse shapes figure 2 (left) shows the dynamic magnification factor κ corresponding to the ratio between the maximum dynamic and static response. The magnification factor has been calculated using a damping ratio of $\xi = 0.05$, but could conservatively be calculated for zero damping.

An impulse correction factor α can be found by normalizing the maximum dynamic response with the Dirac impulse response. Figure 2 (right) shows the impulse correction factor for different impulse shapes. An approximation of the impulse response can thus be obtained by using the Dirac impulse response (7) multiplied by the correction factor α.

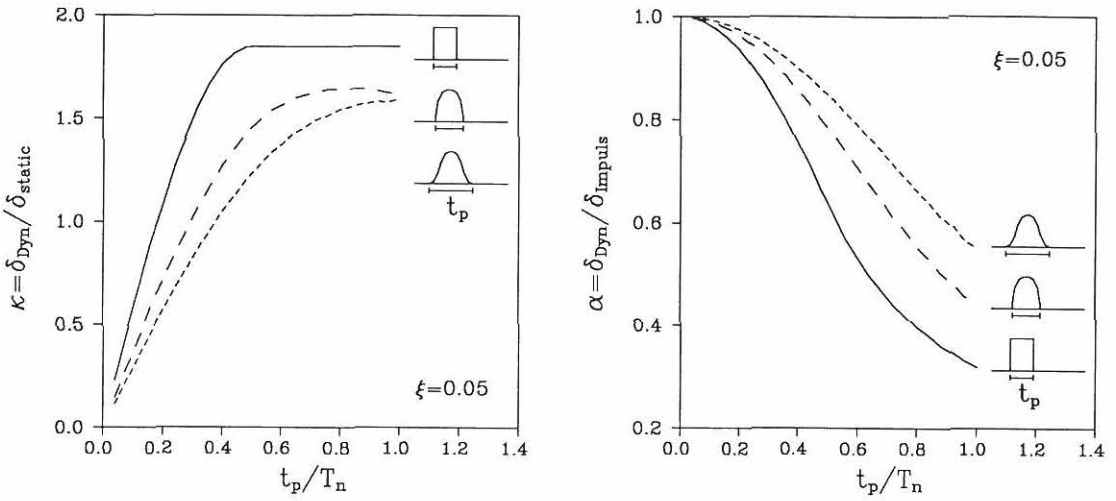

Figure 2: Dynamic magnification factor κ and impulse shape correction factor α.

Periodic impulse response

For a Dirac impulse acting periodically with the period T_p on the damped single degree of freedom system, the response has be found analytically as

$$\delta = \frac{I}{M\omega_d} e^{-\xi\omega_n t} \left(\frac{A}{C} \sin \omega_d t + \frac{B}{C} \cos \omega_d t \right) \tag{8}$$

where the constants are determined as

$$\begin{aligned} A &= 1 - e^{-\xi\omega_n T_p} \cos \omega_d T_p \\ B &= e^{-\xi\omega_n T_p} \sin \omega_d T_p \\ C &= 1 - 2e^{-\xi\omega_n T_p} \cos \omega_d T_p + e^{-2\xi\omega_n T_p} \end{aligned}$$

The maximum displacement response is found at the time

$$t_{ext} = \frac{1}{\omega_d} \arctan \left(\frac{\xi\omega_n B - \omega_d A}{\xi\omega_n A + \omega_d B} \right) + \frac{n\pi}{\omega_d} \tag{9}$$

where n is the lowest integer for which $t_{ext} > 0$. For multiple periodic Dirac impulses superposition can be used and t_{ext} would have to be found for the superimposed responses.

Using a Fourier series solution to find the "correct" response of the periodic half-sine impulse it is possible to compare the maximum response with that of the periodic Dirac impulse response multiplied by the impulse shape correction factor

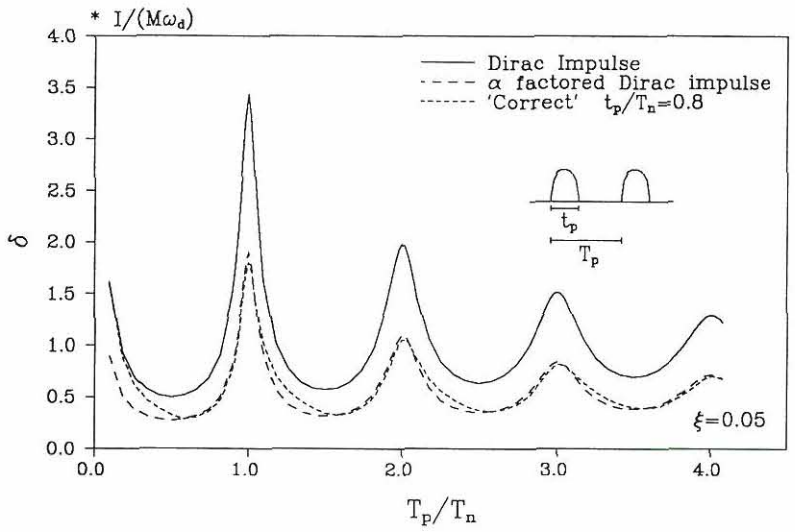

Figure 3: Periodic Dirac impulse response (half-sine impulse).

α. Computing the results for a variety of t_p/T_n ratios and for T_p/T_n ratios in the interval $]0, 4]$ shows that the scaled periodic Dirac impulse response is a good approximation. For $t_p/T_n = 0.8$ the results are shown in figure 3. It is seen that the agreement is good even for this large contact duration compared to the natural period. For the case $t_p/T_n = 0.8$ shown in figure 3, it is worth noting that below $T_p/T_n = 0.8$ the impulse time durations overlap, resulting in a static response from the constant reaction part F_d of the load. This has currently not been further investigated.

Experimental ideas

The experimental part of this research project will monitor the movements of the person or persons participating in the experiment, so that it will be possible to estimate the movement of the center of mass. A simple model of a person could consist of 2 parts for each leg and arm, one part for the body and one for the head, thus giving 10 rigid moving parts. The center of mass would have to be confirmed with medical research.

The experiments will be carried out in two main phases, one in the laboratory and another at a grandstand at a rock concert or a football match. In the laboratory there will probably be three stages. In the first stage the body motion and the load as a function of time will be measured on a small platform mounted on a stiff laboratory floor for jumping and the special wave motion ("the wave" seen at football matches). In the second stage the load measuring platform will be mounted

on a simple beam structure and the measurements repeated on the beam both on and off the platform. The eigenfrequency of the beam structure may be varied by altering support conditions. In the third stage the effect of multiple persons on the beam will be measured.

At the grandstand measurements will be performed for one person jumping, for multiple persons jumping and for real situations either at concerts or at football matches.

References

[1] H. Bachmann and W. Ammann. *Vibrations in structures - Induced by man and machines*, IABSE, Zürich, 1987.

[2] K. Baumann and H. Bachmann. *Durch Menschen verursachte Lasten und deren Auswirkungen auf Balkentragwerke*, Bericht Nr. 7501-3, Institut für Baustatik und Konstruktion, ETH Zürich, 1988.

[3] A. Ebrahimpour and R. L. Sack. Modeling dynamic occupant loads. *Journal of Structural Engineering*, Vol. 115, No. 6, 1989.

[4] A. Ebrahimpour, R. L. Sack and P. D. Van Kleek. Computing crowd loads using a nonlinear equation of motion, *Computers & Structures*, Vol. 41, No. 6, pp. 1313-1319, 1991.

[5] A. Ebrahimpour and R. L. Sack. Design live loads for coherent crowd harmonic movements,*Journal of Structural Engineering*, Vol. 118, No. 4, 1992.

[6] P-E. Eriksson and S. Ohlsson. Dynamic Footfall loading from groups of walking people. *Proc. of Symposium/Workshop on Serviceability of Buildings*, Vol. 1, NRCC, Ottawa, Canada, pp. 497-511, 1988.

[7] P-E. Eriksson. Modal analysis of pre-cast concrete floor element, *Proc. of the 9th International Modal Analysis Conference*, Firenze, Italy 1991. Published by the Society for Experimental Mechanics, USA, 1991.

[8] P-E. Eriksson. Vibration of low-frequency floors - offices and shopping centers. *Proc. of the First World Conference on Constructional Steel Research*, (Acapulco), Elsevier Science Publishers Ltd., Barking , England, pp. 409-418, 1992.

[9] P-E. Eriksson. *Vibration of low-frequency floors - Dynamic Forces and response Prediction*, Doctoral thesis, Publication D 94:3. Unit for Dynamics in Design, Chalmers University of Technology, Göteborg, Sweden, 1994.

[10] F. C. Harper. The mechanics of walking, Research applied in industry, Vol. 15, pp. 23-28, 1962

[11] L. Nilsson. *Impact loads produced by human motion. Part 1: Background and experimental investigation*, document D13:1976, Swedish Council for Building Research, 1976.

[12] L. Nilsson. *Impact loads produced by human motion. Part 2: Requirements for Structures and Methods of test*, document D20:1980, Swedish Council for Building Research, 1980.

[13] S. V. Ohlsson. *Floor vibrations and human discomfort*, Department of Structural Engineering, Chalmers University of Technology, Göteborg, Sweden, 1982

[14] S. V. Ohlsson and P-E. Eriksson. Structural serviceability of commercial steel buildings - General aspects and vibrations, *Proc. of the Nordic Steel Colloquium*, Danish Steel Institute, pp. 79-88, 1991.

[15] S. V. Ohlsson. Serviceability criteria - especially floor vibration criteria, Proceedings of the *1991 International Timber Engineering Conference, London*, Vol. 1, pp, 1.58-1.65. Published by TRADA, High Wycombe, U.K. 1991.

[16] S. Ohlsson and M. Perstorper. Elastic wood properties from dynamic tests and computer modeling, *Journal of Structural Engineering*, Vol. 118, No. 10, 1992.

[17] G. Pernica. Dynamic live loads at a rock concert, *Can. J. Civ. Eng.*, Vol. 10, 1983.

[18] J. H. Rainer and G. Pernica. Vertical dynamic forces from footsteps, *Canadian Acoustics*, Vol 14, no 2, pp 12-21, 1986.

[19] C. Rebelo and R. J. Scherer. A stochastic model for human induced rhythmic loads, *Structural Safety & Reliability*, Schuëller, Shinozuka & Yao (eds), Balkema, Rotterdam, 1994.

Abstract

Fatigue and crack propagation

Fatigue crack propagation is a well-known phenomena. Normally it is studied by using empirical formulas. However at the Department of Structural Engineering, Technical University of Denmark, an energy balance crack growth formula has recently been developed **[90.1]**. This formula can be used to predict crack propagation arising both from static load and from fatigue loading.
The potential power of a theoretical formula is that it is not necessary to determine crack growth parameters by time demanding and expensive tests, as is the case when the well-known Paris equation **[63.1]**

$$\frac{da}{dN} = C\Delta K^m \qquad (1)$$

is used. Here C and m are empirical constants, which have to be determined by crack growth tests. The new formula is based upon well-known parameters such as the modulus of elasticity E, the yield strength f_y, the true fracture stress f_t, the critical stress intensity factor K_{IC} and of course the geometrical dimensions of the actual cracked specimen.
A large number of fatigue tests have been performed earlier, and some of these have been compared with the new formula in an earlier paper **[91.1]**. The comparison did show very good agreement. However unfortunately most of the tests were not supported with all the relevant parameters, especially the true fracture stress f_t and the K_{IC} - K_I relation. These parameters therefore had to be estimated as far as possible.
In this project a new series of fatique tests is performed, where all the relevant parameters are measured. The chosen materials are two high strength aluminiums Al2024 and Al7075 and one high strength steel Hardox400.
To determine all the parameters it is necessary to establish three kinds of tests. At first a simple tension test with the purpose to determine the modulus of elasticity, the yield strength and finally the true fracture stress. Secondly it is important to determine the critical stress intensity factor for instance by using the ASTM standard test **[70.1]** and finally to perform a fatigue test, where the relationship between the crack lengt **a** and the number of cycles **N** is measured.

The main purpose of the project is to test the new theory of crack propagation by comparing it's results with test results. In the following the new theory will be presented.

The theory is based on an energy balance criterion, This leads to a formula, which is a first order differential equation to be solved numerically.
Energy criteria were introduced by Griffith **[21.1]**. For a load controlled test, where a and P are the independent variables, the energy balance equation can be written, see **[90.1]**:

$$\frac{\partial W}{\partial a}da - P\frac{\partial u}{\partial a}da + G_F b da = 0 \qquad (2)$$

Here W is the elastic energy, a is the crack length, P is the force, u is the deformation in the direction of the force, G_F is the fracture energy and b is the thickness.
Taking into account that the effective length of the crack is larger by a length l_e than the one which is actually seen, we have:

$$\frac{\partial W}{\partial a}da + \frac{\partial W}{\partial a}dl_e - P\frac{\partial u}{\partial a}da - P\frac{\partial u}{\partial a}dl_e + G_F b da = 0 \qquad (3)$$

In **[90.1]** l_e has been determined by some approximate energy considerations. For a material with yield strength f_y and tensile strength f_t it was shown that l_e may be put equal to:

$$l_e = \frac{1}{2\pi}\frac{K_I^2}{f_y f_t} \qquad (4)$$

Rearranging the energy balance criterion **(3)** we get the first order differential equation, (see **[94.1]**):

$$\frac{da}{dP} = \frac{\dfrac{\partial W_{(a+l_e)}}{\partial a}\dfrac{\partial l_{e(a)}}{\partial P}}{G_F b - \dfrac{\partial W_{(a+l_e)}}{\partial a}} \qquad (5)$$

Using that the derivative of the strain energy $\partial W/\partial a$ can be expressed by the stress intensity factor K_I and substituting l_e (formula **(4)**) into formula **(5)** we get:

$$\frac{da}{dP} = \frac{K_{I(a+l_e)}^2 \dfrac{\partial}{\partial P}\left(\dfrac{K_{I(a)}^2}{2\pi f_y f_t}\right)}{K_{IC}^2 - K_{I(a+l_e)}^2} \qquad (6)$$

This expression is called the *energy crack propagation formula* and by integration over one cycle the crack-velocity *da/dN* may be found as a function of P and a.

Substituting the relation proposed in **[90.1]**, see also **[94.1]**:

$$K_{IC} = M' K_I^{n'} \tag{7}$$

and neclecting K_I in the nominater in **(6)** assuming $K_I << K_{IC}$, it may be shown (see **[91.1,p50-52]**) that equation **(6)** can be written:

$$\frac{da}{dN} = \frac{1}{4\pi f_y f_t (M')^2} K_I^{4-2n'} \tag{8}$$

This formula indicates that the Paris constants **C** and **m** are related with the parameters n' and M' as follows:

$$\begin{aligned} m &= 4-2n' \\ C &= \frac{1}{4\pi f_y f_t (M')^2} \end{aligned} \tag{9}$$

The most important result of the investigation performed is that in order to make reliable predictions about crack growth two important issues must be considered.
First it must be taken into account, that the critical value of the stress intensity factor or the fracture energy varies with the stress intensity level. Relations have been measured for three materials and they clearly exhibit such a relationship.
Second it must be taken into account, that the ultimate stresses at the crack tip are much higher than the usual values obtained by standard laboratory measurements. To calculate the enhanced values is extremely difficult, and has never to the authors opinion been done before. In **[94.1]** it has been suggested to base the calculation on Weibulls theory of size effects. However it turned out that the size range, which can be obtained in the laboratory, is far too small to get reliable results. To remedy this situation, it has been suggested to base the calculation of the Weibull parameters on the Orowan estimate of the atomic strength, i.e. the strength of a perfect crystal free of dislocations, grain boundaries, foreign particles etc.

The solution presented in **[94.1]** of the two basic problems in deriving a theoretical formula for crack growth was shown to give good estimates of the crack growth, far better than the results obtained by other theoretical crack growth formulas.
However much more work is necessary to cover the whole range of relevant materials and to cover the relevant strength range for the individual materials.

An example of predicting the crack propagation is shown in figure 1.

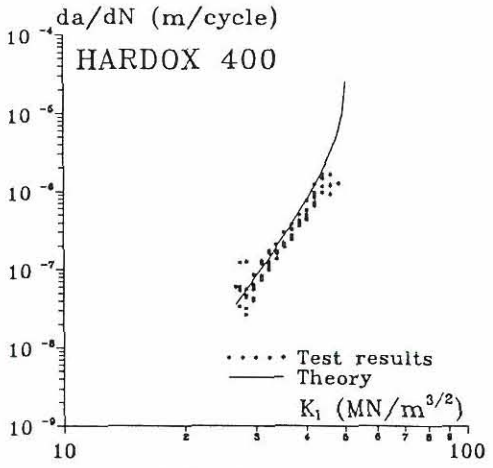

Figure 1 *Calculated crack propagation for the high strength steel Hardox 400.*

As result of this project a paper is published at the Department of Structural Enginering, Technical University of Denmark **[94.1]**.

References

[21.1] A.A.Griffith,*The phenomena of rupture and flow in solids*, Phil.Trans.Soc.of London,A221,1921,p163-197.

[63.1] P.C.Paris and F.Erdogan, *A critical analysis of crack propagation laws*, ASME, serie D, Vol 85, 1963.

[70.1] W.F.Brown,*Review of developments in plane strain fracture toughness testing*,ASTM STP 463,1970.

[90.1] M.P.Nielsen, *An energy balance crack growth formula,* Bygningsstatiske Meddelelser nr 3-4, Dansk Selskab for Bygningsstatik, Sept 1990.

[91.1] H.H.Pedersen and T.C.Hansen, *Revneudvikling i stål*,(Crack propagation in steel), M.Sc.-Thesis, Department of Structural Engineering, Technical University of Denmark, Feb 1991.

[94.1] T.Cornelius Hansen, *"Fatigue and Crack Propagation - A New Approach to Predict Crack Propagation Behavior"*, No.R316, Dept.of Struct.Engineering,DTU,1994.